



Forschungsberichte
aus
dem Institut
für Höchstfrequenztechnik
und Elektronik
der
Universität Karlsruhe

Herausgeber:
Prof. Dr.-Ing. W. Wiesbeck

Dirk Didascalou

**Ray-Optical
Wave Propagation Modelling
in Arbitrarily Shaped Tunnels**

Band 24

Copyright: Institut für Höchstfrequenztechnik und Elektronik
Universität Karlsruhe (TH), 2000

alle Rechte vorbehalten

Druck: Druckerei Gunter Dünnbier, 02779 Großschönau,
Tel. 035841-36757

ISSN: 0942-2935

Vorwort des Herausgebers

Zu Beginn des 3. Jahrtausends überschlagen sich die Berichte in den Medien zur Zukunft der Kommunikation. Daten, Audio und Video werden in den Industrienationen flächendeckend verfügbar sein. Das Internet wird allgegenwärtig. Wenn man diesen Erwartungen vertraut, und ich bin der Überzeugung, dass sie die Zukunft noch unterschätzen, überfällt einen ein etwas beklemmendes Gefühl ob der bevorstehenden technischen, gesellschaftlichen und sozialen Revolution. Bringt man es als Ingenieur technisch gesehen auf den Punkt, dann resultiert hieraus, dass diese gesamte Zukunft in einem begrenzten, nicht vermehrbaren und nicht transportierbaren Spektrum ausgetragen wird. Die entscheidende Frage für die Unternehmen wird sein: was ist der Preis für Spektrum? Wird ein Hertz soviel wert sein wie ein Gramm Gold? Welche regionale Ausdehnung wird damit erkaufte? Wird der Preis vielleicht 1000mal so hoch sein? Diese sicherlich nicht einfach zu beantwortenden Fragen werden die Regulierer, der Staat und der Markt zu lösen haben. Als Ingenieure können wir durch Technologien, Methoden und Verfahren dazu beitragen, dass das Spektrum so effizient wie nur irgend möglich genutzt wird. Schlagworte werden heute kaum benutzte Begriffe sein wie *friendly coexistence*, *sharing rules*, *adaptability* und *heterogeneity*.

Hiermit ist zum Originalton der Dissertation von Herrn Dirk Didascalou übergeleitet. Mit seiner hervorragenden Arbeit zur Wellenausbreitung in Tunnels leistet er einen wesentlichen Beitrag zur effizienten Planung von Kommunikationsnetzen in dieser sehr schwierigen Umgebung. Anders als im ländlichen und städtischen Raum wird die Wellenausbreitung in beliebig im Querschnitt und im Längsschnitt geformten Tunnels durch Mehrfachreflexionen und bewegte Fahrzeuge dominiert. So führen die Reflexionen bei konkaven Krümmungen z.B. zur Wellenfokussierung. Technisch gesehen resultieren daraus keine Probleme, theoretisch ist es jedoch äusserst schwierig zu behandeln. Zur Lösung dieses Problems ist von Herrn Didascalou eine sehr wirkungsvolle Normierung in einem strahlenoptischen Wellenausbreitungsmodell eingeführt worden. Damit wird erstmals eine derartige Umgebung effizient und ausreichend genau berechenbar. Ich wünsche dem entstandenen Planungswerkzeug und den Ideen eine effiziente Verbreitung.

Prof. Dr.-Ing. Werner Wiesbeck

- Institutsleiter -

**Forschungsberichte aus dem
Institut für Höchstfrequenztechnik und Elektronik
der Universität Karlsruhe (TH)**

Herausgeber: Prof. Dr.-Ing. Werner Wiesbeck

- Band 1 Daniel Kähny
Modellierung und meßtechnische Verifikation polarimetrischer, mono- und bistatischer Radarsignaturen und deren Klassifizierung
- Band 2 Eberhardt Heidrich
Theoretische und experimentelle Charakterisierung der polarimetrischen Strahlungs- und Streueigenschaften von Antennen
- Band 3 Thomas Kürner
Charakterisierung digitaler Funksysteme mit einem breitbandigen Wellenausbreitungsmodell
- Band 4 Jürgen Kehrbeck
Mikrowellen-Doppler-Sensor zur Geschwindigkeits- und Wegmessung - System-Modellierung und Verifikation
- Band 5 Christian Bornkessel
Analyse und Optimierung der elektrodynamischen Eigenschaften von EMV-Absorberkammern durch numerische Feldberechnung
- Band 6 Rainer Speck
Hochempfindliche Impedanzmessungen an Supraleiter / Festelektrolyt-Kontakten
- Band 7 Edward Pillai
Derivation of Equivalent Circuits for Multilayer PCB and Chip Package Discontinuities Using Full Wave Models
- Band 8 Dieter J. Cichon
Strahlenoptische Modellierung der Wellenausbreitung in urbanen Mikro- und Pikofunkzellen
- Band 9 Gerd Gottwald
Numerische Analyse konformer Streifenleitungsantennen in mehrlagigen Zylindern mittels der Spektralbereichsmethode
- Band 10 Norbert Geng
Modellierung der Ausbreitung elektromagnetischer Wellen in Funksystemen durch Lösung der parabolischen Approximation der Helmholtz-Gleichung
- Band 11 Torsten C. Becker
Verfahren und Kriterien zur Planung von Gleichwellennetzen für den Digitalen Hörrundfunk DAB (Digital Audio Broadcasting)
- Band 12 Friedhelm Rostan
Dual polarisierte Microstrip-Patch-Arrays für zukünftige satellitengestützte SAR-Systeme

**Forschungsberichte aus dem
Institut für Höchstfrequenztechnik und Elektronik
der Universität Karlsruhe (TH)**

- Band 13 Marcus Demmler
Vektorkorrigiertes Großsignal-Meßsystem zur nichtlinearen Charakterisierung von Mikrowellentransistoren
- Band 14 Andreas Froese
Elektrochemisches Phasengrenzverhalten von Supraleitern
- Band 15 Jürgen v. Hagen
Wide Band Electromagnetic Aperture Coupling to a Cavity: An Integral Representation Based Model
- Band 16 Ralf Pötzschke
Nanostrukturierung von Festkörperflächen durch elektrochemische Metallphasenbildung
- Band 17 Jean Parlebas
Numerische Berechnung mehrlagiger dualer planarer Antennen mit koplanarer Speisung
- Band 18 Frank Demmerle
Bikonische Antenne mit mehrmodiger Anregung für den räumlichen Mehrfachzugriff (SDMA)
- Band 19 Eckard Steiger
Modellierung der Ausbreitung in extrakorporalen Therapien eingesetzter Ultraschallimpulse hoher Intensität
- Band 20 Frederik Küchen
Auf Wellenausbreitungsmodellen basierende Planung terrestrischer COFDM-Gleichwellennetze für den mobilen Empfang
- Band 21 Klaus Schmitt
Dreidimensionale, interferometrische Radarverfahren im Nahbereich und ihre meßtechnische Verifikation
- Band 22 Frederik Küchen, Torsten C. Becker, Werner Wiesbeck
Grundlagen und Anwendungen von Planungswerkzeugen für den digitalen terrestrischen Rundfunk
- Band 23 Thomas Zwick
Die Modellierung von richtungsaufgelösten Mehrwegegebäudefunkkanälen durch markierte Poisson-Prozesse
- Band 24 Dirk Didascalou
Ray-Optical Wave Propagation Modelling in Arbitrarily Shaped Tunnels

À Michèle et à Florent

Ray-Optical Wave Propagation Modelling in Arbitrarily Shaped Tunnels

Zur Erlangung des akademischen Grades eines

DOKTOR-INGENIEURS

von der Fakultät für
Elektrotechnik und Informationstechnik
der Universität Fridericiana Karlsruhe

genehmigte

DISSERTATION

von

Dipl.-Ing. Dirk Leonidas Didascalou
aus Hamburg

Tag der mündlichen Prüfung:

17. Februar 2000

Hauptreferent:

Prof. Dr.-Ing. Werner Wiesbeck

Korreferent:

Prof. Dr.-Ing. habil. Friedrich M. Landstorfer

Acknowledgements

I would like to thank the Director of the *Institut für Höchstfrequenztechnik und Elektronik (IHE)*, Prof. Dr.-Ing. Werner Wiesbeck, for his support in enabling me to carry out a Ph.D. degree (Dr.-Ing.) at the Universität Karlsruhe (TH) in Germany. My appreciation is extended to Prof. Dr.-Ing. habil. Friedrich M. Landstorfer, the second examiner of this thesis, for the interest in my work.

I acknowledge the invaluable suggestions, corrections and constructive criticisms of the reviewers of this thesis: my colleagues and friends Dipl.-Ing. Martin Döttling, Dr.-Ing. Norbert Geng, Dipl.-Ing. Jürgen Maurer and Dipl.-Ing. Ralph Schertlen. I am particularly indebted to Dipl.-Ing. Gunther Auer and Dr. Keith Palmer, who tried hard to make my pidgin English more readable.

Among the many students and colleagues, who have helped me during my work on tunnels at the IHE, many thanks are due to Matthias Dübon, Thomas Kösterkamp, Alexander Widmann, Juan Manuel Canabal Muñoz, Carles Galdón Durá, Bernd Ruthmann, Dipl.-Ing. Yan Venot and Dr.-Ing. Frederik Küchen. A special tribute is owed to Dipl.-Phys. Thomas Schäfer and Dipl.-Phys. Frank Weinmann, who definitively contributed most to the development of the simulation tool.

I am grateful to Prof. Dr. rer. nat. Manfred Thumm, the Director of the *Institut für Hochleistungsimpuls- und Mikrowellentechnik*, at the Forschungszentrum Karlsruhe, Germany, for the provision of the millimeter-wave measurement equipment and to Dipl.-Ing. Andreas Arnold, Richard Kunkel and Dipl.-Ing. Oliver Schindel for their assistance.

I would like to thank Dipl.-Ing. Jörg Borm, E-Plus Mobilfunk GmbH, Düsseldorf, Germany, for the provision of the GSM1800 measurement equipment and his assistance, as well as Dipl.-Ing. Michael Feistel and Dipl.-Ing. Udo Straub, both Mannesmann Mobilfunk, Niederlassung Stuttgart, Germany, and Dipl.-Ing. Jürgen Köttnitz and Dipl.-Ing. Hanns-Michael Müller, both Mannesmann Mobilfunk, Niederlassung Nord-Ost, Germany, for the provision of the GSM900 measurement equipment. Special thanks to Dipl.-Ing. Hans-Jürgen Liesegang, Berliner Verkehrsbetriebe (BVG), Berlin, Germany, for his kind cooperation and to all the staff of his company for their unfailing professionalism and friendliness, making the measurements in the Berlin subway possible.

Finally, I wish to thank my wife, Michèle, for the encouragement and the patience during the numerous week-ends and evenings of typing. Without her, this work would have hardly been possible.

Contents

Glossary	v
Table of symbols and variables	vii
1 Introduction	1
1.1 Background and motivation	1
1.2 Scope and objective of the thesis	2
1.3 Outline of the thesis	4
2 Ray-optical wave propagation modelling	6
2.1 The ray concept	6
2.2 Geometrical optics and propagation modelling	9
2.3 Propagation phenomena	11
2.3.1 Free space propagation and absorption	12
2.3.1.1 Free space propagation	12
2.3.1.2 Absorption	12
2.3.2 Reflection at smooth surfaces	13
2.3.2.1 Planar surfaces	13
2.3.2.2 Curved surfaces	16
2.3.3 Scattering from rough surfaces	17
2.3.3.1 Roughness criteria	18
2.3.3.2 Slightly rough surfaces: the modified Fresnel reflection coefficients	18
2.3.3.3 Stochastic scattering approach	19
2.4 Multipath propagation and analysis	23
2.4.1 Formal description of a propagation path	24
2.4.2 Multipath propagation	26
2.4.3 Broadband analysis and channel parameters	27
2.4.3.1 Frequency and impulse response of the trans- mission channel	28

2.4.3.2	The delay-Doppler-spread function	29
2.4.3.3	Delay spread	30
2.4.3.4	Doppler spread	31
2.5	Summary	31
3	Ray tracing in a tunnel environment	33
3.1	Methods of ray tracing	34
3.1.1	Direct approach: image theory	34
3.1.2	Indirect approach: ray launching	35
3.1.2.1	Discrete ray tubes	35
3.1.2.2	Reception spheres	37
3.1.2.3	Identification of multiple rays	38
3.2	Ray launching in curved geometry	39
3.2.1	Ray tubes: approximate solution for 2D-curvature	39
3.2.2	Reception spheres: the concept of ray density normalization (RDN)	40
3.2.2.1	Determination of the number of multiple rays	40
3.2.2.2	Prerequisites of the RDN	42
3.3	Application of the ray density normalization	42
3.3.1	Relationship between divergence of a ray and ray density	43
3.3.2	Field trace	43
3.3.3	Power trace	45
3.4	The method of power flow	48
3.5	Summary	50
4	The simulation approach	51
4.1	Geometry	51
4.1.1	Straight sections	52
4.1.2	Curves and clothoids	52
4.1.2.1	Clothoid approximation	53
4.2	Stochastic ray launching	56
4.3	Coupling into the tunnel	57
4.4	Moving obstacles	58
4.5	Analysis	59
4.6	Additional remarks on the implementation	60
4.7	Summary	61
5	Theoretical verification	62
5.1	The rectangular waveguide	63
5.1.1	Geometry of the rectangular waveguide	63
5.1.2	Green's function in PEC rectangular waveguide	63
5.1.3	Rectangular waveguide with dielectric boundaries	66

5.2	The circular waveguide	69
5.2.1	Choice of the canonical (reference) geometry	69
5.2.2	Corrugated circular waveguide	69
5.2.3	Comparison of the different techniques in circular waveguide with dielectric boundary	71
5.3	Stochastic scattering approach	73
5.3.1	Arrangement and procedure	73
5.3.1.1	Radar cross section per unit area	74
5.3.1.2	Determination of the RCS matrix by ray tracing using the stochastic scattering approach	75
5.3.1.3	The Kirchhoff models	76
5.3.2	Comparison of the methods	77
5.4	Summary	81
6	Experimental verification in scaled model tunnels	82
6.1	Measurement setup and procedure	83
6.2	Comparisons in a straight concrete tube	85
6.3	Comparisons in a bent stoneware tube	88
6.4	Comparisons in a model tunnel	92
6.5	Summary	96
7	Scenarios and applications	97
7.1	The Berlin subway	97
7.1.1	Measurement setup and procedure	98
7.1.1.1	Measurement equipment	98
7.1.1.2	Measurement environment	99
7.1.2	Results	101
7.1.2.1	Achievable accuracy in the rectangular straight tunnel (U5)	101
7.1.2.2	Path loss in the curved arched-shaped tunnel (U8)	103
7.1.2.3	Influence of curves on the simulation accuracy	105
7.1.2.4	Influence of the cross-sectional shape on the simulation accuracy	105
7.1.2.5	Fast fading characteristics	107
7.1.2.6	Distribution of the propagating power in curves	110
7.2	Exterior antenna placement	112
7.2.1	Difference of interior and exterior positions	112
7.2.2	Exterior antenna locations	113
7.2.2.1	Description of the scenario	113
7.2.2.2	Antenna height	114

7.2.2.3	Distance from the tunnel entrance	114
7.2.2.4	Lateral placement	115
7.3	Moving vehicles and broadband analysis	116
7.4	Summary	119
8	Conclusions	120
A	Radii of curvature after reflection	123
B	Intersection algorithms	125
B.1	Plane	125
B.2	Rectangle	126
B.3	Sphere	126
B.4	Circular cylinder	127
B.5	Elliptical cylinder	128
B.6	Elliptical torus	129
C	Determination of send-range	133
C.1	Rectangular cross section	133
C.2	Elliptical (arched) cross section	135
D	Directional antenna patterns	137
D.1	D-band horn and waveguide probe	137
D.2	Kathrein K73226X (LogPer)	140
D.3	Jaybeam J7360 (Yagi)	141
D.4	$\lambda/4$ -monopoles with circular ground plane	142
	Bibliography	143

Glossary

<i>i</i>D	<i>i</i> -dimensional
AS	angular spread
BWO	backward wave oscillator
CDF	cumulative distribution function
D-band	frequency band between 110GHz and 170GHz
DAB	digital audio broadcasting
DCS1800	digital cellular system (at 1800MHz), now GSM1800
DVB	digital video broadcasting
FD	finite difference
FDTD	finite difference time domain
FM	frequency modulated/modulation
FT	field trace
GO	geometrical optics
GTD	geometrical theory of diffraction
GSM	global system for mobile communications (formerly groupe spécial mobile) at 900MHz, 1800MHz or 1900MHz
GSM900	cf. GSM
GSM1800	cf. GSM, formerly DCS1800
HF	high frequency (3MHz–30MHz)
HP	Hewlett Packard
IMR	identification of multiple rays
IS-95	interim standard 1995
IT	image theory
LMS	least mean square
LogPer	log-periodic
LOS	line of sight
MoM	method of moments
PDF	probability density function

PDP	power delay profile
PE	parabolic equation (method)
PEC	perfectly electric conducting
PF	power flow
PO	physical optics
PT	power trace
PVC	polyvinyl chloride
RAM	random access memory
RCS	radar cross section
RDN	ray density normalization
RMS	root mean square
Rx	receiver
SBR	shooting and bouncing ray (approach)
SSA	stochastic scattering approach
TEM	transverse electromagnetic
TETRA	terrestrial trunked radio
Tx	transmitter
UHF	ultra high frequency (300MHz–3GHz)
UTD	uniform geometrical theory of diffraction
UMTS	universal mobile telecommunications system
VHF	very high frequency (30MHz–300MHz)
VNWA	vector network analyzer

Table of symbols and variables

The additional symbols and variables used in the appendices are not listed in the following tables. They are introduced and explained in the respective appendices.

Mathematical notation

F	real scalar
\underline{F}	complex scalar
\vec{F}	vector
\hat{F}	vector with unit length
$\underline{\vec{F}}$	complex vector
$\underline{\underline{F}}$	complex dyadic
$[\cdot]$	real or complex matrix
\tilde{F}	approximate value
\overline{F}	averaged value
$\Re\{\cdot\}$	real part of complex quantity
$\vec{F}_1 \cdot \vec{F}_2$	scalar (or dot) product of two vectors
$\vec{F}_1 \vec{F}_2$	dyadic product of two vectors
$\vec{F}_1 \times \vec{F}_2$	cross product of two vectors
$ \cdot $	absolute value
$\langle \cdot \rangle$	expectation operator
$\delta(\cdot)$	dirac function
$O(x)$	of the order of x
$p(\cdot)$	probability density function (PDF)
$S(\cdot), C(\cdot)$	real Fresnel integrals

Greek letters

α	attenuation constant (linear)
----------	-------------------------------

α	sector angle (intermediate arc, clothoid)
γ	angular separation of launched rays
$\tan \delta_e$	effective electric loss tangent
$\Delta\theta, \Delta\phi$	resolution of discretized solid angle
ε	permittivity, $\varepsilon = \varepsilon_0\varepsilon_r$
ζ	zero mean gaussian random variable
θ, ϕ	polar (spherical) coordinates
θ	angle of incidence/reflection/scattering
ϑ	surface slope
$\tan \vartheta$	surface gradient
λ	wavelength, $\lambda = c/f$
μ	permeability, $\mu = \mu_0\mu_r$
μ_M	mean (error) between measurement and prediction
ν	doppler shift
ξ	any random variable
ρ	radius of curvature of wave front (astigmatic ray tube)
ρ_M	2D correlation coefficient between measurement and prediction
$[\sigma]$	polarimetric radar cross section (RCS) matrix
$[\sigma^0]$	RCS matrix per unit area
σ_h	standard deviation of surface roughness
σ_e	effective conductivity
σ_M	standard deviation between measurement and prediction
σ_ν	doppler spread
σ_τ	delay spread
τ	delay time of multipath component
ϕ_{hh}	autocorrelation coefficient of surface heights
ψ_0	phase at input port/terminals of antenna
ω	angular frequency, $\omega = 2\pi f$
Ω	solid angle

Latin letters

a	amplitude of multipath component
a	horizontal half axis of ellipse
A	area
A	attenuation (in dB)
A_e	effective area of antenna, $A_e = \frac{\lambda_0^2}{4\pi} G \vec{C} ^2$
b	proportionality factor of clothoid
a	vertical half axis of ellipse
C	directional antenna pattern

d	diameter
d	distance
D	maximum dimension of an aperture
\hat{e}	unit vector for field decomposition at reflection point
E	electric field
f	frequency
G	antenna gain
h	surface height, height
h	impulse response
H	magnetic field
H	frequency response
hh, vv	co-polarization indices (e.g. vv : from vertical to vertical)
hv, vh	cross-polarization indices (e.g. hv : from vertical to horizontal)
j	index indicating number of reflection/interaction ($1 \dots m$)
j	imaginary unit, $j^2 = -1$
k	index indicating number of rays on same physical propagation path ($1 \dots M$)
k	wave number, $k = 2\pi/\lambda$
l	index indicating the number of (physical) waves/rays reaching a receiver ($1 \dots n$)
l	distance between two points on rough surface
l	length
L	correlation length of (random) surface heights
$L_{x,y}$	dimensions of rectangular plate
m	number of reflections
M	(theoretical) number of multiple rays
\hat{n}	normal vector
n	number of rays reaching receiver due to multipath propagation
n_d	ray density
N	number of launched rays
N	number of rays
P	power
$P_{0,1,2}$	points in space
P_{prop}	total time averaged propagating power through a tunnel
Q_R	reflection point
r	distance (from transmitter), total unfolded path length
r	radius, radius of curvature (e.g. of curve)
r_R	radius of sphere receiver

$R_{\parallel, \perp}$	Fresnel reflection coefficients for parallel resp. perpendicular polarization
s	distance
s	RMS gradient (“mean slope”) of a surface
s	arc length (clothoid, intermediate arc)
S	radiation density (or time averaged Poynting vector)
S	complex polarimetric scattering (matrix)
t	time
T	transfer factor
v	speed (of obstacle, Tx or Rx)
V	induced voltage at output/input port/terminals of antenna
w	width
x, y	location, cartesian coordinates
X	weighting factor
Z	impedance
Z_w	wave impedance, $Z_w = \sqrt{\frac{\mu}{\epsilon}}$

Subscripts

0, 1, 2	indices
0	free space (or vacuum) case
0	reference
\parallel, \perp	parallel, perpendicular
ν	doppler (shift/frequency)
τ	delay (time)
a	(intermediate) arc
A	area
c	curve or curved
cloth.	clothoid(al)
cs	cross section
d	(ray) density
dB	in decibel
D	divergence
DCS	in the DCS1800/GSM1800 band
e	effective
exit	fire exit
F	field trace
GSM	in the GSM900 band
h	height
i	incident

i	isotropic
j, k, l	indices
m	number of ray interactions/reflections
max	maximum (number of reflections)
M	measurement (compared to)
n	normal
n	normalized
p	reception plane
pq	polarization indices
$prop$	propagating
P	plane receiver
P	power trace
P	propagation
r	reflected
r	relative
rp	rectangular plate
rt	ray tube
R	reception sphere
R	receiver or received
s	surface
s	scattering
tot	total (i.e. by all rays)
t	“transmitted” power per ray (power trace approach)
T	transmitter or transmitted
$U5, U8$	subways U5 and U8 in Berlin
w	wave
x, y	location

Superscripts

c, i	coherent, incoherent
i, r, s	incident, reflected, scattered
LP	lowpass
mod	modified

Constants

ε_0	permittivity of vacuum, $\varepsilon_0 = \frac{1}{\mu_0 c_0^2} = 8.854188 \cdot 10^{-12} \approx \frac{1}{36\pi} 10^{-9} \frac{\text{As}}{\text{Vm}}$
μ_0	permeability of vacuum, $\mu_0 = 4\pi 10^{-7} \frac{\text{Vs}}{\text{Am}}$
c_0	speed of light in vacuum, $c_0 = 1/\sqrt{\varepsilon_0 \mu_0} = 2.997925 \cdot 10^8 \frac{\text{m}}{\text{s}}$
Z_{w0}	free space wave (or characteristic) impedance, $Z_{w0} = \sqrt{\frac{\mu_0}{\varepsilon_0}} \approx 120\pi\Omega$

Chapter 1

Introduction

1.1 Background and motivation

Mobile radio communications and broadcasting have become common place. A variety of established (FM-radio, GSM, IS-95, DAB etc.) and upcoming (UMTS, TETRA, DVB etc.) systems and services coexist and share one of the most valuable resources, the electromagnetic spectrum. As a result, almost all these systems operate in the UHF frequency range and above ($> 300\text{MHz}$) in order to meet their spectrum requirements. The motto “the freedom to communicate at any time and at any place” implies a complete and seamless coverage for the offered services. Although in mobile communications over land and in urban areas this is mainly achieved, the one Achilles heel is propagation in tunnels. For example in Germany, there are more than 200 road tunnels with a total length of more than 150km [Str96], and about 4% of the rail way consists of tunnels. Furthermore there is an increased trend in the construction of new tunnels, e.g. in and near settlements for noise prevention, and in fast rail tracks for security reasons. To plan and provide efficient mobile services in tunnels, knowledge of the transmission channel properties is obviously required.

Subsurface radio communication, especially in mines and tunnels, has been a subject of research for several decades [DD⁺70, GDW71, MW74b, Wai75, ELS75, Del82, etc.]. Initially this was mainly intended for professional usage in mines for control, signalling, and emergency applications [MP78]. Traditionally these systems operate in the HF and VHF frequency ranges and below ($< 300\text{MHz}$). For these frequencies, guidance of electromagnetic waves is normally supported by special-purpose cables, e.g. leaky feeders (or radiating cables).

At higher frequencies, however, natural propagation¹ becomes an alternative due to the decreasing attenuation of electromagnetic waves in tunnels for increasing frequency [Lan57, Der78]. In fact, at frequencies above 2GHz, leaky-feeder systems are infeasible because of the opposite effect, namely, the attenuation constant in such cables increases drastically with increasing frequency [Del82, Del87]. Furthermore, natural propagation has the great advantage of lower installation and maintenance costs [Kle93]. In addition to economic reasons, there is another argument in favour of natural wave propagation. Recently, several major tunnels in the Alps were afflicted by disastrous accidents. The enormous heat produced by fires inside the tunnels destroyed all installations. The only means to communicate in such an extreme situation is given by mobile communications via natural propagation.

The overall goal of this thesis follows from the above considerations:

This work is concerned with the calculation of natural electromagnetic wave propagation and the determination of the propagation channel characteristics in highway or railway tunnels in the UHF frequency range and above ($> 300\text{MHz}$).

1.2 Scope and objective of the thesis

Realistic tunnel geometries are generally of rectangular cross section or arched shape, i.e. of elliptical cross section with a raised floor and eventually an additional ceiling. Furthermore, they are mostly curved [Str96]. In order to calculate electromagnetic wave propagation in such tunnels, several modelling approaches can be followed.

The ideal solution would be to solve Maxwell's equations for the boundary conditions imposed by the tunnel's materials, its geometry and eventually enclosed vehicles. Unfortunately, this field-theoretical solution can only be obtained by numerical methods. Full-wave solutions, like finite-difference (FD) [Yee66, Taf95] or method-of-moments (MoM) [Har68, Mit75] techniques, are not feasible due to the enormous computational burden. Already a relatively short rectangular tunnel section of 100m length, 8m width and 5m height would require more than 1 billion voxels at 2GHz due to the necessary discretization of at least $\lambda/10 = 1.5\text{cm}$. For each voxel, a minimum of six values, representing the complex vector field, need to be stored in double precision, resulting in $6 \cdot 8 = 48$ bytes per voxel. Thus, only for the discretization about 50 gigabyte of random access memory (RAM) would be required, indicating the almost infinite computer resources required to solve the problem, regardless the numerical

¹I.e. no special-purpose cables are strung in the tunnel to guide electromagnetic waves [Del82].

approach. Neglecting backward propagating electromagnetic waves, the original computational costly boundary-value problem can be reduced to a more efficient initial-value problem, which can be solved by the parabolic equation (PE) method [Foc65, GW96, Gen96]. However, a fully three-dimensional PE solution is still not available so that the actual modelling can only be performed by further simplifications [ZL⁺99].

A more conventional way to tackle the problem is given by mode theory. Here, the tunnel is treated as a hollow waveguide with perfectly electric conducting (PEC) or dielectric boundaries. Unfortunately, analytical expressions for the wave impedance, propagation constant, cutoff frequency, guide wavelength etc. exist only for very few types, e.g. rectangular or circular cross-section waveguides [Col91, Bal89, Mah91]. In practice, often the first propagating mode is considered solely to characterize wave propagation in different tunnels [ELS75, Del82], [Mah91, Chap. 6]. If one needs to compute the total field in a waveguide, the concept of Green's functions [Bal89, Tai93] or the method of fast mode decomposition [MT99] are available for some canonical geometries and usually for only PEC boundaries. Obviously, realistic bent or arch-shaped tunnels with dielectric or even lossy boundaries can therefore only be treated in a simplified or empirical way by mode theory [MW74b, YA⁺85].

All of the above stated frequency domain approaches² have in common that they only predict the electric or magnetic field in a tunnel or waveguide. Wideband channel parameters, like the power delay profile (PDP), delay spread, Doppler spread, or the angular spectrum (AS) cannot be obtained directly. These parameters, however, are mandatory for modern digital communications systems design and evaluation [Lee89, Pro89, Ste92]. A means to predict wave propagation in a complex environment with an adequate precision in finite time, which also allows to obtain wideband channel characteristics, is given by ray-optical modelling approaches [Kür93, Cic94, vD94, Gsc95, Riz97, Küc98, GW98]. They can also be adopted for tunnels because generally all obstacles in a tunnel are large compared to the wavelengths considered in this thesis [LCL89].

Recently, several ray based methods have been proposed to model the electromagnetic wave propagation in tunnels. Irrespective of their ray-tracing technique (ray launching [ZHK98b], imaging [Mar92, Rem93, Kle93, MLD94] or a combination of both [CJ95, CJ96a]), they all have in common that they can only treat reflections at plane boundaries. As a consequence, either they only look at rectangular (piecewise) straight tunnel sections [Kle93, MLD94, ZHK98b], or they tessellate more complex geometries into multiple plane facets [CJ96a, HCC98].

In contrast, a novel ray-optical method is presented in this work, which

²With the exception of the finite-difference time-domain (FDTD) technique.

is *not* restricted to planar surfaces. For the first time it allows a sufficiently accurate ray-tracing based coherent calculation of the electromagnetic field in tunnels of arbitrary shape. The modelling is based on geometrical optics (GO) [Bal89]. Contrary to classical ray tracing, where the one ray representing a locally plane wave front is searched, the new method requires multiple representatives of each physical electromagnetic wave at a time. The contribution of each ray to the total field at the receiver is determined by the proposed ray density normalization (RDN). This technique has the further advantage of overcoming one of the major disadvantages of geometrical optics, the failure at caustics. Additionally, wideband channel signatures like the power delay profile, or parameters like the delay and Doppler spread, are predicted. The model also handles moving vehicles inside tunnels so that sets of time series can be generated automatically. These sets can for example be used to evaluate the performance of different transmission schemes. Furthermore, deterministic modelling is extended by a stochastic scattering component for rough surface scattering, taking into account the non-deterministic nature of the scattering process. These approaches are verified theoretically with canonical examples, by various measurements at 120GHz in scaled tunnel models, and in real subway tunnels at mobile communications frequencies.

1.3 Outline of the thesis

The methods and techniques described in this thesis are based on ray-optical wave propagation modelling. The chapter 2 is devoted to the foundations and concepts of this modelling approach, leading from the ray concept to geometrical optics and wave propagation modelling. The relevant propagation phenomena are reviewed in section 2.3 and the notation used throughout this thesis is introduced. A new method to include stochastic rough surface scattering into deterministic ray-optical propagation modelling is derived in section 2.3.3.3. Furthermore, multipath propagation is dealt with and the determination of broadband channel parameters with respect to the modelling results is presented (cf. section 2.4).

Then the treatment of ray tracing in tunnels is discussed in chapter 3. First, the existing methods of ray tracing are presented and evaluated in terms of their ability to cope with the special environment of curved tunnels. It was found that all of the commonly used techniques, i.e. imaging, ray launching with reception spheres, or ray launching with discrete ray tubes, are only suited for planar geometries. To circumvent this problem, a novel technique termed ray density normalization (RDN) is derived in section 3.2.2, allowing a sufficiently accurate ray-tracing based prediction of the electromagnetic field in curved geometries. As a side effect, the failure at caustics, which is inherent

to GO-based modelling, is heuristically overcome by this method (cf. section 3.3.3). Additionally, a computationally effective, approximate method is presented in section 3.4, which determines the mean received power in a tunnel as a function of distance from the transmitter.

Chapter 4 deals with common geometries of tunnels and their modelling with a computer. The approach to allow for transmitter placement outside a tunnel is explained in section 4.3. Also, the inclusion of moving obstacles like vehicles, the concept of stochastic ray launching, and the different types of analysis are presented.

The next two chapters are devoted to the validation of the proposed modelling schemes. In chapter 5, the models are compared to theoretical reference solutions in canonical geometries. The method of Green's functions and image theory are used to validate the schemes in a rectangular waveguide (cf. section 5.1). This is followed by a validation in a PEC corrugated circular waveguide. The reference solution for this type of geometry is based on fast mode decomposition (cf. section 5.2). After the theoretical validation, in chapter 6 comparisons to measurements are conducted. The measurements are performed in scaled model tunnels at 120GHz with various constellations: a straight concrete tube with and without a vehicle present in section 6.2, a bent stoneware tube in section 6.3, and a comprehensive model tunnel made of a straight and a curved stoneware tube with a concrete road lane in section 6.4. The almost perfect agreement of theoretical reference solutions and predictions, as well as the very good agreement with measurements validate the presented modelling techniques.

Finally, the applicability and performance of the modelling in real scenarios is tested in chapter 7. For this purpose, measurements have been conducted in the Berlin subway in two different tunnels with various antenna constellations at 945MHz and 1853.4MHz. In contrast to the "laboratory-like" conditions of the model tunnels in chapter 6, these measurements represent a type of worst-case scenario, because of the difficult and varying geometry of the different tunnel sections. It is shown that a correct modelling of the tunnel's cross section and course is mandatory to obtain a sufficiently accurate wave propagation prediction. Furthermore, the ability of the model to generate time series and broadband channel parameters is presented in section 7.3, together with some general results on electromagnetic wave propagation in curved tunnels.

Chapter 2

Ray-optical wave propagation modelling

In this chapter the concepts of ray-optical wave propagation modelling are presented as they are used throughout this thesis. The underlying assumptions and preconditions are briefly reviewed, leading from the ray concept (cf. section 2.1) to geometrical optics (GO) and wave propagation modelling (cf. section 2.2). The formulations to describe the different propagation mechanisms are collected and reproduced in a uniform notation (cf. section 2.3). Emphasis is placed on curved surfaces, because they appear in most tunnel geometries (cf. section 2.3.2.2). Furthermore, a new method to include stochastic rough surface scattering into deterministic ray-optical propagation modelling is derived (cf. section 2.3.3.3). Finally, the handling of multipath propagation, which is always present and particularly severe in a tunnel, together with the possible methods of analysis based on the outcome of ray-optical propagation modelling, conclude this chapter (cf. section 2.4).

2.1 The ray concept

For source-free, isotropic and homogenous media, the well-known (vector) wave equations [Bal89, chap. 3] take the form

$$\nabla^2 \vec{E}(\vec{x}) + \underline{k}^2 \vec{E}(\vec{x}) = 0 \quad (2.1a)$$

$$\nabla^2 \vec{H}(\vec{x}) + \underline{k}^2 \vec{H}(\vec{x}) = 0, \quad (2.1b)$$

if time-harmonic variations of the electromagnetic field according to $e^{j\omega t}$ are assumed, where ω denotes the radial frequency. This is justified, because any

real signal can be approximated by a Fourier-series expansion [Pro89]. For a known spatial distribution of the complex amplitudes $\underline{\vec{E}}(\vec{x})$ and $\underline{\vec{H}}(\vec{x})$, the instantaneous quantities are represented by

$$\vec{E}(\vec{x}, t) = \Re\left\{\underline{\vec{E}}(\vec{x})e^{j\omega t}\right\} \quad (2.2a)$$

$$\vec{H}(\vec{x}, t) = \Re\left\{\underline{\vec{H}}(\vec{x})e^{j\omega t}\right\}, \quad (2.2b)$$

where $\Re\{\cdot\}$ is the real part operator. The underbar denotes complex values, whereas a vector is represented by an arrow. In the following only complex spatial quantities are used and the explicit harmonic time dependency is omitted. The complex wave number \underline{k} is given by

$$\underline{k} = \frac{2\pi}{\lambda_0} \sqrt{\underline{\varepsilon}_r \underline{\mu}_r} = k_0 \sqrt{\underline{\varepsilon}_r \underline{\mu}_r}, \quad (2.3)$$

where k_0 denotes the wave number in vacuum, $\underline{\varepsilon}_r$ the relative (effective) complex permittivity [Bal89, chap. 2]

$$\underline{\varepsilon}_r = \frac{\underline{\varepsilon}}{\varepsilon_0} = \varepsilon_r - j \frac{\sigma_e}{\omega \varepsilon_0} = \varepsilon_r (1 - j \tan \delta_e) \approx \varepsilon_r - j60\lambda_0 \sigma_e \frac{V}{A}, \quad (2.4)$$

and $\underline{\mu}_r$ is the relative complex permeability. Furthermore, $\lambda_0 = c_0/f$ represents the wavelength in vacuum, $c_0 = 2.998 \cdot 10^8 \text{m/s}$ is the speed of light in vacuum, and f is the frequency. In (2.4) $\underline{\varepsilon}$ is the complex permittivity, ε_r the relative permittivity of the medium, σ_e is its equivalent conductivity, $\varepsilon_0 = 8.854 \cdot 10^{-12} \text{As/Vm}$ is the permittivity of vacuum, and $\tan \delta_e$ is the effective electric loss tangent¹ of the medium.

The simplest solution of the vector wave equations (2.1a) and (2.1b), obtained by the method of separation of variables [Bal89, chap. 3], is given by the travelling uniform plane wave

$$\vec{E}(\vec{x}) = \underline{\vec{E}}_0 e^{-j\underline{k}\vec{x}} \quad (2.5a)$$

$$\underline{\vec{H}}(\vec{x}) = \underline{\vec{H}}_0 e^{-j\underline{k}\vec{x}}. \quad (2.5b)$$

$\underline{\vec{E}}_0$ and $\underline{\vec{H}}_0$ are related as follows

$$\underline{\vec{H}}_0 = \frac{\underline{\vec{k}} \times \underline{\vec{E}}_0}{\underline{k} \underline{Z}_w}, \quad (2.6)$$

¹The effective electric loss is the sum of the static and the alternating electric loss [Bal89, chap. 2].

that is both the electric and the magnetic field are perpendicular to each other and to the direction of propagation, referred to as a transverse electromagnetic (TEM) wave. The ratio of the complex amplitudes of the electric to magnetic field is known as the wave impedance

$$\underline{Z}_w = \frac{\underline{E}_0}{\underline{H}_0} = Z_{w0} \sqrt{\frac{\underline{\mu}_r}{\underline{\epsilon}_r}}. \quad (2.7)$$

In free space ($\underline{\epsilon}_r \approx 1$, $\underline{\mu}_r \approx 1$) the wave impedance (also named free-space characteristic impedance) is given by

$$Z_{w0} = \sqrt{\frac{\mu_0}{\epsilon_0}} \approx 120\pi\Omega, \quad (2.8)$$

where $\mu_0 = 4\pi \cdot 10^{-7} \text{Vs/Am}$ denotes the permeability of vacuum.

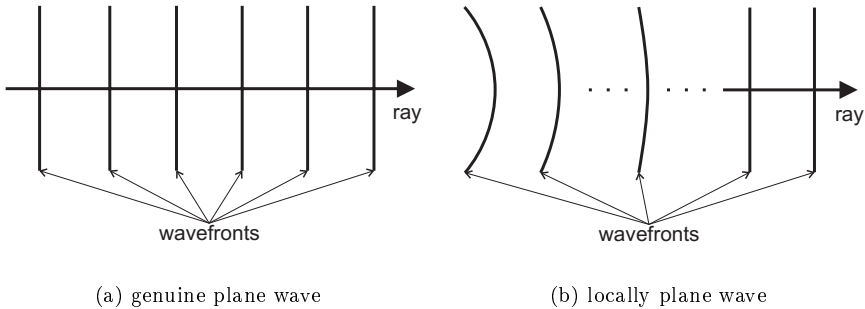


Figure 2.1: The ray concept for (locally) plane waves

The uniform plane wave of (2.5) is now totally characterized by one of its complex vectors $\underline{\vec{E}}_0$ or $\underline{\vec{H}}_0$, its wave number \underline{k} , and its direction of propagation \hat{k} , with $\underline{\vec{k}} = \underline{k}\hat{k}$. Therefore, the wave may be seen as a *ray* (cf. Fig. 2.1(a)) propagating perpendicular to the wavefronts. However, such a plane wave cannot be generated in reality. Provided that the point of observation is sufficiently distant from a point source, the resulting spherical wave can be approximated by a locally plane wave on a small portion of the sphere [GW98, chap. 2], i.e. it still may be interpreted as a ray (cf. Fig. 2.1(b)). This approximation is generally valid for distances greater than $2D^2/\lambda$ from any source², where D denotes the largest dimension of the source's aperture [Bal97, chap. 2].

²Additionally, the extension of the area of observation has to be limited, so that the phase difference between its borders is sufficiently small.

However, the amplitude of this locally plane wave decreases with distance in contrast to the genuine uniform plane wave. The dependency of the amplitude and the phase of the wave (or the ray) from the distance to the source is given by geometrical optics and the Luneburg-Kline high-frequency expansion, as indicated in the following section. In the remainder of this thesis, solely the formalism for the electric field will be stated, since the corresponding magnetic field can be obtained at any time by (2.6).

2.2 Geometrical optics and wave propagation modelling

Geometrical optics (GO) is an approximate high-frequency method for determining wave propagation for incident, reflected, and refracted fields. Because it uses ray concepts, it is often referred to as *ray optics* [Des72, Bal89]. In classical GO, the transport of energy between any two points in an isotropic lossless medium is accomplished using the conservation of energy flux in a tube of rays. The rays between them follow a path according to Fermat's principle [Bal89, chap. 13]. If the background medium is homogenous (like the air in a tunnel), the ray trajectories are straight lines, perpendicular to the wave fronts (cf. Fig. 2.1). Within a tube of rays, also called pencil of rays [Des72], the power energy flux has to remain constant

$$S_0 dA_0 = S dA, \quad (2.9)$$

where S_0 , S denote the radiation densities and dA_0 , dA are the cross-sectional areas of the tube at two different locations separated by a distance s . For TEM waves in a lossless medium S and the electric field strength are related as follows

$$S = \frac{1}{2Z_w} |\vec{E}|^2, \quad (2.10)$$

such that

$$\frac{|\vec{E}|^2}{|\vec{E}_0|^2} = \frac{dA_0}{dA}. \quad (2.11)$$

For an astigmatic tube of rays depicted in Fig. 2.2, being the most general configuration of a ray tube, (2.11) leads to

$$\frac{|\vec{E}|}{|\vec{E}_0|} = \sqrt{\frac{dA_0}{dA}} = \sqrt{\frac{\rho_1 \rho_2}{(\rho_1 + s)(\rho_2 + s)}}, \quad (2.12)$$

where $\rho_{1,2}$ are the radii of curvature of the wave front at $s = 0$, whereas $(\rho_{1,2} + s)$ are the radii at distance s from the reference point. For a positive radius of curvature the wave is diverging, for a negative radius it is converging, i.e. energy is focused. It is apparent from Fig. 2.2 that all rays of the astigmatic tube of rays pass through the same lines PP' and QQ' , which are called caustics. The GO field in such caustics is in principle infinite, because an infinite number of rays pass through it. This behaviour is also reflected in (2.12): at $s = -\rho_{1,2}$ the denominator vanishes and hence the field becomes infinite. In these areas/points, a quantitative evaluation of the actual field is therefore not possible by means of GO, although qualitatively, this focusing of energy can be experimentally verified (cf. chapter 6). A means to overcome this problem is presented in section 3.3.3. If the wave front is spherical, cylindrical and a plane wave the radii are $\rho_1 = \rho_2 = \rho$, $\rho_{1/2} = \infty$, $\rho_{2/1} = \rho$, and $\rho_1 = \rho_2 = \infty$, respectively.

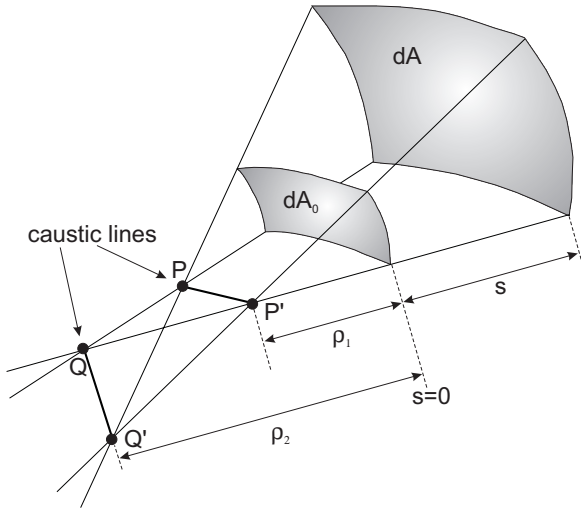


Figure 2.2: Astigmatic tube of rays (cf. [Bal89])

Equation (2.12) only relates the magnitude of the electric field at s to a reference magnitude at $s = 0$. In order to obtain an expression for the actual complex field vector, i.e. including phase and polarization, the Luneburg-Kline high-frequency expansion [Lun64, Kli51, Bal89] is adopted. By restriction to first-order solutions this approach in combination with classical GO leads to

$$\vec{E}(s) = \sqrt{\frac{\rho_1}{\rho_1 + s}} \sqrt{\frac{\rho_2}{\rho_2 + s}} e^{-jk_0 s} \vec{E}_0, \quad (2.13)$$

where \vec{E}_0 is the electric field at the reference point ($s = 0$). Contrary to common usage [MPM90, vD94, Bal89], the square root must be split in order to correctly predict $+90^\circ$ phase jumps each time a caustic is crossed in the direction of propagation [LCL89].

The previous equation is the basis for all following considerations. It is only valid for high frequencies, if the field is to exhibit a ray-optical behaviour, i.e. if the assumption of locally plane waves holds, and all obstacles are large compared to the wavelength. At mobile radio frequencies—which are of matter in this thesis—with corresponding wavelengths of $\lambda_0 < 0.5\text{m}$, this assumption is naturally fulfilled.

In (2.13) the free space dependency of the electric field of a locally plane wave front, i.e. a ray in free space, is stated. This ray is now interacting with its surrounding by means of reflection, scattering etc. The actual total field at a particular point of observation is given by the complex and vectorial superposition of all present rays (or wave fronts) at that point. The overall aim in ray-optical wave propagation modelling is now to determine all relevant rays from a source to the point of observation, to calculate the field strength of each single ray, and to superimpose all rays in order to obtain the total field.

In the following section, the formalisms to calculate the ray propagation phenomena free space propagation, absorption by the atmosphere, specular reflection, and scattering are presented. Diffraction is neglected due to its minor influence compared to reflection in realistic tunnel scenarios, although it can be included in ray-optical wave propagation modelling [Leb91, Cic94, vD94, Küc98] by the geometrical theory of diffraction (GTD) [Kel62] and its extension to the uniform geometrical theory of diffraction (UTD) [PBM80, Jam86, BU88, Bal89, MPM90]. Then multipath propagation is treated and how the different rays are actually combined.

2.3 Propagation phenomena

In this section the phenomena free space propagation, attenuation through the atmosphere, specular reflection at planar and curved surfaces, and scattering at rough surfaces are treated in a way that they can easily be used in conjunction with the ray-optical approach of the previous sections. The goal is to successively take into account the different propagation mechanisms after a ray trajectory is known from a source to a point of observation, in order to determine the field strength of the ray.

2.3.1 Free space propagation and absorption

2.3.1.1 Free space propagation

In a tunnel, the surrounding medium is air, which at a first approximation can be taken as lossless with $\varepsilon_r = \mu_r = 1$. In free space, the dependency of the electric field is then already given by (2.13). Of further interest is the special case of a spherical wave, which is radiated by a point source. For a point source the initial values of the radii of curvature are theoretically zero. Therefore, it is convenient to take the reference value $\vec{\underline{E}}_0$ not at the point source, but at a reference distance. Throughout this thesis the reference distance $s_0 = 1\text{m}$ is taken, resulting in

$$\vec{\underline{E}}(r) = \frac{1\text{m}}{r} e^{-jk_0(r-1\text{m})} \vec{\underline{E}}_0, \quad (2.14)$$

where $r = 1\text{m} + s$ denotes the distance from the point source. In (2.14) it is assumed that the phase at the input port/terminals of the antenna equals $\psi_0 = 0^\circ$. If the transmitting antenna is modelled by a point source with complex vector directional pattern³ $\vec{\underline{C}}_T$ and gain G_T , the reference value is given by [GW98, chap. 2]

$$\vec{\underline{E}}_0 = \sqrt{\frac{P_T G_T Z_{w0}}{2\pi}} \frac{e^{-jk_0 1\text{m}}}{1\text{m}} \vec{\underline{C}}_T, \quad (2.15)$$

where P_T denotes the input power of the transmitting antenna. One should note that (2.14) in conjunction with (2.15) is only valid in the far field of the antenna, but not in the vicinity of the source.

2.3.1.2 Absorption

At certain high frequencies, additional attenuation of the electromagnetic waves in the atmosphere may occur due to resonance absorption of specific gaseous molecules. In the frequency range up to 100GHz this is mainly the case for the self-resonances of water (H_2O) at 22GHz and of oxygen (O_2) at 60GHz [Hal79, ITU676]. This gaseous absorption results in an exponential decay of the field strength with the geometrical optical path length

$$|\vec{\underline{E}}(s)| = e^{-\alpha s} |\vec{\underline{E}}_0|, \quad (2.16)$$

³The complex vector directional pattern defines the phase, polarization and directivity of an antenna [Bal97, GW98].

where α denotes the attenuation coefficient with dimension 1/m. Usually the attenuation is given in dB/km yielding the following relations

$$\frac{A}{\text{dB}} = 20 \lg \left(\frac{|\vec{E}_0|}{|\vec{E}(s)|} \right) = \alpha s 20 \lg(e) \approx 8.69 \alpha s \quad (2.17)$$

or

$$\frac{\alpha}{1/\text{m}} \approx \frac{1}{8.69} \frac{A/\text{dB}}{s/\text{m}} = \frac{1}{8.69 \cdot 10^3} \frac{\alpha_{\text{dB}}}{\text{dB}/\text{km}} \approx 1.15 \cdot 10^{-4} \frac{\alpha_{\text{dB}}}{\text{dB}/\text{km}}. \quad (2.18)$$

At 60GHz for example, which is a promising candidate for the intervehicle communication link [SL90] or mobile broadband systems [COST231], the attenuation has a maximum of $\alpha_{\text{dB}} \approx 15\text{dB}/\text{km}$ [ITU676].

Thus far, propagation in unbounded media has been treated. In a tunnel, however, the rays (and therefore the fields) encounter boundaries, such as the tunnel walls or the ground, and other obstacles like cars or trains, at which the energy is reflected or scattered in different directions. In the next section, reflection at smooth surfaces is treated, followed by some considerations on scattering from rough surfaces.

2.3.2 Reflection at smooth surfaces

Reflection is obviously one of the dominant propagation mechanisms in a tunnel environment. A general solution for the field must satisfy both Maxwell's equations and the boundary conditions. For the special case of two different homogeneous infinite halfspaces, which are separated by a smooth planar interface, the solution is given by the so-called Fresnel reflection and transmission coefficients. The total field is split into an incident, a reflected and a transmitted portion. At the tunnel walls, only the incident and reflected parts are of importance, since it is assumed that the transmitted energy will be completely absorbed by the building materials⁴. The derivation of the Fresnel coefficients are given in almost any textbook on electromagnetic field theory [UMF83, Bal89, Leh90]. Thus, only the results together with the convention used throughout this thesis are stated in the following.

2.3.2.1 Planar surfaces

In a tunnel, reflection normally occurs at boundaries between the air and e.g. the tunnel's walls or ground. Therefore, the original problem with two

⁴Also, as will be seen in section 4.4, the vehicles in the tunnel are supposed to be metallic and hence purely reflective.

arbitrary media can be reduced to the special case of a boundary between vacuum (or air) and a non-magnetic material ($\mu_{r,1} = 1$) with relative effective complex permittivity $\underline{\varepsilon}_{r,1}$. The incident plane wave has to be decomposed into two orthogonal polarizations which are treated separately. The total field is then given by the vector sum of the two components. Figure 2.3 depicts the convention used for this decomposition: the electric field perpendicular to the plane of incidence, i.e. parallel to the interface, is referred to as perpendicular polarization (index: \perp); when the electric field is parallel to the plane of incidence, it is referred to as parallel polarization (index: \parallel). The plane of incidence is spanned by the normal vector of the interface between the two media \hat{n} and the unit vector in the direction of incidence of the plane wave (or ray) \hat{k}^i . The superscripts i and r refer to the incident and the reflected values, respectively.

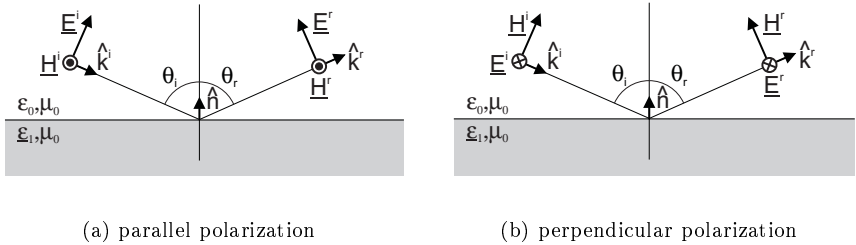


Figure 2.3: Reflection of an incident plane wave (or ray) at a smooth plane boundary between air ($\varepsilon_{r,0} = 1, \mu_{r,0} = 1$) and a homogenous dielectric infinite halfspace with $\underline{\varepsilon}_{r,1}$ and $\mu_{r,1} = 1$

The angle of reflection is determined according to Snell's law of reflection

$$\theta_r = \theta_i = \arccos(-\hat{k}^i \cdot \hat{n}) = \arccos(\hat{k}^r \cdot \hat{n}). \quad (2.19)$$

The reflection coefficients $\underline{R}_{\parallel, \perp}$, relating the incident and the reflected fields according to

$$\underline{R}_{\parallel, \perp} = \frac{\underline{E}_{\parallel, \perp}^r}{\underline{E}_{\parallel, \perp}^i} = \frac{\underline{H}_{\parallel, \perp}^r}{\underline{H}_{\parallel, \perp}^i}, \quad (2.20)$$

are given by

$$\underline{R}_{\parallel}(\theta_i, \underline{\varepsilon}_{r,1}) = \frac{\underline{\varepsilon}_{r,1} \cos \theta_i - \sqrt{\underline{\varepsilon}_{r,1} - \sin^2 \theta_i}}{\underline{\varepsilon}_{r,1} \cos \theta_i + \sqrt{\underline{\varepsilon}_{r,1} - \sin^2 \theta_i}}, \quad (2.21)$$

$$\underline{R}_\perp(\theta_i, \underline{\varepsilon}_{r,1}) = \frac{\cos \theta_i - \sqrt{\underline{\varepsilon}_{r,1} - \sin^2 \theta_i}}{\cos \theta_i + \sqrt{\underline{\varepsilon}_{r,1} - \sin^2 \theta_i}}. \quad (2.22)$$

As previously indicated, the transmitted portion of the wave is assumed to be totally absorbed and hence not further treated in this thesis. If a more confined model for vehicles than the one of section 4.4 is used, transmission needs to be considered. Transmission can be described in analogy to the reflection problem according to Snell's law of transmission and by transmission coefficients, which are similar to those in (2.21) and (2.22) [UMF83, Bal89, Leh90].

The following special cases are needed in parts of the thesis. First, at an ideal PEC metallic surface with $\sigma \rightarrow \infty$, the reflection coefficients are independent of the angle of incidence

$$\underline{R}_\parallel = R_\parallel = 1, \quad \underline{R}_\perp = R_\perp = -1. \quad (2.23)$$

Furthermore, an ideal corrugated PEC metallic surface is utilized (cf. section 5.2.2) [Kil90], with

$$\underline{R}_\parallel = \underline{R}_\perp = R = -1. \quad (2.24)$$

The previous equation is also valid for a non-PEC halfspace at grazing incidence ($\theta_i \rightarrow 90^\circ$), which is important at large distances from the transmitter. In this case the coefficients are independent of the electrical properties of the dielectric material.

The separation of the incident field into a parallel and a perpendicular component allows to treat reflection by (2.19)–(2.24). This separation, however, depends on the incidence direction \hat{k}^i and the orientation of the reflecting surface given by \hat{n} , and is therefore a “local” transformation. A compact formulation is achieved by introducing the dyadic reflection coefficient $\underline{\underline{R}}$ so that the reflected field at Q_R can be obtained from the incident field at Q_R via

$$\underline{\underline{E}}^r(Q_R) = \underline{\underline{R}} \cdot \underline{\underline{E}}^i(Q_R). \quad (2.25)$$

The dyadic $\underline{\underline{R}}$ is given by

$$\underline{\underline{R}} = \underline{R}_\parallel \hat{e}_\parallel^r \hat{e}_\parallel^i + \underline{R}_\perp \hat{e}_\perp^r \hat{e}_\perp^i, \quad (2.26)$$

with

$$\hat{e}_\perp^i = \hat{e}_\perp^r = \frac{\hat{n} \times \hat{k}^i}{|\hat{n} \times \hat{k}^i|} \quad (2.27a)$$

$$\hat{e}_\parallel^i = \hat{k}^i \times \hat{e}_\perp^i, \quad \hat{e}_\parallel^r = \hat{k}^r \times \hat{e}_\perp^r. \quad (2.27b)$$

Strictly speaking, the aforementioned formulas are only valid for an uniform plane wave incident on an infinite smooth planar boundary, but they may still be adopted for locally plane waves (or rays), if the dimensions of the interface (and therefore obstacles) are large compared to the wavelength.

2.3.2.2 Curved surfaces

If the interface is curved, like arched cross sections or bends of a tunnel, reflection can still be treated by ray-optical methods provided that the radii of curvature of the surface are large compared to the wavelength [KP74, Bal89]. The incident ray, representing a tube of rays or a locally plane wave front, is simply reflected at the tangential plane in the intersection point of the incident ray trajectory and the surface. The angle of reflection is again given by Snell's law of reflection and equals the incident angle determined by the normal \hat{n} of the tangential plane and the direction of propagation of the incident ray. In contrast to the reflection of a plane wave at a planar boundary, however, one must consider that the principal radii of curvature of the reflected tube of rays are in general different from the ones of the incident tube of rays due to the curvature of the surface. In other words, the tube of rays may be focused or defocused by the reflecting surface.

Figure 2.4 depicts the geometry of the reflection at a curved surface, where $\rho_{1,2}^i$ and $\rho_{1,2}^r$ denote the principal radii of curvature of the incident ray tube and the radii after reflection, respectively. The reference point in both cases is the point of reflection Q_R . For a given electric field \vec{E}^i of the incident wave at the point of reflection Q_R , the reflected field at a distance s from the point of reflection becomes

$$\vec{E}^r(s) = \sqrt{\frac{\rho_1^r}{\rho_1^r + s}} \sqrt{\frac{\rho_2^r}{\rho_2^r + s}} e^{-jk_0 s} \bar{\bar{R}} \cdot \vec{E}^i(Q_R). \quad (2.28)$$

If the electric field vectors are decomposed in parallel and perpendicular polarization referring to the plane of incidence (spanned by \hat{n} and \hat{k}^i), the dyadic reflection coefficient $\bar{\bar{R}}$ reduces to a diagonal matrix with components \bar{R}_{\parallel} and \bar{R}_{\perp} . The principal radii of curvature $\rho_{1,2}^r$ are related to the principal radii of the incident wave front $\rho_{1,2}^i$, the angle of incidence, and the curvature of the reflecting surface at Q_R in a non-trivial way. The equations for calculating $\rho_{1,2}^r$ are taken from [KP74, Bal89] and are summarized in appendix A. For the special case of a planar surface, the principal radii of the tube of rays remain unchanged, i.e. $\rho_{1,2}^r = \rho_{1,2}^i$.

Thus far, perfectly smooth surfaces were assumed. The impact of surface roughness on wave propagation and its classification is treated in the following section.

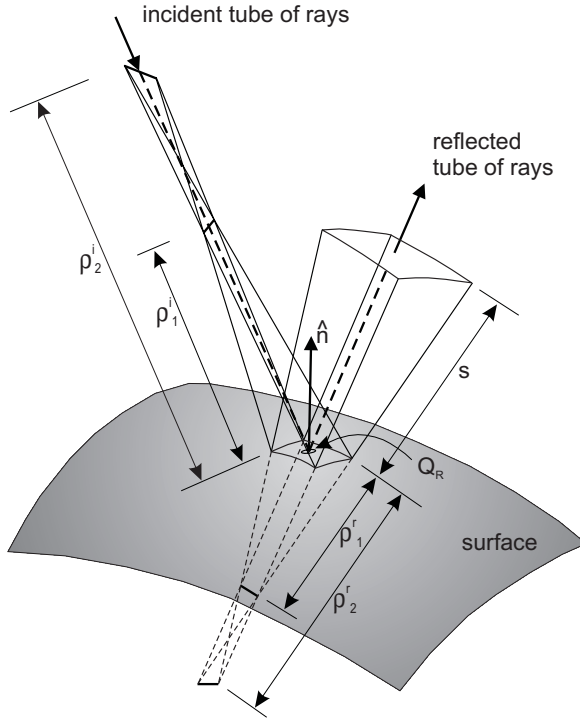


Figure 2.4: Ray optical reflection of an astigmatic tube of rays from a curved surface (cf. [Bal89])

2.3.3 Scattering from rough surfaces

For infinite perfectly smooth surfaces, the total energy of a ray is reflected in the specular direction, given by Snell's law of reflection as indicated in the previous section. In reality however, some portion of the energy is scattered in other directions than the specular one due to the roughness of the surface. The scattered energy is generally split in the so-called coherent and incoherent components [RB⁺70, UMF83, GW98]. The coherent part is defined by the mean value of the scattered field, while the incoherent part characterizes the deviation of this mean. The coherent component decreases with increasing surface roughness, whereas the incoherent (or diffuse) component becomes more significant. Before attempting to tackle the problem of scattering, one must quantify the roughness of a surface.

2.3.3.1 Roughness criteria

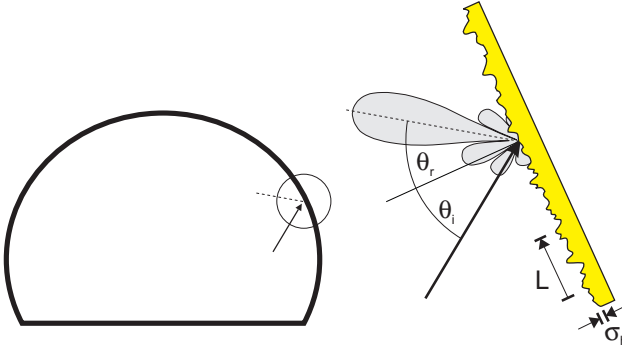


Figure 2.5: Characterization of a rough surface by standard deviation σ_h of the surface height and by its correlation length L

For statistically rough surfaces, which generally have an arbitrary distribution of surface heights, a geometrical measure of the roughness is given by the standard deviation σ_h of the surface height and by its correlation length L (cf. Fig. 2.5). The first is a measure for the variations of the height against its mean value, the second is a simple measure for the statistical dependence of the heights at two different points on the surface. The greater σ_h and the smaller L , the rougher the surface in mechanical terms. For the scattering of an electromagnetic wave, however, not the absolute value but the relation between σ_h and the wavelength λ_0 matters. A heuristical but widely accepted criterion for the roughness of a surface with respect to the wavelength is given by the Fraunhofer criterion, namely that a surface can be considered smooth for [RB⁺70, BS63, UMF83]

$$\sigma_h < \frac{\lambda_0}{32 \cos \theta_i}. \quad (2.29)$$

Equation (2.29) results from the demand that the root mean square (RMS) phase difference between two rays reflected at two different heights on the surface must be smaller than $\pi/8$ in the far field in order to combine coherently, i.e. the rays are almost “in phase”, as in the case of a perfectly smooth surface.

2.3.3.2 Slightly rough surfaces: the modified Fresnel reflection coefficients

If the surface has only a slight roughness, i.e. $\sigma_h \ll \lambda_0$, the diffuse component can be neglected and the scattering of the coherent component may be well

approximated by a reflection. However, the power density in the specular direction is reduced due to the partial cancellation of the statistically varying phases, compared to the pure specular reflection discussed in section 2.3.2. In this case, the so-called modified Fresnel reflection coefficients [BS63, UMF83, LFR96] can be adopted, which approximate the reduction of the magnitude of the field by

$$\underline{R}_{\parallel,\perp}^{mod} = \underline{R}_{\parallel,\perp} e^{-8\pi^2(\sigma_h/\lambda_0)^2 \cos^2\theta_i}. \quad (2.30)$$

According to (2.29) the ratio of the modified to the original Fresnel reflection coefficients at the Fraunhofer limit is $\underline{R}^{mod}/\underline{R} = 0.926$ or -0.67dB . As a rule of thumb, (2.30) is applicable up to roughly 4 times the roughness allowed by (2.29), known as the Rayleigh criterion⁵. At the Rayleigh limit $\underline{R}^{mod}/\underline{R} = 0.291$ or -10.7dB .

The roughness σ_h of common building materials in tunnels is in the lower millimeter range (e.g. $\leq 1\text{mm}$ for tarred road surfaces [Sch98, LS99] and for smooth concrete surfaces [LS99]). Hence, the modified reflection coefficients are well applicable for standard mobile communications frequency ranges. For millimeter waves or if the roughness exceeds the millimeter range, the diffuse scattering can no longer be neglected. An (almost) exact solution for the scattering of a statistically rough surface can only be obtained numerically by computationally costly Monte-Carlo methods [AF78], [WSC97, with further references]. Analytical scattering models [BS63, RB⁺70, UMF83, Fun94], using the statistical parameters of the surface σ_h , L etc., provide only mean values for the coherent and/or the diffuse components. An approach, which combines these two methods and which suits well with the stochastic ray-launching approach of section 4.2, is presented in the following section.

2.3.3.3 Stochastic scattering approach

The novel stochastic scattering approach (SSA) is based on the same assumptions as the Kirchhoff or the physical optics (PO) formulation for surface scattering. These theories are applicable to surfaces with gentle undulations, whose horizontal dimensions are large compared with the incident wavelength. Hence, the total field at any point on the surface can be computed as if the ray (or the wave) is impinging at the tangential plane in that point [UMF83]. This tangential plane approximation is the basic assumption for the Kirchhoff methods. The difference to specular reflection, where all elementary waves of an incident uniform plane wave are reflected at the same ideally smooth planar boundary, lies in the different orientation of the tangential planes in

⁵(2.30) actually results from the scalar Kirchhoff approximation, which is valid for the conditions given in (2.44) and (5.12).

space and the varying heights at the respective points of reflection for each elementary wave. Thus, depolarization and scattering in directions other than the specular one may occur.

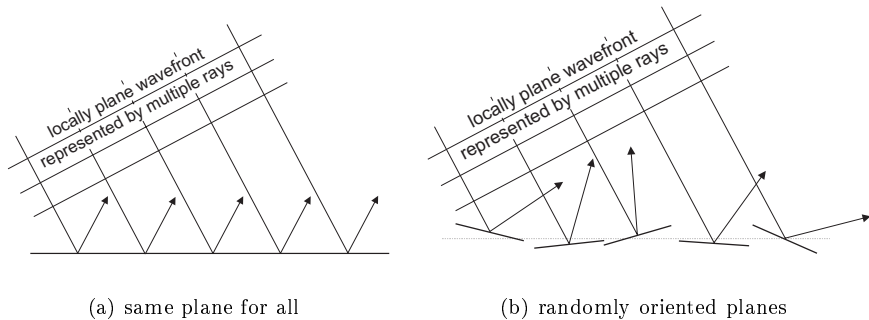


Figure 2.6: The stochastic scattering approach: reflection at randomly oriented tangential planes for each discrete ray (here only a 2D representation is shown for simplicity)

The main idea of the stochastic scattering approach is now based on the stochastic ray launching of sections 3.2.2 and 4.2, where each locally plane wave front is actually represented by multiple discrete rays instead of only one ray (cf. Fig. 2.6). Instead of reflecting all these discrete rays at the same boundary plane, the orientation of the plane (its normal vector) and its position (its height) are varied statistically for each discrete ray and for each reflection. In that sense each discrete ray is seen as a representative of an elementary wave for the locally plane incident wave front. The variations of the local⁶ tangential planes naturally have to be related to the properties of the rough surface, which will be derived in the following.

The surface height of most man-made materials is (at least approximately) normally distributed [BS63, LS99]. Let the height h be normally distributed with zero mean and variance σ_h , i.e. the distribution of the height is given by

$$p_h(h) = \frac{1}{\sqrt{2\pi}\sigma_h} e^{-\frac{1}{2}\left(\frac{h}{\sigma_h}\right)^2}. \quad (2.31)$$

Let the autocorrelation coefficient $\phi_{hh}(l)$ be Gaussian

$$\phi_{hh}(l) = e^{-l^2/L^2}, \quad (2.32)$$

⁶The tangential planes are “local” in the sense that for each discrete ray a different tangential plane is generated.

which gives the correlation between the random height h at two points on the surface separated by a distance l . L is the correlation length, for which (2.32) equals $1/e$. Then, according to [BS63, appendix D], [Hag66], [UMF83, appendix 12F], the distribution of the slopes ϑ of a normally distributed one-dimensional (1D) surface $h(x)$, defined by

$$\tan \vartheta = h' = \frac{dh}{dx}, \quad (2.33)$$

is again normally distributed with zero mean and variance

$$\sigma_{h'}^2 = -\sigma_h^2 \phi''_{hh}(0) = \frac{2\sigma_h^2}{L^2}. \quad (2.34)$$

Hence the distribution of h' equals

$$p_{h'}(h') = \frac{L}{2\sigma_h\sqrt{\pi}} e^{-\left(\frac{Lh'}{2\sigma_h}\right)^2}. \quad (2.35)$$

Using the relation [Pap84, MG92]

$$p_a(a)|da| = p_b(b)|db| \quad (2.36)$$

to transform (2.35) to the random variable ϑ , the distribution of the slopes becomes

$$p_{\vartheta}(\vartheta) = \frac{L}{2\sigma_h\sqrt{\pi}\cos^2\vartheta} e^{-\left(\frac{L\tan\vartheta}{2\sigma_h}\right)^2}. \quad (2.37)$$

For any random variable ξ , the second central moment (variance) is given by

$$\langle (\xi - \langle \xi \rangle)^2 \rangle = \langle \xi^2 \rangle - \langle \xi \rangle^2, \quad (2.38)$$

where $\langle \cdot \rangle$ is the expectation operator. With (2.38) and $\langle h' \rangle = 0$, it follows that the root mean square (RMS) gradient (often misleadingly called ‘‘RMS slope’’) is given by the root of (2.34)

$$\sqrt{\langle h'^2 \rangle} = \sigma_{h'} = \frac{\sqrt{2}\sigma_h}{L}. \quad (2.39)$$

For a two-dimensional (2D) isotropic rough surface with $h = h(x, y)$, which is described by (2.31) and (2.32), a measure for the slope magnitude of the irregularities forming the rough surface is therefore given by [BS63, RB⁺70]

$$s = \langle h_x'^2 + h_y'^2 \rangle^{\frac{1}{2}} = \frac{2\sigma_h}{L}. \quad (2.40)$$

The previous equation implies a direct geometrical interpretation. A plane through the origin of random orientation and the same mean slope having the same statistical properties as the considered Gaussian rough surface is shown in Fig. 2.7. It is determined by three points $P_0(0, 0, 0)$, $P_1(L/\sqrt{2}, 0, \zeta_x)$ and $P_2(0, L/\sqrt{2}, \zeta_y)$ in cartesian coordinates. $\zeta_{x,y}$ are two independent Gaussian random variables with zero mean and variance σ_h . Equivalently the plane is defined by P_0 and its normal vector

$$\vec{n} = \left(-\frac{\sqrt{2}\zeta_x}{L}, -\frac{\sqrt{2}\zeta_y}{L}, 1 \right)^T = (-h'_x, -h'_y, 1)^T. \quad (2.41)$$

The first two components of the normal vector represent the negative gradients of the plane $-h'_x$ and $-h'_y$ in the x - and y -directions, respectively. It is easily verified that these gradients are distributed according to (2.35). The RMS

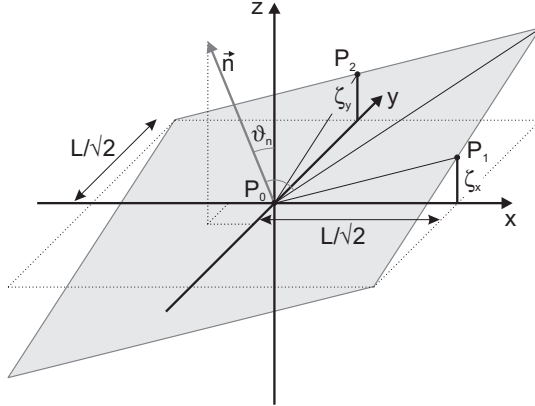


Figure 2.7: Local tangential plane of random orientation with the same statistical properties as a Gaussian rough surface with a given mean gradient

gradient of the plane is given by

$$\langle \tan^2 \vartheta_n \rangle^{\frac{1}{2}} = \left\langle \left(\frac{\sqrt{2}\zeta_x}{L} \right)^2 + \left(\frac{\sqrt{2}\zeta_y}{L} \right)^2 \right\rangle^{\frac{1}{2}} = \frac{\sqrt{2}}{L} \langle \zeta_x^2 + \zeta_y^2 \rangle^{\frac{1}{2}} = \frac{2\sigma_h}{L}. \quad (2.42)$$

Equation (2.42) uses the first moment of a central two-dimensional chi-square distribution

$$\langle \xi_1^2 + \xi_2^2 \rangle = 2\sigma_\xi^2, \quad (2.43)$$

where the $\xi_{1/2}$ are statistically independent, normally distributed random variables with zero mean and variance σ_ξ . It should be noted that the absolute

value of the gradient $|\tan \vartheta_n| = \sqrt{\tan^2 \vartheta_n}$ is Rayleigh distributed with mean $\frac{\sqrt{\pi}}{L} \sigma_h$. The agreement of (2.42) and (2.40) proves the equivalence of the statistical properties of the slopes of the randomly oriented plane in Fig. 2.7 and a Gaussian rough surface. This means that the variation of the orientation of the local tangential planes in the stochastic scattering process is to be performed according to (2.41). The local height variation of the reflection point is naturally performed according to a Gaussian law with zero mean and variance σ_h^2 .

By applying the stochastic scattering approach, the inclusion of random (but directive) surface scattering into ray-optical propagation modelling becomes possible. The purely deterministic GO modelling is expanded by a “stochastic” component, resulting in varying prediction results; thus allowing for the first time to account for non-deterministic scattering in ray-optical modelling. The results can be used in the generation of time series for the purpose of system performance evaluation, which otherwise could only be obtained by the assumption of ergodicity with respect to time and space [Kür93, Bec96].

In contrast to the two Kirchhoff models⁷, which are only valid for either slightly rough or very rough surfaces, the stochastic scattering approach includes both the coherent and incoherent components at the same time. Its validity conditions are only determined by the tangential plane approximation [UMF83]

$$\frac{L^2}{2.76\sigma_h} > \lambda_0, \quad \text{and} \quad L > \frac{6}{2\pi}\lambda_0. \quad (2.44)$$

The first condition in (2.44) calls for the mean radius of curvature of the random rough surface to be large compared to the wavelength, the second calls for a large correlation length compared to the wavelength. Multiple scattering between various parts of the surface is neglected in the stochastic scattering approach, like in the Kirchhoff models. A comparison of the proposed stochastic scattering approach with the Kirchhoff models is given in section 5.3.

Note that an empirical approach, which uses randomly changed normal vectors of the walls to take surface roughness into account, was proposed in [LL98].

2.4 Multipath propagation and analysis

In the previous section the different (relevant) propagation mechanisms and their integration into ray-optical propagation modelling was presented. Each

⁷The Kirchhoff model with scalar approximation and the Kirchhoff model with stationary phase approximation (cf. section 5.3).

ray experiences on its way from the transmitter to the receiver a certain attenuation, depolarization, phase shift, and delay, due to the different aforementioned propagation effects. Moving objects, as vehicles or trains, or the motion of transmitter and/or receiver, additionally introduce a Doppler shift for each ray. In the complex environment of a tunnel, there are generally several ray paths from the transmitter to the receiver, each representing a physical propagation path for the corresponding electromagnetic wave. For the described multipath propagation, the different impinging rays interfere, contributing to the resulting field at the receiver. How to perform this combination of rays and what other consequences result from multipath propagation is treated in the following.

First, the formalism for a single propagation path is reproduced followed by the generalization to multipath propagation. Then the broadband channel signatures frequency response, impulse response, delay-Doppler-spread function, the parameters delay spread and Doppler spread are given as functions of the multipath components.

2.4.1 Formal description of a propagation path

On each propagation path from the transmitter to the receiver, a ray may experience several propagation phenomena in any order. The starting point for each ray is the radiated (far) field of the transmitting antenna, which is given by (2.14) and (2.15)

$$\vec{\underline{E}}(r) = \sqrt{\frac{P_T G_T Z_{w0}}{2\pi}} \frac{e^{-jk_0 r}}{r} \vec{\underline{C}}_T = e^{-jk_0(r-1m)} \underline{T}_{D,0} \vec{\underline{E}}_0, \quad (2.45)$$

where $\underline{T}_{D,0} = 1m/r$ denotes the divergence transfer factor, which is a measure for the divergence of the tube of rays. At each interaction of the ray with an obstacle, the field strength is multiplied by a dyadic propagation transfer factor $\underline{\bar{T}}_{P,j}$, which accounts for the actual propagation effect, and by $\underline{T}_{D,j}$, which accounts for a change in divergence due to the interaction. For a reflection, $\underline{\bar{T}}_{P,j}$ is given by the dyadic reflection coefficient and $\underline{T}_{D,j}$ by the possibly complex square roots⁸ in (2.28). Considering the absorption case, $\underline{\bar{T}}_{P,j}$ reduces to a scalar, given by the exponential term in (2.16), and $\underline{T}_{D,j} = 1$. Cascading all transfer factors—and therefore all occurring propagation phenomena—leads

⁸The square roots may be complex after crossing a caustic (cf. section 2.3.2.)

to the field strength of the ray at the receiver

$$\vec{\underline{E}}_R = \vec{\underline{E}}(r) = e^{-jk_0(r-1m)} \underbrace{\left(\prod_{j=m}^0 \underline{T}_{D,j} \vec{\underline{T}}_{P,j} \right)}_{\vec{\underline{T}} = \underline{T}_D \vec{\underline{T}}_P} \cdot \vec{\underline{E}}_0, \quad (2.46)$$

where r denotes the total unfolded path length and m the number of ray interactions. The free-space propagation transfer factor $\vec{\underline{T}}_{P,0}$ in (2.46) equals the unit dyadic. As indicated in (2.46), all transfer factors can be combined to the total (dyadic) transfer factor $\vec{\underline{T}} = \underline{T}_D \vec{\underline{T}}_P$, which, together with the phase factor $e^{-jk_0(r-1m)}$, completely characterizes the propagation of the ray.

The electric field can only be determined indirectly via a receiving antenna by its induced voltage \underline{V}_R at the output port/terminals of the antenna and/or the amount of power P_R delivered to its load. The effective area of the receiving antenna is given by [Bal97, GW98, chaps. 2]

$$A_{eR} = \frac{\lambda_0^2}{4\pi} G_R |\vec{\underline{C}}_R|^2. \quad (2.47)$$

The relation between the maximum available power P , the (open-circuit) voltage \underline{V} , and the internal impedance of a generator \underline{Z} under complex conjugate matching is

$$P = \frac{|\underline{V}|^2}{8\Re\{\underline{Z}\}}. \quad (2.48)$$

By means of (2.10), (2.47), (2.48), and a straightforward extension for arbitrary orientation of the receiving antenna⁹ one obtains

$$\underline{V}_R = \sqrt{\frac{\lambda_0^2}{4\pi} G_R \frac{4\Re\{\underline{Z}_R\}}{Z_{w0}}} \vec{\underline{C}}_R \cdot \vec{\underline{E}}_R, \quad (2.49)$$

where G_R , $\vec{\underline{C}}_R$ and Z_R denote the gain of the receiving antenna, the complex vector directional pattern and the impedance, respectively. Consequently, the power delivered to the load equals [Bal97, GW98]

$$P_R = \frac{\lambda_0^2}{8\pi} G_R \frac{1}{Z_{w0}} |\vec{\underline{C}}_R \cdot \vec{\underline{E}}_R|^2 = \left(\frac{\lambda_0}{4\pi 1m} \right)^2 G_R G_T P_T \left| \vec{\underline{C}}_R \cdot \underbrace{\underline{T}_D \vec{\underline{T}}_P}_{\vec{\underline{T}}} \cdot \vec{\underline{C}}_T \right|^2. \quad (2.50)$$

⁹I.e. not necessarily polarization-matching.

In the previous two equations it is assumed that the receiving antenna is matched to its load. In chapter 3.3, a modified form of (2.50) is used to simplify the notation

$$P_R = \left(\frac{\lambda_0}{4\pi 1\text{m}} \right)^2 G_R G_T P_T \underbrace{T_D^2 T_P^2}_{T^2}. \quad (2.51)$$

In (2.51), the “real equivalents” T_D and T_P of the complex divergence transfer factor \underline{T}_D and the complex dyadic propagation transfer factor $\underline{\bar{T}}_P$ after reception are introduced with

$$T_D = |\underline{T}_D| \quad (2.52a)$$

$$T_P = |\underline{\bar{C}}_R \cdot \underline{\bar{T}}_P \cdot \underline{\bar{C}}_T|. \quad (2.52b)$$

For the direct or line-of-sight (LOS) path from the transmitter to the receiver with $T_D = T_{D,0}$ and $T_P = |\underline{\bar{C}}_R \cdot \underline{\bar{C}}_T|$, (2.51) (respectively (2.50)) reduces to the well-known Friis transmission equation [Bal97]. Equations (2.46)–(2.52) are valid for any propagation path between the transmitting and receiving antennas.

2.4.2 Multipath propagation

In the previous section, the propagation path of a single ray (or wave front) at a given frequency was studied. In general, a large number of rays n reach the receiver on different propagation paths and interfere, especially in confined spaces as tunnels. The overall electric field at the receiver $\underline{\bar{E}}_{R,tot}$ is therefore given by the vector sum of all $\underline{\bar{E}}_{R,l}$. The individual fields $\underline{\bar{E}}_{R,l}$ of the multipath components l , with $l = 1, \dots, n$, are given by (2.46). The total induced voltage $\underline{V}_{R,tot}$ at the output port/terminals of the receiving antenna is obtained by the summation of all contributing complex voltages $\underline{V}_{R,l}$ from (2.49), i.e.,

$$\underline{V}_{R,tot} = \sum_{l=1}^n \underline{V}_{R,l}. \quad (2.53)$$

Equivalently, the total power delivered to a matched load is

$$P_{R,tot}^c = \frac{|\underline{V}_{R,tot}|^2}{8\Re\{\underline{Z}_R\}} = \frac{1}{8\Re\{\underline{Z}_R\}} \left| \sum_{l=1}^n \underline{V}_{R,l} \right|^2 \quad (2.54a)$$

$$= \left(\frac{\lambda_0}{4\pi 1\text{m}} \right)^2 G_R G_T P_T \left| \sum_{l=1}^n e^{-jk_0 r_l} \underline{\bar{C}}_{R,l} \cdot \underline{\bar{T}}_l \cdot \underline{\bar{C}}_{T,l} \right|^2. \quad (2.54b)$$

Here, the complex voltage components are summed up coherently (indicated by the superscript c), which requires perfect knowledge of the amplitude and phase of each single $\underline{V}_{R,l}$. However, already small variations in the geometry of the propagation environment on the order of $\lambda_0/2$, like the dimension of a tunnel's cross section or a receiver location, generally lead to a significant change in the phase of each multipath component¹⁰. Therefore, it is often useful to average the received power over a certain range. This averaging can be easily approximated, if the complex voltages of the multipath components are substituted with the respective received powers $P_{R,l}$, yielding

$$\overline{P}_{R,tot} = \frac{1}{8\Re\{\underline{Z}_R\}} \overline{\left| \sum_{l=1}^n \underline{V}_{R,l} \right|^2} \approx \frac{1}{8\Re\{\underline{Z}_R\}} \sum_{l=1}^n |\underline{V}_{R,l}|^2 = \sum_{l=1}^n P_{R,l} = P_{R,tot}^i. \quad (2.55)$$

This incoherent summation (indicated by the superscript i), which is also termed power sum, equals the averaged received power $\overline{P}_{R,tot}$, if the phases of the voltage components are completely uncorrelated, and if the amplitudes are constant. Using the simplified formalism of the previous section, one can write

$$P_{R,tot}^i = \left(\frac{\lambda_0}{4\pi 1\text{m}} \right)^2 G_R G_T P_T \sum_{l=1}^n T_l^2. \quad (2.56)$$

Again, (2.56) presents only the mean received power. Locally, the instantaneous values may differ, according to the values obtained by (2.54).

2.4.3 Broadband analysis and channel parameters

One of the major advantages of ray-optical wave propagation modelling is the ability to obtain broadband channel parameters in addition to the narrowband field strength/received power prediction. This is possible due to the distinction of each ray and its attributes delay, attenuation, phase shift, and Doppler shift. Additionally, the fully polarimetric modelling allows to investigate the influence of different antennas and transmission schemes without increase in computational costs.

Originally, the calculation is performed at one single frequency, i.e. for harmonic excitation. For non-dispersive propagation paths, i.e. under the assumption that the phenomena reflection, scattering, and attenuation are similar (if not equal) within the considered bandwidth, the "single frequency" result of each ray can be used for the entire frequency band. However, the

¹⁰Whereas the amplitude remains almost constant.

interfering multipath components result in a frequency-selective behaviour of the channel, because the absolute phases of the single rays depend on the traversed path length and the frequency.

Furthermore, the channel is also time-variant. The reason for time-variance in a tunnel is movement of obstacles, transmitters, and/or receivers. Movement leads to a Doppler shift ν for each ray resulting in a Doppler spread (and/or shift) after multipath reception. Modelling the Doppler shift is incorporated in the ray-optical approach in a straightforward way: each ray carries its actual Doppler shift in addition to the field strength information. Consequently, the output of a ray-optical propagation prediction is a polarimetric Doppler-resolved impulse response with additional angle-of-arrival information, from which the power delay profile (PDP), the Doppler spectrum, and the angular spectrum (AS) can be derived. In the following, the explicit connection between ray-tracing results and the channel functions frequency response, impulse response, and delay-Doppler-spread function are pointed out, together with the general parameters delay spread and Doppler spread.

2.4.3.1 Frequency and impulse response of the transmission channel

The frequency response of the transmission channel $\underline{H}(f)$ can be defined by the ratio [GW98]

$$\underline{H}(f) = \frac{\underline{V}_{R,tot}(f)}{\underline{V}_T(f)}, \quad (2.57)$$

where \underline{V}_T denotes the (open-circuit) voltage at the input port/terminals of the transmitting antenna. Assuming complex conjugate impedance matching, \underline{H} follows from (2.53) for positive frequencies $f > 0$

$$\underline{H}(f) = \sqrt{\left(\frac{\lambda_0}{4\pi 1\text{m}}\right)^2 G_R G_T} \sum_{l=1}^n \left\{ e^{-j2\pi f \tau_l} \underline{\vec{C}}_{R,l} \cdot \underline{\vec{T}}_l \cdot \underline{\vec{C}}_{T,l} \right\} \quad (2.58a)$$

$$= \sum_{l=1}^n \underline{a}_l e^{-j2\pi f \tau_l}. \quad (2.58b)$$

The ratio $\tau_l = r_l/c_0$ denotes the delay of the l^{th} multipath component. Except for the wavelength, the only explicit frequency dependence of the multipath components in (2.58) results from the delay term. Their complex amplitudes \underline{a}_l are assumed to be independent of f .

Using the notation for bandpass signals and systems with their equivalent lowpass representation [Pro89, chap. 4], the lowpass impulse response $\underline{h}^{LP}(\tau)$

of the channel is obtained by the inverse Fourier transform of (2.58b) shifted by $-f_0$, leading to

$$\underline{h}^{LP}(\tau) = \sum_{l=1}^n a_l e^{-j2\pi f_0 \tau_l} \delta(\tau - \tau_l). \quad (2.59)$$

The real-valued bandpass impulse response is therefore given by

$$h(\tau) = 2 \Re\{\underline{h}^{LP}(\tau) e^{j2\pi f_0 \tau}\}. \quad (2.60)$$

The above equations hold for a channel with infinite bandwidth. For band-limited systems, the dirac function in (2.59) has to be replaced by the actual filter function of the system, which includes both the transmitting and receiving blocks.

2.4.3.2 The delay-Doppler-spread function

The aforementioned channel functions reflect the frequency-selective behaviour of the channel. The time-variant nature of the channel is integrated in deterministic wave propagation modelling by means of movement and therefrom resulting Doppler shifts. The Doppler shift ν_j experienced by a ray at the interaction with a moving obstacle is illustrated in Fig. 2.8.

Assuming a fixed direction of propagation \hat{k}_j , the Doppler shift of the ray is given by

$$\nu_j = -\frac{\vec{v}_j \cdot \hat{k}_j}{c_0} f_j, \quad (2.61)$$

where \vec{v}_j denotes the velocity vector of the obstacle, $-\vec{v}_j \cdot \hat{k}_j$ is the speed in the direction of propagation, and f_j is the frequency before the interaction. In the case of a moving receiver (or transmitter), (2.61) states the total experienced Doppler shift. However in a strict sense, if reflections at moving obstacles are considered, the Doppler shift of the incident (ν^i) and the reflected ray (ν^r) have to be treated separately. For reflections at a planar surface moving in the direction of its normal vector (cf. Fig. 2.8(b)), the Doppler shift is given by

$$\begin{aligned} \nu_j &= \nu_j^i + \nu_j^r = -\frac{\vec{v}_j \cdot \hat{k}_j^i}{c_0} f_j + \frac{\vec{v}_j \cdot \hat{k}_j^r}{c_0} (f_j + \nu_j^i) \\ &= \left(-2 \frac{\vec{v}_j \cdot \hat{k}_j^i}{c_0} + \underbrace{\left(\frac{\vec{v}_j \cdot \hat{k}_j^i}{c_0} \right)^2}_{\ll 1} \right) f_j \approx -2 \frac{\vec{v}_j \cdot \hat{k}_j^i}{c_0} f_j = 2\nu_j^i. \end{aligned} \quad (2.62)$$

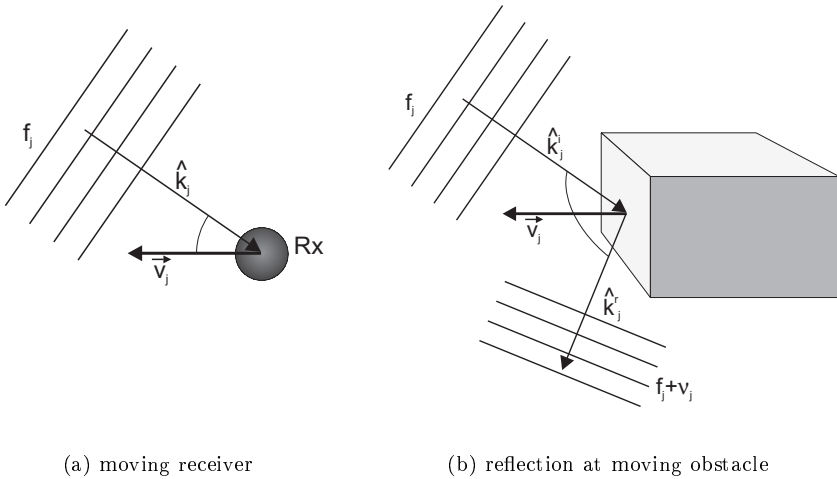


Figure 2.8: Ray interaction with moving receiver or obstacle of speed \vec{v}_j , resulting in a Doppler shift ν_j for the ray

The overall Doppler shift of a ray is obtained by the sum of all occurring ν_j . The approximation in (2.62) is equivalent to setting $f_j = f_0$, which can be generalized to simplify the calculation of the overall Doppler shift.

Using the overall Doppler shift ν_l of each multipath component, the delay-Doppler-spread function [Bel63, Fle90], or Doppler-resolved lowpass impulse response [Kat97], is given by

$$\underline{s}^{LP}(\tau, \nu) = \sum_{l=1}^n \underline{a}_l e^{-j2\pi f_0 \tau_l} \delta(\tau - \tau_l) \delta(\nu - \nu_l), \quad (2.63)$$

from which all other general system functions can be obtained via Fourier transforms. The time-variant lowpass impulse response¹¹, which is the generalized form of (2.59), is e.g. obtained by the inverse Fourier transform of (2.63) with respect to the Fourier relation ($\nu \bullet \circ t$).

2.4.3.3 Delay spread

In order to characterize the frequency-selective behaviour of a transmission channel, the integral parameter delay spread σ_τ plays an important role. It is a

¹¹ Also called input delay-spread function [Bel63]

measure of the broadening of a transmitted impulse due to the time-dispersive influence of the channel. Mathematically it is equivalent to the definition of the “standard deviation” of the power delay profile (PDP) of a channel and is therefore related to its width. The PDP, generally obtained by ensemble averaging, is proportional to the square of the absolute value of the lowpass impulse response (2.59) [Ste92, GW98]. The square root of the second central moment of the PDP, which is the delay spread, can thus directly be calculated from the output of the ray tracing as

$$\sigma_\tau = \sqrt{\frac{\sum_{l=1}^n \tau_l^2 T_l^2}{\sum_{l=1}^n T_l^2} - \left(\frac{\sum_{l=1}^n \tau_l T_l^2}{\sum_{l=1}^n T_l^2} \right)^2}. \quad (2.64)$$

The right part in the radical is the squared mean delay. A non time-dispersive channel has a delay spread equal to zero. The larger σ_τ , the stronger is the frequency-selective behaviour of the channel.

2.4.3.4 Doppler spread

Following the same approach as for the delay spread in the delay domain, the time-variant behaviour of a channel can be integrally characterized by the Doppler spread in the Doppler domain. The Doppler spread σ_ν is a measure of the broadening of the theoretically infinitely narrow spectral line of a harmonic excitation due to the frequency-dispersive influence of the channel. Mathematically it is equivalent to the definition of twice the “standard deviation” of the Doppler spectrum. The Doppler spectrum is proportional to the square of the absolute value of the delay-Doppler-spread function (2.63) integrated over τ [Ste92, GW98]. Thus, according to the case of the delay spread, σ_ν can directly be calculated from the output of the ray tracing as

$$\sigma_\nu = 2 \sqrt{\frac{\sum_{l=1}^n \nu_l^2 T_l^2}{\sum_{l=1}^n T_l^2} - \left(\frac{\sum_{l=1}^n \nu_l T_l^2}{\sum_{l=1}^n T_l^2} \right)^2}. \quad (2.65)$$

Again, the right part in the radical is the squared mean Doppler. A non frequency-dispersive channel would have a Doppler spread equal to zero. The larger σ_ν , the stronger is the time-variant behaviour of the channel.

2.5 Summary

In this chapter, a ray-optical modelling approach was explained together with the underlying assumptions. The necessary formulations of the most important wave propagation phenomena in the environment of a curved tunnel were

presented. In particular, a new method to include stochastic rough surface scattering into deterministic ray-optical propagation modelling was derived. Finally, multipath propagation was treated, and the radio propagation channel functions and parameters were stated in the context of the ray-optical modelling results.

The central—because computationally expensive—issue of ray-optical propagation modelling in an arbitrarily shaped tunnel is to determine the ray trajectories from the transmitter to the receiver. This problem is dealt with and solved in the following chapter.

Chapter 3

Ray tracing in a tunnel environment

In the previous chapter, the formulation and methods of ray-optical wave propagation modelling have been presented. However, one major point has not yet been considered but implicitly assumed, namely, that the ray trajectories from the transmitter to the receiver are known. This chapter now deals with the question of *how* these trajectories are determined in the curved geometry of a tunnel environment. In this context, the concept of ray tracing becomes indispensable. The term ray tracing includes two different aspects: firstly, the determination of a ray trajectory from the transmitter to the receiver; secondly, once this trajectory is available, the determination of the actual field strength of the ray at the receiver by “tracing” (i.e. following) the ray along its trajectory, taking into account all occurring propagation phenomena. The latter was treated in the previous chapter, the former is treated in this one. A sharp distinction between the above two aspects is not always possible. Instead, often they are performed in parallel during the process of ray tracing.

The principle methods of ray tracing are first examined (cf. section 3.1). In section 3.2, the shortcomings of existing ray-tracing techniques arising in curved geometries are identified. In the same section, a general solution to the problem is derived in connection with ray launching. Section 3.3 shows how the proposed technique is applied to ray tracing and the different types of analysis (i.e. coherent or incoherent analysis). This is followed by an approximate solution for the power flux through a tunnel in section 3.4.

3.1 Methods of ray tracing

The retrieval of valid ray trajectories from the transmitter to the receiver in a given geometry via ray tracing can be distinguished in direct and indirect methods. Direct methods, like image theory or the “rubber band method¹”, directly lead to the exact ray paths. For indirect methods, also called ray launching, a number of rays is launched (i.e. send out) from the transmitter in arbitrary directions and traced until they eventually hit the receiver or until they surpass a certain maximum attenuation. The approaches which are relevant to ray tracing in tunnel environments are discussed in the following.

3.1.1 Direct approach: image theory

Obviously, it is most desirable to determine all ray trajectories exactly. This is possible by means of image theory, but unfortunately only in planar geometries. The principle of image theory is depicted in Fig. 3.1. The transmitter

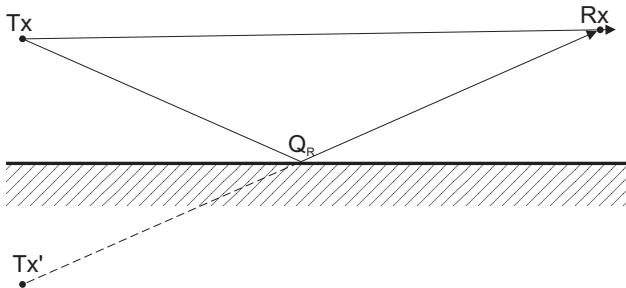


Figure 3.1: The concept of image theory

Tx (or receiver Rx) location is mirrored at the plane of interaction, leading to an image transmitter Tx' (or image receiver Rx'). The straight line from the image transmitter to the receiver (or from the transmitter to the image receiver) intersects the plane of interaction in the reflection point, which clearly defines the ray trajectory for this single reflection. For multiple reflections, the process of imaging is repeated accordingly. At curved boundaries, however, the concept of images becomes ambiguous, because the image of the transmitter (or receiver) is a continuous image line, instead of a discrete point. Image theory is therefore only applicable to straight tunnels with rectangular or piecewise/partially planar cross sections. In such planar geometries it delivers the most accurate ray-tracing results [Rem93, Kle93, MLD94], thus it is taken as

¹The “rubber band method” is used to determine diffraction wedges and paths in a 2D vertical plane for rural or urban wave propagation modelling [Leb91, Cic94]

reference solution in the theoretical validation of section 5.1. The limitation to (piecewise) planar geometries implies that realistic tunnels can only be dealt with by image theory in a highly approximate manner. Usually the real cross section is approximated by an equiarea rectangle [YA⁺85, ZH98a], or the whole tunnel is tessellated into multiple planar facets [CJ96a, HCC98, TV⁺99].

It is worth noticing that if a straight tunnel with rectangular cross section is considered, a direct relation between mode theory and the GO imaging approach can be established [MW74a, Del82].

3.1.2 Indirect approach: ray launching

In contrast to image theory, where the retrieval of the exact ray trajectory precedes the actual propagation modelling, ray launching follows a completely different approach. In ray launching, also referred to as the shooting and bouncing ray (SBR) method [LCL89], a large number of rays is sent out from the transmitter in arbitrary/specific directions. The initial phasors of the rays are determined by the radiation pattern of the transmitting antenna including phase and polarization. Each ray is traced in space and wave propagation is calculated according to geometrical optics, including reflection, scattering etc. The trace terminates if a ray eventually hits a receiver, or when it surpasses a certain maximum attenuation. At the receiver, all incoming rays are combined in order to determine the overall reception level. Generally, only a few of the launched rays, of which the trajectories have been searched for, actually hit the receiver. Therefore ray launching is referred to as an indirect ray-tracing approach. To ensure that all relevant propagation paths are found in the process of ray launching, a sufficiently large number of rays has to be sent out at the transmitter. The major advantage of ray launching is its applicability even in curved geometries. However, the decision, whether a ray hits a receiver or not, is actually one of the most severe problems in ray launching. The two known methods to solve this problem—at least in planar geometry—are discrete ray tubes [CZL95, SM97] or reception spheres [HB⁺92, SR94].

3.1.2.1 Discrete ray tubes

Discrete ray tubes of finite width may be seen as a discretization/magnification of the differential tube of rays in GO (cf. Fig. 2.2). They consist of typically three to four limiting rays (or lines) circumscribing the actual ray, which itself is often named reference or central ray (cf. Fig. 3.2). Discrete ray tubes have the purpose to delimit the different reference rays to each other, all of which represent locally plane wavefronts. Therefore, the limiting rays belong to (different) adjacent discrete ray tubes at the same time, in order to make this delimitation unambiguous. The decision, whether a receiver is reached by

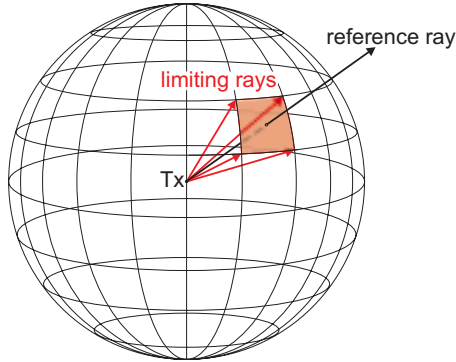


Figure 3.2: Discrete ray tube and corresponding reference ray

a ray² or not, becomes quite simple: it is sufficient to determine, if the receiver lies in the respective discrete ray tube. Figure 3.3 shows the same 2D scenario as Fig. 3.1 but with discrete ray tubes. It illustrates the approximate nature of ray launching: the reference rays of the direct and the reflected ray tubes are similar but almost never equal to the exact rays given by image theory.

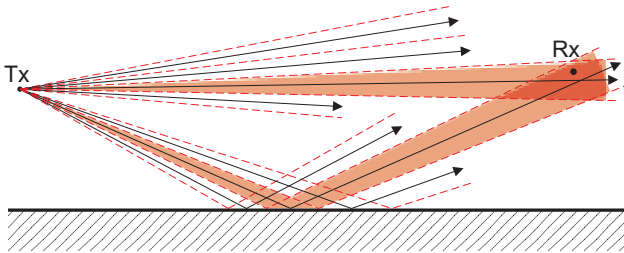


Figure 3.3: Ray launching with discrete ray tubes

Ray launching with discrete ray tubes proves to be a suitable means to predict wave propagation in indoor environments, which are constituted by planar surfaces [Zwi94, Cic94, GW⁺95, COST231]. The disadvantage of discrete ray tubes is their failure at curved boundaries, which will be addressed in section 3.2.

²I.e. a geometrical optical ray or reference ray.

3.1.2.2 Reception spheres

Another tool widely used in ray launching is the reception sphere concept [HB⁺92, SR94]. The receivers are assigned to a certain volume in space, typically a sphere, yielding the termination reception sphere. A launched ray reaches a receiver, if it intersects the corresponding reception sphere. The difficulty with the classical approach of reception spheres is the determination of their size. If the size is too small, only a few rays reach the receiver and the results are inaccurate, since important propagation paths may not be considered. On the other hand, if the size is too large, several physically “identical rays” reach the receiver so that the results become faulty without a correct normalization. This *multiple ray problem* is illustrated in Fig. 3.4, where receiver Rx₁ is reached by multiple direct rays, each representing a distinct wavefront. In reality, however, there is only one physical wavefront reaching the receiver on the direct propagation path and thus only one direct ray. The multiple rays can also be classified as being too close to be considered as independent [Des72]. Additionally, Fig. 3.4 shows that the number of registered rays also

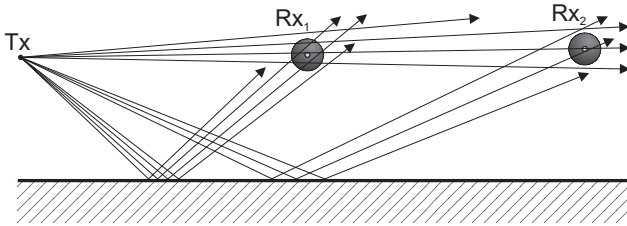


Figure 3.4: The multiple ray problem using reception spheres with constant size in ray launching

depends on the distance from the transmitter, assuming a constant size of the reception spheres. An approximate solution to overcome those problems in planar geometries are adaptive reception spheres. If the rays are launched with an uniform angular separation γ at the transmitter, the spacing between two adjacent rays is proportional³ to γ and the unfolded path length r . If the distance of the receiver to a ray is smaller than half of the ray spacing, the ray is assumed to contribute to the received signal. For small γ , the tested ray will be a good approximation of the ray passing directly through the center of the receiver [HB⁺92]. An almost identical angular separation between a ray and its nearest neighbours can be achieved, if e.g. the spherical surface of the source is subdivided by a geodesic polyhedron with tessellated trian-

³The ray spacing is given by $2 \tan(\frac{\gamma}{2})r \approx 2\frac{\gamma}{2}r$ for small γ .

gular faces, resulting in hexagonal shaped wavefront portions⁴ [SR94]. The wavefronts can be further approximated by circumscribed circles around the hexagons to make sure that no reception points are missed. Thus the radius of the reception spheres becomes

$$r_R = \frac{\gamma r}{\sqrt{3}}, \quad (3.1)$$

which is of course different for each ray path. Due to the small overlap of the

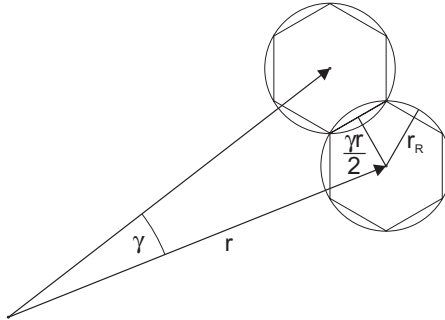


Figure 3.5: Hexagonal shaped ray tubes with circumscribed, slightly overlapping reception spheres, still leading to multiple received rays (cf. [SR94])

reception spheres (c.f. Fig. 3.5), there may be still some multiple received rays. To eliminate them, all received rays have to be stored and compared pairwise. This process is called identification of multiple rays.

3.1.2.3 Identification of multiple rays

The task of identifying multiple rays, which seems obvious for the human being, cannot be performed exactly on the computer, but has to be done according to several conditions. One possibility is to test the following three criteria consecutively:

1. Number of reflections: obviously if the number of reflections is different for two rays, they cannot be the same.
2. Delay time: if the number of reflections are equal, the delay time of the two rays are compared. They are considered to have “equal” delay times, if both fall into the same delay interval.

⁴Actually, resulting in pentagonal and hexagonal wavefronts on the surface of the polyhedron.

3. Angle of transmission: only if both preceding criteria are satisfied, the angles of transmission of both rays under test are compared. Finally, if both are launched into the same direction, specified by a solid angle interval, the rays are considered to be equal.

Although the first point is unambiguous, the following two require the specification of a certain test range. The delay interval is less critical and mainly depends on the accuracy of the computer arithmetic. The solid angle interval, however, also depends on the angular separation of the rays at the transmitter and has to be chosen to be significantly larger than $\frac{\sqrt{3}r_B}{r}$, which follows from (3.1).

The identification of multiple rays (IMR), which has been originally used in conjunction with adaptive reception spheres in planar geometries, can be utilized as an independent method even in curved geometries. It delivers reasonable results with the exception of the areas near and in caustics [SW98]. However, the approach is only feasible for a small number of receiver locations, due to the fact that all incoming rays have to be stored and post-processed, which requires large storage capacity and excessive simulation times.

3.2 Ray launching in curved geometry

3.2.1 Ray tubes: approximate solution for 2D-curvature

The advantage of discrete ray tubes is the unique assignment of rays to the receiver. The test, whether a receiver “falls” into a ray tube, becomes quite efficient, if adjacent limiting rays lie in a plane. In this case, fast geometrical algorithms [Zwi94, Gla95] can be used, which determine on which side of the plane the receiver is located. For point sources and planar boundaries, the premise of limiting planes is always fulfilled.

The situation changes, if curved boundaries are to be considered. The two obvious methods to proceed with the reflection of a discrete ray tube at a curved surface are either to reflect the whole tube at the tangential plane in the intersection point of the central ray and the surface, or to reflect each limiting ray and the central one at the tangential plane of its own intersection point with the surface. If the joint tangential plane approach is chosen, the initial intention of the discrete ray tubes, which is the unique delimitation of the different central rays, is invalidated. For convex surfaces, this approach leads to dispersed—formerly adjacent—ray tubes, leaving the space between them uncovered. For concave surfaces, adjacent ray tubes overlap and become ambiguous. If the separate reflection plane approach is chosen, the resulting tubes can no longer be interpreted as a discretization of the differential GO tube of rays. In fact, the central ray may even leave the limiting tube. But

the most important drawback is the arbitrary shape of the reflected ray tube: adjacent limiting rays generally do not lie in the same plane, which inevitably leads to a more complicated and therefore time-consuming receiver test⁵.

An approximate solution for two-dimensional (2D) curvature can be found by forcing the reflected limiting rays such that the rays pairwise form a limiting plane [Laq94, CZW96]. For straight tunnels with an elliptical cross section, first the projection of the propagation paths into the plane of the cross section is considered. The strategy is to reflect the limiting rays at the arc of the ellipse, each of them in its own point of reflection. Then the reflected central ray is chosen to pass through the intersection point of the limiting rays. The divergence in the other dimension, which is along the tunnel axis, is kept to be spherical such that finally ray tubes with limiting planes are achieved.

Although this approximation seems reasonable, it produces unsatisfactory results by introducing artificial caustics [Laq94, CZW96, SW98]. An approach, which is not restricted to 2D curvature, and which does not suffer from the above mentioned limitations, is presented in the following section.

3.2.2 Reception spheres: the concept of ray density normalization (RDN)

If reception spheres are used, a normalization can be found, being also valid in curved geometries—contrary to the hitherto usual approach (cf. section 3.1.2.2). The new concept of ray density normalization (RDN) is as follows. Instead of trying to avoid the existence of multiple rays, it is *a priori* assumed that several multiple (or dependent) rays are present on each physical propagation path. The number of these rays is determined, and this number is used to normalize the contribution of each ray to the total field. As a consequence, the new method requires multiple representatives of each physical electromagnetic wave at a time. This is opposed to classical ray tracing, where the one ray representing a locally plane wave front is searched.

3.2.2.1 Determination of the number of multiple rays

In order to determine the number of rays, which reach the receiver on the same propagation path, the ray density is used. The ray density is defined as the number of rays per unit area. In addition to its amplitude, phase, polarization etc., each ray carries the ray density along its path. If a ray hits a reception sphere, the theoretical number of multiple rays hitting the same sphere can be calculated by simply multiplying the ray density with the area of the sphere.

⁵For the general case, this test can only be performed on a numerical basis.

For a number of N launched, equally distributed, discrete rays in space and the restriction to plane surfaces, the ray density n_d at a distance⁶ r from the transmitter is given by

$$n_d = \frac{N}{4\pi r^2}. \quad (3.2)$$

If reflections at curved surfaces are considered, the proportionality of n_d to $1/r^2$ is not longer valid in general. At curved surfaces the rays can be focused or defocused. It is e.g. possible that after a reflection at a parabolic reflector the rays are parallel, i.e. n_d becomes independent of r (plane wave). The determination of the ray density n_d in curved geometries is performed according to geometrical optics in analogy to the calculation of the electric field after reflection from a curved surface. However, the ray density n_d is not proportional to the electric field $\underline{\vec{E}}$ but to the radiation density S of a ray. Since $S \propto |\underline{\vec{E}}|^2$, the ray density n_d at a distance s from a curved surface can be written as

$$n_d^r(s) = \left| \frac{\rho_1^r \rho_2^r}{(\rho_1^r + s)(\rho_2^r + s)} \right| n_d^i, \quad (3.3)$$

where n_d^i denotes the incident ray density just before the reflection, $n_d^r(s)$ is the ray density after reflection at a distance s from the point of reflection, and $\rho_{1,2}^r$ denote the radii of curvature of the wave front after reflection at $s = 0$, which is represented by the reflected ray (cf. chapter 2). The ray density $n_{d,1}^i$ before the first reflection at a curved surface is given by (3.2). Using (3.2) and (3.3) it is possible to determine the ray density of all rays along their propagation path.

The special case of an initially stigmatic ray ($\rho_1 = \rho_2 = r$) reflecting exclusively on planar surfaces leads back to (3.2) according to

$$n_{d,m}^r(s_m) = \left| \frac{r_m^2}{(r_m + s_m)^2} \right| n_{d,m}^i = \left| \frac{r_m^2}{(r_m + s_m)^2} \right| \cdots \left| \frac{r_1^2}{(r_1 + s_1)^2} \right| \frac{N}{4\pi r_1^2} = \frac{N}{4\pi r^2}, \quad (3.4)$$

with $r_{j+1} = r_j + s_j$, $n_{d,j+1}^i = n_{d,j}^r(s_j)$, $j = 1, \dots, m-1$; m is the number of reflections and $r = r_m + s_m$.

If a ray hits the receiver, the theoretical total number M of rays reaching the receiver on the same propagation path is now calculated using the “visible” area A of the receiver normal to the propagation direction of the ray, i.e.,

$$M = n_d A. \quad (3.5)$$

⁶I.e. the unfolded path length.

Again, these *multiple rays* are physically identical, i.e. they arrive from the same direction, they have the same delay, number of reflections etc. Hence, these rays have to be weighted, such that the ensemble of M multiple rays leads to the same result as if only (exactly) one ray would reach the receiver. The weighting thereby depends on the type of analysis, described in section 3.3. The determination of A depends on the type of receiver, treated in section 4.5. For a reception sphere, the area equals $A = \pi r_R^2$, where r_R denotes the radius of the sphere.

3.2.2.2 Prerequisites of the RDN

Prerequisites of the RDN are a large number of rays and their homogeneous distribution in space. The large number requirement results from the discretization in the computer: the theoretical number of multiple rays M given by (3.5) is a real valued number. However, the number of actual registered rays is an integer. Consequently, in order to keep the error introduced by the weighting as small as possible, the number of multiple rays has to be sufficiently large. The second requirement directly results from (3.5): the relation is only valid for a homogeneous distribution of the rays. This distribution can be achieved by a stochastic generation of the ray directions (Monte-Carlo method, cf. section 4.2). In order to fulfil the first requirement with tolerable computational complexity, all ray-tracing calculations, especially all intersection routines, should be solvable analytically (cf. section 4.1).

3.3 Application of the ray density normalization

In the remainder of this section, only the ratios of received values (index R) to a reference value (index 0) are examined, whereby absolute values become obsolete. Directly at the transmitter ($r = 0\text{m}$) the ratio cannot be determined, since the electric field—and consequently the received power—theoretically become infinite (cf. section 2.2). Without loss of generality, suppose that a reference distance $r_0 = 1\text{m}$ is assumed, i.e.,

$$\frac{P_R(r_0 = 1\text{m})}{P_0} = \frac{V_R(r_0 = 1\text{m})}{V_0} = 1, \quad (3.6)$$

where the notation $V = |\underline{V}|$ is used for the magnitude of the induced voltage at the receiver.

3.3.1 Relationship between divergence of a ray and ray density

As shown in section 2.4, the loss along a propagation path due to reflection, absorption etc. can be represented by the propagation transfer factor T_P , which also includes the influence of the antennas directivities. The attenuation due to the divergence of the tube of rays can be represented by the divergence transfer factor T_D . For exclusively planar boundaries, the divergence factor is given by $T_D = T_{D,0} = 1m/r$, where r denotes the unfolded path length. However, at curved boundaries, the radii of curvature of the astigmatic tube of rays have to be considered, leading to

$$T_D = \sqrt{\left| \frac{\rho_{1,m}^r \rho_{2,m}^r}{(\rho_{1,m}^r + s_m)(\rho_{2,m}^r + s_m)} \right| \cdots \left| \frac{\rho_{1,1}^r \rho_{2,1}^r}{(\rho_{1,1}^r + s_1)(\rho_{2,1}^r + s_1)} \right| \frac{1m^2}{r_1^2}}, \quad (3.7)$$

with m representing the number of reflections, $\rho_{1/2,j}$ the radii of curvature after the j -th reflection, s_j the distance from reflection point j to the next one, and r_1 the distance from the transmitter to the first point of reflection. T_D can also be expressed in terms of n_d by taking the ray density of the ideal isotropic source (3.2) as start density and by cascading (3.3) accordingly. By comparison to (3.7) the following relation can be established

$$T_D = \sqrt{\frac{4\pi}{N} n_d 1m^2}. \quad (3.8)$$

Now it is possible to state the normalized induced voltage at the receiver for a single physical propagation path or ray in dependence of the ray density

$$\frac{V_R}{V_0} = T_P T_D = T_P \sqrt{\frac{4\pi}{N} n_d 1m^2}. \quad (3.9)$$

The relative received power results from the square of (3.9), i.e.,

$$\frac{P_R}{P_0} = \left(\frac{V_R}{V_0} \right)^2 = T_P^2 \frac{4\pi}{N} n_d 1m^2. \quad (3.10)$$

In the following sections is shown how the ray density normalization is applied to two different calculation schemes: the so-called field and power traces.

3.3.2 Field trace

The classical approach in ray launching/tracing is to assign a certain electric field strength to each ray, which is normalized to a reference level, as indicated

in chapter 2. The rays are traced until they eventually hit a receiver, or until they surpass a certain maximum attenuation. This approach is referred to as *field trace*.

In order to correctly weight the contribution of each ray to the overall received power or the induced voltage at the receiver, weighting factors $X_F^{c/i}$ are introduced. This is because the number of rays reaching the receiver on the same physical propagation path is *a priori* unknown (cf. section 3.2.2). Furthermore, one has to differentiate if the analysis of multipath propagation is of coherent or incoherent nature. For the coherent analysis, the weighting takes the form

$$V_R^c = V_R X_F^c, \quad (3.11)$$

for the incoherent analysis, the weighting becomes

$$V_R^i = V_R X_F^i. \quad (3.12)$$

The following considerations are only valid for a single physical propagation path, on which several discrete rays with identical amplitude \underline{V}_R reach the receiver. The number of multiple rays is theoretically given by M . The coherent summation of all rays belonging to the same propagation path leads to

$$\frac{P_R^c}{P_0} = \left| \sum_{k=1}^M \frac{V_{R,k}^c}{V_0} \right|^2 = \left(M \frac{V_R^c}{V_0} \right)^2 = M^2 T_P^2 \frac{4\pi}{N} n_d 1 \text{m}^2 X_F^{c,2}, \quad (3.13)$$

which has to match the result of (3.10), yielding

$$X_F^c = \frac{1}{M} = \frac{1}{n_d A}. \quad (3.14)$$

The incoherent summation leads to

$$\frac{P_R^i}{P_0} = \sum_{k=1}^M \left| \frac{V_{R,k}^i}{V_0} \right|^2 = M \left(\frac{V_R^i}{V_0} \right)^2 = M T_P^2 \frac{4\pi}{N} n_d 1 \text{m}^2 X_F^{i,2}. \quad (3.15)$$

Comparing the result to (3.10) gives

$$X_F^i = \frac{1}{\sqrt{M}} = \frac{1}{\sqrt{n_d A}} = X_F^c \sqrt{n_d A}. \quad (3.16)$$

With (3.14) and (3.16) the RDN-based weighting factors are known, by which the predicted values of the discrete rays have to be normalized at the receiver in order to obtain valid results.

3.3.3 Power trace

The idea of the *power trace* is to look at the power (respectively energy) of each ray, instead of the habitual electric field. This method is the standard approach in ray tracing for computer graphics [Gla89]. The total radiated power of the transmitter is spread over all rays. Each ray “keeps” its portion of the power on its way through the tunnel, attenuation may occur due to propagation phenomena like reflection etc. If a ray hits a receiver, it is assumed that its remaining power is transferred totally to the receiver. The summation over all received rays gives the received total power. Focusing effects for instance may occur, if a huge number of rays hit the receiver. On the other hand, the effect of free-space attenuation is included implicitly: at increased distance, less rays and thus less power reach the receiver due to geometrical divergence (cf. Fig. 3.6). In contrast to the field trace, where each ray represents a locally plane wave and therefore can be treated separately, only the ensemble of all rays reaching the receiver makes sense in physical terms for the power trace.

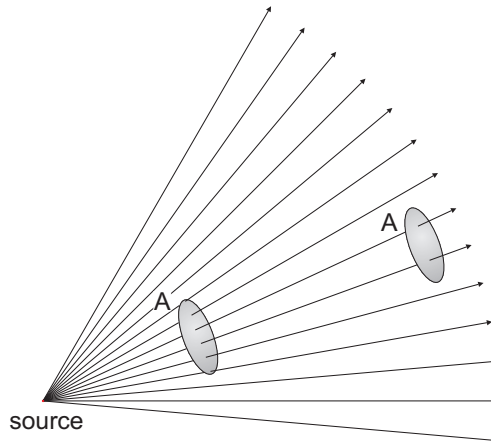


Figure 3.6: Geometrical divergence of the power trace approach: at increased distance less rays reach the area A

The initial power P_t of each ray is determined by the input power P_T , the transmitting antenna characterized by G_T and \vec{C}_T , and the number of launched rays N , yielding

$$P_t = \frac{P_T G_T |\vec{C}_T|^2}{N}. \quad (3.17)$$

If no propagation losses occur, the assumption that a ray delivers its total

energy to the receiver can be expressed by

$$S_A = \frac{P_t}{A}. \quad (3.18)$$

Here A denotes the area of the receiver and S_A the radiation density, which the ray tube (corresponding to the discrete ray) would have, if its area equalled A . The approximation is valid for

$$A_{rt} \leq A \approx A_{eR}, \quad (3.19)$$

where A_{rt} denotes the actual area of the ray tube and A_{eR} the effective area of the receiving antenna given by (2.47). The contribution of the ray to the total received power is obtained using A_{eR} , leading to

$$P_R = S_A A_{eR} = \frac{P_t}{A} A_{eR} = \frac{\lambda_0^2}{4\pi AN} P_T G_T G_R T_P^2. \quad (3.20)$$

To overcome the loss-free requirement of (3.18), the propagation transfer factor T_P is necessary in the previous equation to account for the dissipation of energy⁷ on the propagation path due to the different propagation phenomena. However, no divergence factor is introduced since the power of the ray is regarded, not its radiation density. Equation (3.20) points out that only the ensemble of all received rays has a physical meaning. This can easily be verified for the free-space case with $T_P = 1$. The area of the receiver A at a distance r to the source is reached by

$$M = \frac{AN}{4\pi r^2} \quad (3.21)$$

rays, assuming N rays equally distributed over the solid angle 4π (cf. Fig. 3.6). This results in a total received power of

$$P_{R,tot} = \sum_{k=1}^M P_{R,k} = M P_R = \left(\frac{\lambda_0}{4\pi r}\right)^2 P_T G_T G_R, \quad (3.22)$$

which equals (2.51) for $T_D = T_{D,0} = 1\text{m}/r$.

For the general case—including reflection etc.—the same approach as in the previous section is adopted. First, the power of each single ray is normalized leading to

$$\frac{P_R}{P_0} = T_P^2, \quad (3.23)$$

⁷ T_P also includes the influence of the antenna directivities (cf. (2.52b)).

or equivalently

$$\frac{V_R}{V_0} = T_P. \quad (3.24)$$

The phase of the induced voltage at the receiver is determined by the traversed path length and phase jumps of $+90^\circ$ at potential passages through caustics [Bal89, LCL89]. However, (3.24) only states the contribution of a single ray. Again, the number of rays arriving at the receiver on the same physical propagation path is *a priori* unknown. Therefore, according to the field trace case, weighting factors are introduced which are based on the RDN. Finally, the actual value at the receiver is achieved by weighting and superposition of all incoming rays. In analogy to section 3.3.2, the coherent summation is in the form

$$\frac{P_R^c}{P_0} = \left| \sum_{k=1}^M \frac{V_{R,k}^c}{V_0} \right|^2 = \left(M \frac{V_R^c}{V_0} \right)^2 = M^2 T_P^2 X_P^c{}^2, \quad (3.25)$$

yielding

$$X_P^c = \sqrt{\frac{4\pi n_d 1m^2}{N M^2}} = \sqrt{\frac{4\pi 1m^2}{N n_d A^2}} = \sqrt{\frac{4\pi 1m^2}{NA} \frac{1}{M}} \quad (3.26)$$

after comparison with (3.10). The power sum, on the other hand, is given by

$$\frac{P_R^i}{P_0} = \sum_{k=1}^M \left| \frac{V_{R,k}^i}{V_0} \right|^2 = M \left(\frac{V_R^i}{V_0} \right)^2 = M T_P^2 X_P^i{}^2, \quad (3.27)$$

leading to

$$X_P^i = \sqrt{\frac{4\pi 1m^2}{NA}} = X_P^c \sqrt{n_d A}. \quad (3.28)$$

For both the field and the power trace, the following relation holds

$$X^i = X^c \sqrt{n_d A}, \quad (3.29)$$

i.e. (3.29) is independent of the approach.

Because of the introduced factors, the actual computation of the coherent results is essentially the same for both the field and the power trace⁸. Only the

⁸One difference lies in the determination of the phase jumps when crossing caustics. The change in phase is performed implicitly by (2.13) for the field trace case. For the power trace, passages through caustics have to be determined by additional tests.

way how these methods are derived differs: the conventional straight forward analytical formalism for the field trace and the more graphical approach for the power trace. The difference between the two methods, however, becomes significant for the incoherent analysis. The incoherent weighting factor X_P^I of the power trace is constant according to (3.28) and therefore independent of the ray density. This means, the complicated and time-consuming calculation of the ray density can be omitted, speeding up the simulation considerably, if only the power sum is of interest in the analysis. A method, making solely use of the incoherent analysis, is treated in detail in the next section.

Furthermore, the power trace in combination with the RDN allows to overcome one of the major disadvantages of geometrical optics: its failure at caustics. Section 2.2 has shown that in a caustic the predicted GO field—and therefore the received power—approach infinity. For the power trace approach, however, the received power is determined by the number of rays, which actually reach the receiver. This number is always finite and smaller than the number of launched rays N . Consequently, even if all rays reached the receiver, the maximum received power would always be lower⁹ than the input power of the transmitting antenna P_T in the incoherent analysis. The only variable, which reflects the GO behaviour, is the ray density n_d needed for the weighting of the coherent analysis. In (3.26), the ray density n_d is used together with the visible area of the receiver A to determine the theoretical number of multiple received rays $M = n_d A$. In a caustic, this value would approach infinity. Heuristically, it can now be bound by the maximum value of N , or by a fraction of it.

3.4 The method of power flow

A fast way to integrally characterize the propagation through a tunnel is given by the method of *power flow*. For this method, the total time-averaged forward propagating power P_{prop} through the tunnel cross section is computed at different locations in a tunnel [LL98]. Mathematically P_{prop} is given by the surface integral

$$P_{prop} = \int S_n dA, \quad (3.30)$$

where S_n denotes the radiation density (or time-averaged Poynting vector component) normal to the cross section. In ray tracing this can be achieved

⁹Or equal to P_T , if no losses at the reflecting surfaces occur.

by the power sum of all impinging rays on the tunnel's cross section

$$P_{prop} = \sum_q P_{R,q}, \quad (3.31)$$

where $P_{R,q}$ are the (remaining) powers of each discrete ray according to the power-trace approach. Furthermore, if an equal distribution of the power over the whole cross section is assumed, the radiation density is given by

$$\tilde{S} = \frac{P_{prop}}{A_{cs}}, \quad (3.32)$$

where A_{cs} denotes the total area of the cross section. Using the effective area $A_{ei} = \frac{\lambda_0^2}{4\pi}$ of an isotropic antenna, an approximation of the total received incoherent power can be obtained by

$$\tilde{P}_{R,tot}^i = \tilde{S}A_{ei} = P_{prop} \frac{A_{ei}}{A_{cs}} = \frac{\lambda_0^2}{4\pi} \frac{P_T G_T}{N A_{cs}} \sum_q T_{P,q}^2. \quad (3.33)$$

This result can now be compared with the received incoherent power of section 3.3.2. Summing over all incoming rays at the receiver and substituting (3.16) into (3.15) yields

$$\frac{P_{R,tot}^i}{P_0} = \sum_l M_l T_{P,l}^2 \frac{4\pi 1\text{m}^2}{N A_l} = \frac{4\pi 1\text{m}^2}{N} \sum_{q'} \frac{T_{P,q'}^2}{A_{q'}}. \quad (3.34)$$

With $G_R = 1$ for the isotropic antenna, the reference power P_0 is given by

$$P_0 = \left(\frac{\lambda_0}{4\pi 1\text{m}} \right)^2 G_T P_T, \quad (3.35)$$

such that

$$P_{R,tot}^i = \frac{\lambda_0^2}{4\pi} \frac{P_T G_T}{N} \sum_{q'} \frac{T_{P,q'}^2}{A_{q'}}. \quad (3.36)$$

In comparison to the previous equation, (3.33) reveals its ability to approximate the actual received power: the important difference lies in the considered area. In (3.36), the actual visible area $A_{q'}$ of the receiver is taken for each ray (cf. section 4.5), resulting in a certain number of discrete rays (index q'), which actually hit the receiver or reception sphere. Conversely on the other hand in (3.33), the total cross section A_{cs} is taken, where *all* remaining rays (index q), i.e. all rays that reach the cross-sectional area, are used for the

analysis. The approximation of (3.33) is thus not applicable in the vicinity of the source, where the main assumption, namely an equal distribution of power over the cross section, is rarely fulfilled. Nevertheless, the simulation becomes very fast for this incoherent analysis, since the calculation of the ray density is not required, and since only a significant smaller number of rays is needed than for the coherent analysis [LL98, CG99]. Therefore, the method of power flow can be used as a first and fast estimate of the mean received power and thus of the propagation behaviour in a tunnel.

3.5 Summary

In this chapter, the question of “how” the ray trajectories are determined in a tunnel has been answered. The terms ray tracing and ray launching were introduced and explained. The different existing techniques, which are *not* able to cope with curved boundaries, were illuminated. In order to solve the problem of ray tracing in curved geometries, a novel ray-launching/ray-tracing technique was developed, termed ray density normalization (RDN). Additionally, this method leads to finite results in caustics, which is not the case in conventional GO. Finally, a very fast approximate way to characterize the propagation behaviour in a tunnel, the method of power flow, together with its relation to the correct solution was established.

The application of the theoretical considerations presented and the integration into a functional simulation tool require an adequate representation of a tunnel in the computer. Therefore, the handling of the geometry of a tunnel is presented in the following chapter, together with other features of the simulation approach.

Chapter 4

The simulation approach

In the previous chapters, techniques to treat electromagnetic wave propagation in a ray-optical way have been developed theoretically. To simulate wave propagation in arbitrarily shaped tunnels by applying these methods, a precise modelling of the tunnel itself is needed. The present chapter deals with the models for the geometry of a tunnel. Additional aspects of the implementation, which are inherent to the special geometry of tunnels and to the requirements of tunnel communication systems, are also presented.

The first section 4.1 deals with geometries commonly used for tunnels and their modelling with the computer. This is followed by the concept of stochastic ray launching in section 4.2, which is mandatory for the RDN of chapter 3. Furthermore, an approach to allow for transmitter placement outside the tunnel is explained (cf. section 4.3). The inclusion of moving obstacles, like vehicles, is treated in section 4.4. Finally, the different types of analysis are presented (cf. section 4.5), followed by general remarks on the simulation approach in section 4.6.

4.1 Geometry

Almost all train or street tunnels are either of rectangular or arched shape [BL74, Kin90, Mar93, Str96]. The tunnel course consists of combinations of straight and curved sections. Normally the curves have a constant radius of curvature for security reasons. The geometry of the transition from a straight section to a curve with constant radius of curvature is depicted in Fig. 4.1. In roadmaking and tunnelling, the smooth transition from the theoretically infinite radius of curvature of the straight section to a curve with radius r_c is generally performed by a section of a clothoid of length s [Str96, Str95, Mar86].

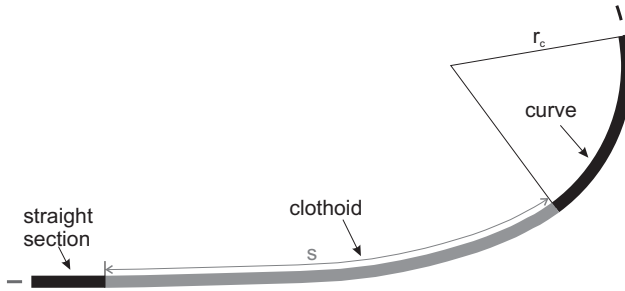


Figure 4.1: Transition of straight section to curved section via intermediate clothoid

To determine the ray trajectories, the reflection points of a ray on the tunnels boundaries have to be known. They are found by intersecting the ray with the respective boundary in three-dimensional space. As already indicated in section 3.2.2, all ray-tracing calculations, especially the intersection routines, have to be solvable analytically in order to allow for tracing the required large number of rays in reasonable computation time. Therefore, the tunnel geometry must be described by only a few geometrical (3D) primitives, staying as close as possible to reality.

In the simulation approach, the cross section of a tunnel can be either rectangular or elliptical with a raised floor representing the road or rail level. Furthermore, an additional ceiling may be inserted in the elliptical tunnel, which is often the case for arched tunnels of newer kind with ventilation.

4.1.1 Straight sections

For straight rectangular tunnel sections, four planes (rectangles) are needed to describe the geometry (cf. Fig. 4.2(a)). For straight elliptical tunnel sections, one elliptical cylinder and one or two planes (rectangles), representing the floor and an optional ceiling, are sufficient to describe the geometry of the tunnel, as indicated in Fig. 4.2(b). The intersection routines for a ray with a plane (rectangle) and with an elliptical cylinder are given in appendix B.

4.1.2 Curves and clothoids

For curves with constant radius of curvature, a curved rectangular tunnel section can be modelled by two planes, representing the floor and the ceiling, and by the jackets of two circular cylinders, representing the curved side walls (cf. Fig. 4.3(a)). The curved elliptical tunnel section is modelled by an elliptical

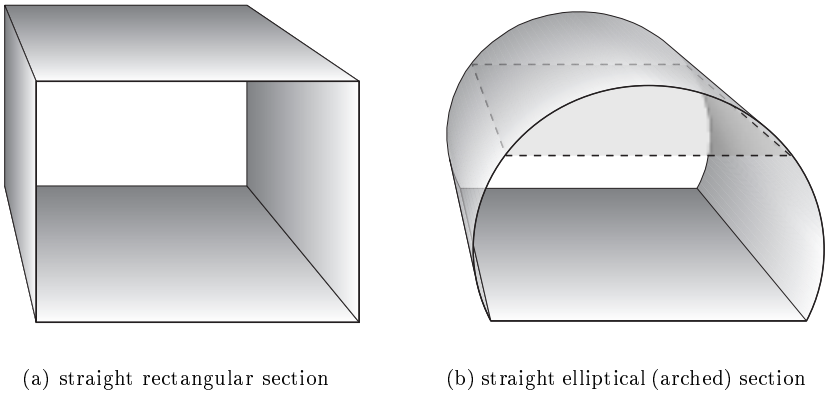


Figure 4.2: Straight sections of a tunnel implemented in the simulation approach

torus and one to two planes, representing the floor and an optional ceiling (cf. Fig. 4.3(b)). The intersection routines for the circular cylinder and the elliptical torus are again given in appendix B.

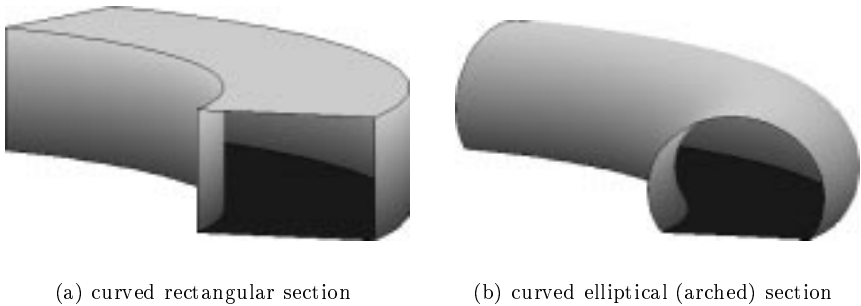


Figure 4.3: Curved sections of a tunnel with constant radius of curvature implemented in the simulation approach

4.1.2.1 Clothoid approximation

In the simulation approach, the clothoid is approximated by an extension of the adjacent straight section and an intermediate circular arc between this extension and the actual curved section. The center of the arc and its radius

$r_a > r_c$ are chosen so that the transitions “straight–arc” and “arc–curve” have continuous slopes (cf. Fig. 4.4). This approximation keeps the original ori-

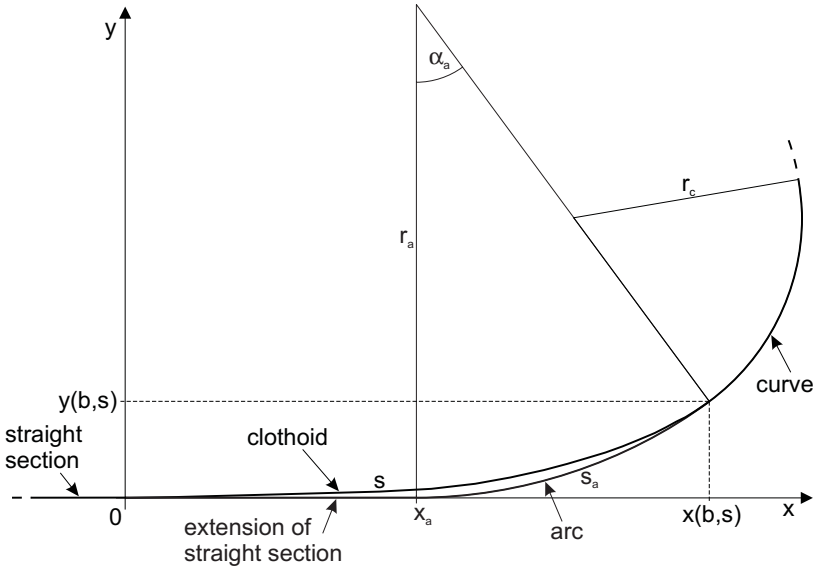


Figure 4.4: Approximation of the clothoid by an extension of the straight section and an intermediate circular arc.

entation of the tunnel’s course and allows to retain the analytical intersection routines of appendix B for curves with constant radius of curvature.

A clothoid is a curve, for which the radius of curvature r is inversely proportional to its arc length s

$$\frac{1}{r} = \frac{s}{b^2}, \quad (b > 0), \quad (4.1)$$

with the proportionality factor $\frac{1}{b^2}$, which in parameter presentation is given by [BS⁺99]

$$x(b, s) = b\sqrt{\pi} \int_0^{\frac{s}{b\sqrt{\pi}}} \cos\left(\pi \frac{u^2}{2}\right) du = \int_0^s \cos\left(\frac{v^2}{2b^2}\right) dv \quad (4.2a)$$

$$y(b, s) = b\sqrt{\pi} \int_0^{\frac{s}{b\sqrt{\pi}}} \sin\left(\pi \frac{u^2}{2}\right) du = \int_0^s \sin\left(\frac{v^2}{2b^2}\right) dv. \quad (4.2b)$$

For a given clothoid, i.e. s and b are known, the parameters of the intermediate arc r_a (radius of the arc) and s_a (arc length), as well as the extension length x_a of the straight section have to be determined. The slope of the clothoid in $(x(b, s), y(b, s))$ can be written as

$$\tan \alpha_a = \tan \alpha_{\text{cloth.}} = \frac{dy}{ds} = \frac{\sin\left(\frac{s^2}{2b^2}\right)}{\cos\left(\frac{s^2}{2b^2}\right)} = \tan\left(\frac{s^2}{2b^2}\right). \quad (4.3)$$

Referring to the geometry of Fig. 4.4, the equation of the circle corresponding to the intermediate circular arc is

$$(x - x_a)^2 + (y - r_a)^2 = r_a^2. \quad (4.4)$$

Solving the above equation with respect to y leads to

$$y = r_a - \sqrt{r_a^2 - (x - x_a)^2}, \quad (4.5)$$

where the negative sign is chosen to match the area of possible transition points with the actual curve. The gradient of the arc in (x, y) , given by

$$\tan \alpha_a = \frac{dy}{dx} = \frac{x - x_a}{\sqrt{r_a^2 - (x - x_a)^2}}, \quad (4.6)$$

is chosen to equal (4.3), leading to

$$\tan\left(\frac{s^2}{2b^2}\right) \stackrel{!}{=} \frac{x - x_a}{\sqrt{r_a^2 - (x - x_a)^2}}. \quad (4.7)$$

With the set of two equations (4.5) and (4.7), the parameters r_a and x_a can be obtained, which determine both the intermediate arc (defined by r_a , x_a) and the extension of the straight section (defined by x_a), yielding

$$x_a = x - \frac{y\left(1 + \sqrt{1 + \tan^2\left(\frac{s^2}{2b^2}\right)}\right)}{\tan\left(\frac{s^2}{2b^2}\right)} \quad (4.8a)$$

$$r_a = y + \frac{x - x_a}{\tan\left(\frac{s^2}{2b^2}\right)}. \quad (4.8b)$$

The values $x = x(b, s)$ and $y = y(b, s)$ can be obtained by evaluating (4.2). The left integrals in (4.2) are the so-called real Fresnel integrals $C(\nu)$ and $S(\nu)$, such that these relations can be rewritten as

$$x(b, s) = b\sqrt{\pi} C\left(\frac{s}{b\sqrt{\pi}}\right) \quad (4.9a)$$

$$y(b, s) = b\sqrt{\pi} S\left(\frac{s}{b\sqrt{\pi}}\right). \quad (4.9b)$$

The Fresnel integrals can be approximated by [AS72]

$$C(\nu) \approx \frac{1}{2} + A(\nu) \sin\left(\frac{\pi}{2}\nu^2\right) - B(\nu) \cos\left(\frac{\pi}{2}\nu^2\right) \quad (4.10a)$$

$$S(\nu) \approx \frac{1}{2} - A(\nu) \cos\left(\frac{\pi}{2}\nu^2\right) - B(\nu) \sin\left(\frac{\pi}{2}\nu^2\right), \quad (4.10b)$$

$$A(\nu) = \frac{1 + 0.926\nu}{2 + 1.792\nu + 3.104\nu^2} \quad (4.10c)$$

$$B(\nu) = \frac{1}{2 + 4.142\nu + 3.492\nu^2 + 6.67\nu^3}, \quad (4.10d)$$

with an absolute error smaller than $2 \cdot 10^{-3}$ for all $\nu \geq 0$. Finally, the length of the intermediate arc is given by

$$s_a = r_a \alpha_a = r_a \frac{s^2}{2b^2}. \quad (4.11)$$

4.2 Stochastic ray launching (Monte-Carlo method)

One important prerequisite for the ray density normalization studied in section 3.2.2 is a homogeneous distribution of the launched rays over the solid angle at the transmitter. De facto it is mathematically impossible to deterministically distribute equally spaced rays over the whole steradian. Therefore, a Monte-Carlo based generation of the launch directions is chosen in the simulation approach¹.

The idea of the stochastic ray launching is to generate random directions in space, which all occur with equal probability [Sob91]. Thus, the constant probability density function that a ray is pointing to a specific direction is

$$p_\Omega = \frac{1}{4\pi}, \quad (4.12)$$

taking into account that the total solid angle equals 4π . The differential solid angle is given by

$$d\Omega = \sin(\theta)d\theta d\phi, \quad (4.13)$$

with $0 \leq \phi < 2\pi$ and $0 \leq \theta \leq \pi$. Using (2.36) to transform (4.13) to the spherical coordinates θ and ϕ , the following probability density function (PDF)

¹Additionally, this stochastic sampling technique provides a means of anti-aliasing [Gla89, chaps. 5,6], resulting in smooth transitions between closely spaced adjacent receiver locations.

is obtained

$$p_{\theta,\phi}(\theta, \phi) = \frac{\sin(\theta)}{4\pi}. \quad (4.14)$$

The one-dimensional probability density functions of the individual coordinates are therefore

$$p_{\theta}(\theta) = \int_0^{2\pi} p_{\theta,\phi}(\theta, \phi) d\phi = \frac{\sin(\theta)}{2} \quad (4.15a)$$

$$p_{\phi}(\phi) = \int_0^{\pi} p_{\theta,\phi}(\theta, \phi) d\theta = \frac{1}{2\pi}, \quad (4.15b)$$

which are mutually independent, because $p_{\theta}(\theta)p_{\phi}(\phi) = p_{\theta,\phi}(\theta, \phi)$. Realizations of θ and ϕ , which follow (4.15), can be generated via two independent uniformly distributed random variables ξ_1 in $[0, 1]$ and ξ_2 in $[0, 1]$ by

$$\theta = \arccos(1 - 2\xi_1) \quad (4.16a)$$

$$\phi = 2\pi\xi_2. \quad (4.16b)$$

The previous two equations are derived by the percentile transformation method [Pap84], i.e. by inversion of the integrals of (4.15) [PT⁺92].

Monte-Carlo approaches have already been used for ray tracing in other contexts. In [Sch95, LL98] the directional pattern of the transmitting antenna is used to distribute the ray directions in order to reduce complexity. Furthermore a so-called Monte-Carlo ray tracing has been proposed in [Mül94a, Mül94b]. In that approach, the positions of the transmitter and image transmitters (for image theory) are varied randomly to simulate clutter, which is thus somehow comparable to the stochastic scattering approach of section 2.3.3.3.

4.3 Coupling into the tunnel

The transmitting antennas are installed either inside, or—e.g. for maintenance reasons—outside a tunnel in the vicinity of the entrance. For an outside location directly in front of the tunnel with the antenna pointing towards the entrance, the total interior of the tunnel up to the first curve is directly illuminated by the transmitting antenna (frontal antenna in Fig. 4.5). For a lateral location, the transmitting antenna is only partially illuminating the interior of the tunnel. For this situation, diffracted rays at the boundary of

the tunnel entrance constitute a considerable part of the total power inside the tunnel [Mar92, MLD94] (lateral antenna in Fig. 4.5). Clearly, the first case with frontal location is preferable in order to maximize the coverage.

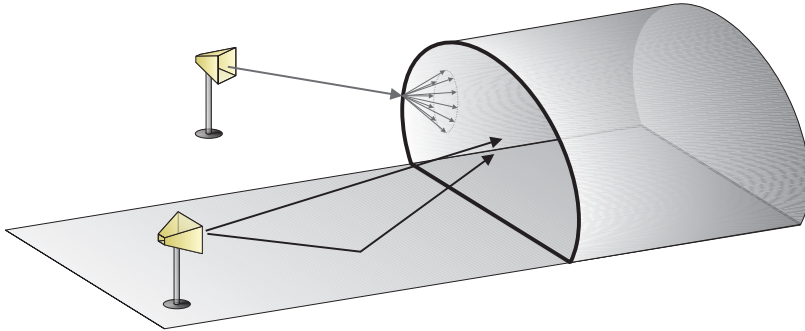


Figure 4.5: Classification of transmitter positions outside a tunnel: frontal or lateral antenna placement

In the simulation approach, all rays which directly enter the tunnel are taken into account for exterior transmitter locations, together with the rays which enter the tunnel via an intermediate ground reflection. The transmitter can be located at any distance over the whole width/cross section of the tunnel, corresponding to the grey-shaded area in Fig. 4.5. In this case, the additional consideration of diffraction would lead to only marginal improvements of the simulation results [Mar92, MLD94] and is therefore not considered any further.

A convenient way to allow for this type of transmitter configuration is by restricting the send-range of launched rays² to the portion of the steradian, which corresponds to the area of direct ray entry into the tunnel, and the area of ray entry via ground reflection. The formulas to determine the send-range for tunnels of rectangular or elliptic (arched) cross sections are given in appendix C.

4.4 Moving obstacles

The goal of communication systems or broadcasting in tunnels is to provide the respective services to people (or machinery). Note that in addition to the empty tunnel scenario, the inclusion of obstacles, especially moving obstacles, is a major point to provide realistic simulation results. As already mentioned

²I.e. the directions, in which the different rays are launched in space.

in sections 2.4.3.2 and 2.4.3.4, the movement of obstacles, as well as receivers or transmitters, leads to a Doppler spread, which may affect the overall system performance.

In the simulation approach, moving obstacles are modelled as floating rectangular boxes of any size, with PEC sidewalls, PEC roofs, and ideally absorbing underbodies. In this way, these floating boxes represent simple models of cars, trucks or train waggons, which are (still) mainly built of metal. Although a more refined model of e.g. a car could be envisaged, this simple “floating box” approach already allows to simulate all important effects, like strong reflectivity, generation of Doppler shifts, shadowing effects, and the ability of electromagnetic waves to propagate between the road and the underbody of a car [SDW00] via an intermediate reflection on the ground. Furthermore, a more meticulous description of a vehicle may not be constructive, since each calculation with moving vehicles only represents an instantaneous snap-shot of the time-variant situation, which almost never exactly maps the real-world scenario. In order to quantify the time-variant behaviour of the channel, the automatic generation of time series, as a sequence of successive snap-shots, is also possible (cf. section 7.3).

4.5 Analysis

The calculation of electromagnetic wave propagation in the simulation approach is performed according to the principles presented in the chapters 2 and 3. The results obtained by the modelling are the received power level, the delay spread, the Doppler spread, and optionally the delay-Doppler-spread function with additional angle-of-arrival information for each point of analysis. These results include the influence of the antennas, for which a polarimetric description by their complex vector directional patterns $\underline{\vec{C}}$ is used [GW98, chap. 2], leading to different results for different states of polarization (e.g. vv , vh , hv , and hh).

Single points of analysis or sequences of points, as they are used for coaxial analyses in tunnels, are represented by reception spheres with radius r_R (cf. section 3.1.2.2). The visible area³ A needed for the ray density normalization of section 3.2.2 is given by

$$A = \pi r_R^2. \quad (4.17)$$

In Figs. 5.1 and 5.5, the principal usage of reception spheres for the generation of line-like analyses is sketched.

³The visible area is the area of a receiver normal to the direction of propagation of a ray.

However, if a whole area of analysis is of interest, as the entire cross section of a tunnel, the usage of reception spheres is disadvantageous: the area would have to be covered by a large number of reception spheres, resulting in a large number of objects, which would prolong the simulation time considerably. In this case, the usage of a reception plane is favourable. A reception plane is a portion of a plane, generally a rectangle, which is subdivided into a mesh of small rectangles, each of them representing a “point” of analysis on the plane. If a ray hits the reception plane, it contributes to the sub-rectangle it is crossing, with the advantage that for the whole reception plane only a single intersection test needs to be performed, no matter how high the resolution of the sub-rectangles has been chosen. The visible area of an element (sub-rectangle) of the reception plane is given by

$$A = A_p |\hat{k} \cdot \hat{n}_p|, \quad (4.18)$$

where A_p denotes the geometrical area of the element (sub-rectangle), \hat{n}_p is the normal vector of the reception plane, and \hat{k} is the propagation direction of the ray. As follows from (4.18), the visible area of an element approaches zero for grazing incidence. Equivalently, the number of rays reaching the element with grazing incidence approaches zero, too. This reveals the disadvantage of the usage of reception planes: suppose the majority of rays is incident on the reception plane under grazing angles. Then a very large number of rays is needed in the process of ray launching, in order to satisfy the “large-number-of-received-rays” requirement of the RDN (cf. section 3.2.2). Fortunately, most relevant rays impinge under almost normal incidence onto the cross section of a tunnel so that a cross-sectional analysis can be obtained relatively fast by the aid of reception planes. However, if a horizontal area is under test, the simulation time may be considerably slower due to the required large number of rays (cf. section 6.4). In Fig. 6.9(a), the usage of a horizontal reception plane is visualized.

4.6 Additional remarks on the implementation

In addition to the above mentioned analytical intersection routines and the possibility to employ reception planes, several other ray-tracing acceleration techniques are employed in the simulation approach, in order to speed up the simulation time and thus allow for a large number of rays. The concepts of spatial subdivision and bounding volumes (both [Gla89, chap. 6]) are utilized in conjunction with the multiple usage of intersection points [SW98].

4.7 Summary

In this chapter, the particulars of the simulation approach were introduced. The possible tunnel geometries and their treatment in the simulation tool were presented. The stochastic ray launching, which is mandatory for the RDN of chapter 3, the handling of transmitting antennas at exterior positions in front of a tunnel entrance, as well as the two principal modes of analysis, i.e. along trajectories and over entire cross sections, were described.

After the treatment of ray-optical propagation modelling in chapter 2, the particulars of ray tracing in a tunnel environment in chapter 3, and the simulation approach addressed here, the next two chapters are devoted to the validation of the proposed modelling techniques. To do this, a theoretical verification is performed in the next chapter using simple canonical geometries, for which analytical reference solutions exist.

Chapter 5

Theoretical verification

In order to validate the different ray-optical wave propagation modelling techniques of chapters 2 and 3, the proposed approaches are compared to theoretical “reference solutions” in canonical geometries. This theoretical verification will be followed by comparisons with measurements in chapter 6.

The first canonical problem chosen in section 5.1 is a straight PEC rectangular waveguide. In this geometry, a field-theoretical reference solution is given by the method of Green’s functions. The Green’s function of a PEC rectangular waveguide serves to validate the implementation of the exclusively existing ray-optical reference solution, namely, image theory. Image theory is further used to evaluate the performance of the different ray-launching techniques, especially the RDN-based field and power traces. Unfortunately, in curved geometries no ray-optical reference solution such as image theory exists (cf. section 3.1.1). Therefore, another strategy for the validation is chosen in section 5.2. First, an ideal metallic corrugated circular waveguide is utilized as the second canonical geometry for the purpose of qualitative and quantitative verification of the ray density normalization. The reference solution for this type of curved geometry is based on fast mode decomposition. Furthermore, the different techniques are compared to each other to reveal possible differences between them. Finally, the stochastic scattering approach of section 2.3.3.3 is compared to the Kirchhoff rough-surface scattering models in section 5.3.

5.1 Verification in planar geometry: the rectangular waveguide

5.1.1 Geometry of the rectangular waveguide

The canonical geometry chosen to validate the different modelling techniques in planar geometry is the rectangular waveguide. The geometry of the rectangular waveguide is depicted in Fig. 5.1. The dimensions of the cross section are

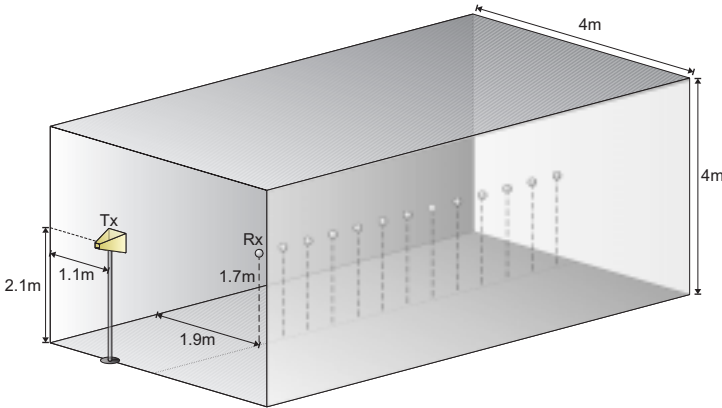


Figure 5.1: Geometry of the rectangular waveguide with asymmetric transmitter and receiver positions

$4\text{m} \times 4\text{m}$. The transmitter is situated at the entrance of the waveguide, 1.1m from the left wall and 2.1m above ground. The receivers have a variable distance to the transmitter, 1.9m from the left wall and 1.7m above ground. The carrier frequency is $f = 1\text{GHz}$ for all calculations with this geometry. The scenario is chosen to avoid any symmetry effects [CJ96a].

5.1.2 Validation of the image theory by the Green's function approach in PEC rectangular waveguide

The ray-optical reference solution available for planar geometries is given by the image theory [MW74a, MLD94, Kle93, Rem93]. All other techniques have to match the results provided by the image theory. In order to verify this reference method, it is first of all compared to a field-theoretical solution in a PEC rectangular waveguide obtained by means of the Green's function. In engineering terminology, the Green's function is equivalent to the spatial impulse response of a system [Bal89]. Thus, knowledge of the Green's function

for a given scenario allows to determine the solution for a variety of driving sources by means of convolving excitation and Green's function. Consequently, if the source excitation is a spatial impulse (Dirac function), the response of the system is given by the Green's function itself. The Green's function¹ for a PEC rectangular waveguide must satisfy a partial differential equation, the scalar Helmholtz equation in cartesian coordinates, and the boundary conditions imposed by the waveguide. The Green's function can be obtained by expansion into a series of eigenfunctions of the corresponding homogeneous differential equation. The derivation is discussed thoroughly in [Bal89, chap. 14], [Tai93, chap. 5] and is omitted for the sake of simplicity.

For image theory, the scenario shown in Fig. 5.1 is assumed with perfectly electric conducting boundaries. The transmitting antenna is modelled as a vertically polarized Hertzian dipole, which is equivalent to a Dirac-impulse source in vertical direction. If the receiver is also modelled as a vertically polarized Hertzian dipole, the received voltage will be proportional to the vertical component of the field. On the other hand, the vertical field component excited by this type of transmitting antenna is given by the Green's function relating a vertical source to a vertical response² (multiplied by $j\omega_0\mu_0$ and the weight of the Dirac impulse [Bal89, Tai93]). This allows a direct comparison of image theory and the Green's function approach.

According to (2.23), the reflection coefficients for PEC boundaries are $R_{\parallel} = 1$ and $R_{\perp} = -1$. In other words, the reference geometry of a PEC rectangular waveguide is a theoretically lossless environment. As a result, even rays experiencing a large number of reflections still contribute significantly to the total field at the receiver in the ray-optical imaging approach. The only limiting factor in this case is the traversed path length and the associated spreading, leading to a decrease of the field with increasing distance (2.14). Consequently, a large number of reflections has to be considered in the simulation in order to achieve sufficient convergence. The number N_m of rays reaching the receiver via m reflections in a rectangular waveguide is given by

$$N_m = \begin{cases} 1 & \text{for } m = 0, \\ 4m & \text{otherwise.} \end{cases} \quad (5.1)$$

The total number of rays N with a maximum of m_{max} reflections is therefore

$$N = \sum_{m=0}^{m_{max}} N_m = 1 + 2m_{max}(m_{max} + 1). \quad (5.2)$$

¹In the general case, the Green's function is a dyadic [Tai93].

²The total field excited by a vertically polarized Hertzian Dipole would be given by a vectorial Green's function.

The computational cost, however, is not only determined by the number of rays, but also by the number of intersection/reflection routines, which have to be executed. For a ray with m reflections, $(m + 1)$ such tests have to be performed, resulting in a computational complexity of order $O(m^3)$ [SDK96].

Figure 5.2 compares results of the Green's function approach and the ray-optical image theory in the PEC waveguide of Fig. 5.1 for distances between 10m and 20m from the transmitter. Both curves are normalized to their re-

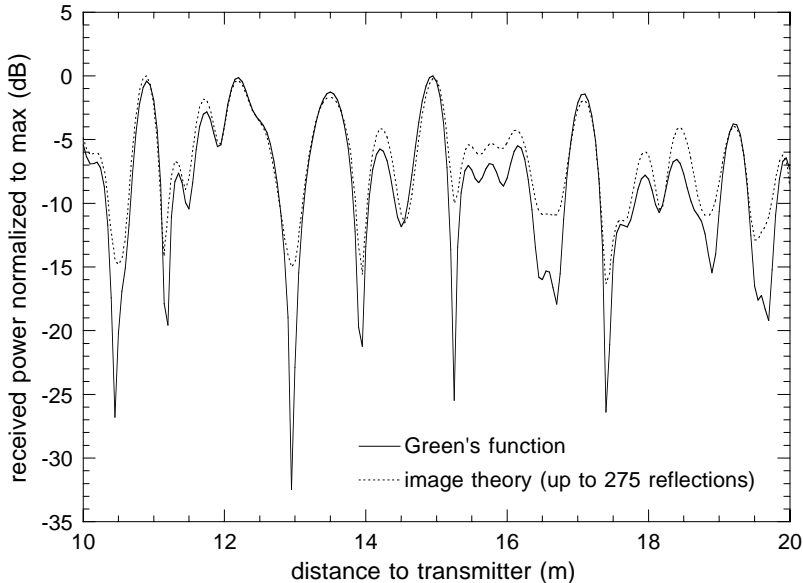


Figure 5.2: Comparison of Green's function approach and ray-optical image theory in PEC rectangular waveguide of Fig. 5.1, excited by a vertically polarized Hertzian dipole, $f = 1\text{GHz}$ (here, the speed of light is set to $c_0 = 3 \cdot 10^8 \frac{\text{m}}{\text{s}}$, cf. [CJ95, CJ96a, CJ96b, CJ97])

spective maximum values. Although up to 275 reflections have been traced, resulting in a total number of $N = 151801$ rays per receiver (cf. (5.2)), still no perfect convergence and therefore no perfect agreement could be achieved between image theory and Green's function approach due to the lossless geometry. Furthermore, the infinite series solution of the Green's function is also very sensitive to slight changes in the parameters, e.g. the speed of light c_0 [SW98]. Bearing in mind these difficulties, the comparison of the two entirely different methods validates the ray-optical image approach quite satisfactorily. Therefore, image theory is used in the following to verify the RDN-based

methods of chapter 3.

5.1.3 Validation by image theory in a rectangular waveguide with dielectric boundaries

Fortunately, real tunnels are rarely made of PEC boundaries but of rock, reinforced concrete, or other building materials. For this type of (lossy) dielectric materials, the reflectivity is always below unity, resulting in a much smaller number of reflections needed for satisfactory convergence. The minimum number of reflections, however, is increasing with increasing distance between transmitter and receiver: this is because for grazing incidence, which occurs for large distances, the reflectivities approach unity (2.24). To quantify this

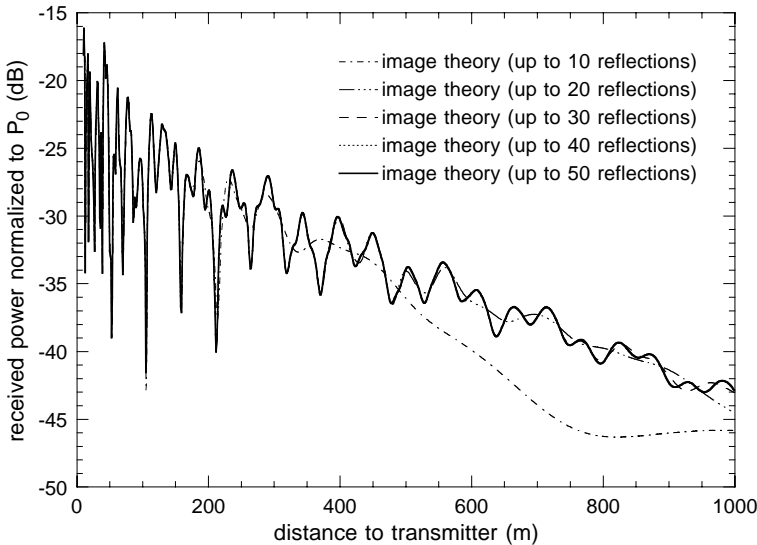


Figure 5.3: Convergence of image theory in the rectangular waveguide of Fig. 5.1 made of dielectric boundaries with $\epsilon_r = 5$, maximum number of reflections $m_{max} = 10 \dots 50$, vertically polarized isotropic transmitter and receivers, $f = 1\text{GHz}$

behaviour, the same rectangular waveguide as in the previous section (cf. Fig. 5.1) is chosen, but this time made of smooth dielectric boundaries with $\epsilon_r = 5$, corresponding to dry concrete. Figure 5.3 depicts the results of image theory for different maximum numbers of reflections $m_{max} = 10 \dots 50$ at distances up to 1km from the source. Both the transmitting and the receiving antennas are modelled with isotropic vertically-polarized patterns. In the vicinity of the

source up to 200m, as few as $m_{max} = 10$ reflections are sufficient; at farther distances of about 1km, however, at least $m_{max} = 40$ reflections should be considered in order to achieve reliable results.

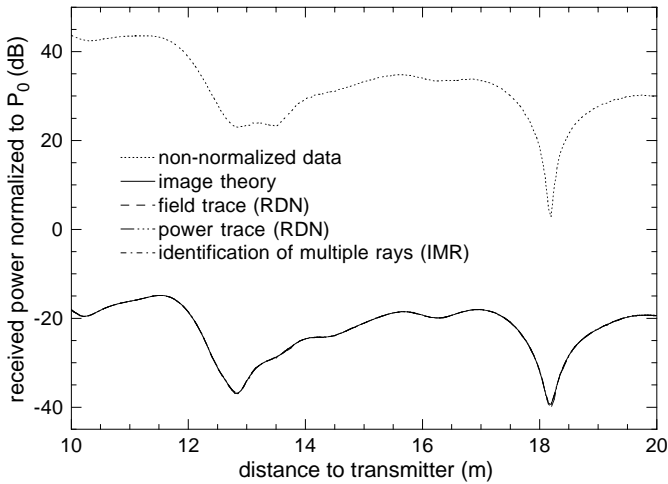
For the comparison of the different ray-optical techniques, again the same scenario as in Fig. 5.1 is chosen at distances from 10m to 20m to the transmitter. Except for image theory and the method of power flow, which require much less rays to be traced, 20 million rays are launched equally distributed in space by the stochastic ray launching and up to 10 reflections are included, ensuring sufficient convergence of the results. Figure 5.4(a) depicts the coherent comparison of the reference solution, the pairwise identification of multiple rays (IMR), the field and the power trace with RDN, and the uncorrected “raw” ray launching. Obviously, the non-normalized curve does not fit the reference solution. Apart from the very high predicted level, it generally decreases too fast with distance, indicating a non-constant offset. At increased distances, less rays reach the receiver resulting in a decreasing total received power level. On the other hand, the two RDN-based approaches and the IMR match the image theory results very well. The required computation times for the different methods on a Hewlett Packard C-series workstation with 240MHz clock-rate are compared in Table 5.1.

Table 5.1: Computation times of different ray-optical methods in rectangular waveguide of Fig. 5.4 on Hewlett Packard C-series workstation with 240MHz clock-rate

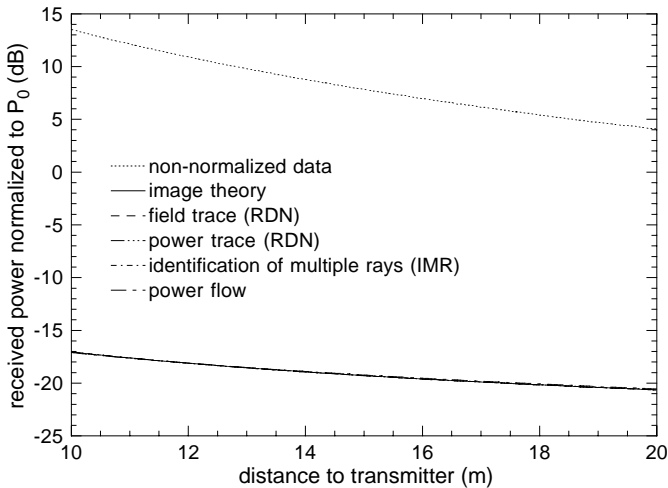
	image theory	RDN (PT/FT)	IMR	power flow
analysis	coh./inc.	coh./inc.	coh./inc.	inc.
N	$201 \cdot 221$	$20 \cdot 10^6$	$20 \cdot 10^6$	$1 \cdot 10^5$
time	44s	1:30h	2:30h	3:40min

Figure 5.4(b) shows the same comparison but for incoherent ray combination. In this figure, it is clearly seen that the “raw” ray launching experiences not only an offset by a constant value. Additionally to the RDN and IMR approaches, the method of power flow is also included in the comparison. Even the power flow method, assuming a constant distribution over the whole cross section, leads to the same results as the image theory with far less computational cost than the RDN or IMR approaches. This is mainly due to a significantly reduced number of required rays for converging results: generally convergence is already achieved for less than 10^5 rays [LL98, CG99] (cf. chapter 7).

The previous two figures reveal the applicability and power of the proposed



(a) coherent analysis



(b) incoherent analysis

Figure 5.4: Comparison of different ray-optical approaches in the rectangular waveguide of Fig. 5.1 made of dielectric boundaries with $\epsilon_r = 5$, vertically polarized isotropic transmitter and receivers, $m_{max} = 10$, radius of reception spheres $r_R = 10\text{cm}$, 201 receiver points, $f = 1\text{GHz}$

RDN-based ray launching in planar geometry. To allow for curved boundaries, a circular waveguide is considered in the next section.

5.2 Verification in curved geometry: the circular waveguide

In the previous section it was shown that the proposed RDN-based methods work well in a rectangular shaped straight tunnel. Unfortunately, in tunnels of curved cross section no ray-optical reference solution like image theory is available. This is because an unambiguous image of a point only exists at planar surfaces (cf. section 3.1.1). Thus, another strategy for validation has been chosen. First, the RDN-based approaches are theoretically validated in an ideal metallic corrugated circular waveguide. The reference solution for this type of curved geometry is based on fast mode decomposition. This is followed by a comparison of the different methods in a tunnel of circular cross section with dielectric boundaries to reveal any possible differences between them.

5.2.1 Choice of the canonical (reference) geometry

Although approximate modal solutions are available to determine wave propagation in curved rectangular waveguides/tunnels with large radii of curvature [MW74b], no exact solution exists for curved waveguides—at least to the best of the author’s knowledge. Therefore, the canonical geometry chosen to theoretically validate the different modelling techniques is the straight circular waveguide. The validation in a geometry of real three-dimensional curvature, i.e. curvature in cross section and course, is performed by measurements in chapter 6. The geometry of the circular waveguide is depicted in Fig. 5.1. The radius of the circular cross section is $r_{cs} = 2\text{m}$. The position of the transmitter is either centric or 1m above the tunnel axis. For simulation work, the receivers are either situated parallel to the tunnel axis, or in the plane of the cross section. The carrier frequency is $f = 1\text{GHz}$ for all calculations with this geometry.

5.2.2 Corrugated circular waveguide

For the theoretical verification, a fictitious ideal metallic corrugated circular waveguide is assumed. An ideal corrugated waveguide is a special waveguide with Fresnel reflection coefficients $R_{\parallel} = R_{\perp} = -1$ (2.24). This behaviour is achieved by a special geometry of grooves on the inner surface of the waveguide, also named corrugation [Kil90]. In practice, corrugated waveguides are e.g.

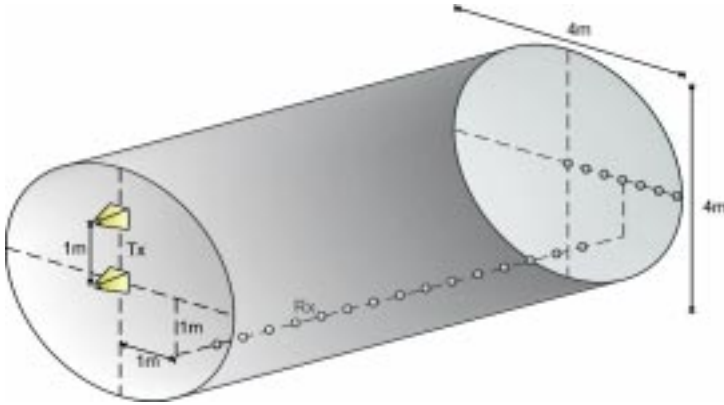


Figure 5.5: Geometry of the circular waveguide with different transmitter and receiver positions

used in microwave technology for power transmission or dish antenna feed systems. The reference solution utilized in this geometry is based on fast mode decomposition [MT99]. The field is decomposed in modes, where only the propagating modes are considered.

Figure 5.6 shows the comparison of the analytical method and the RDN-based power trace in the waveguide of Fig. 5.5 at $f = 1\text{GHz}$. An ideal isotropic transmitter is placed in the center of the waveguide, the receivers with radii $r_R = 4\text{cm}$ are situated along the line center-to-outer-wall at 10m from the transmitter (cf. Fig. 5.6). For the RDN-based power trace, two different curves are plotted in Fig. 5.6: one with the weighting factors given by (3.26); the other is bound to a maximum number of multiple rays $M_{max} = N/1000$ in order to predict correct values in caustics (cf. section 3.3.3). Taking into account the ideal lossless surface of the corrugated waveguide, even rays with a high number of reflections are still contributing to the overall reception level. Therefore, sufficient convergence of the ray tracing is only possible with considerable computational effort. For the simulation in Fig. 5.6 200 million rays have been traced with up to 200 reflections. The simulation time on the HP workstation of Table 5.1 was about one day. Despite the critical circumstances, which represent a numerical worst-case scenario in ray launching, a very good agreement of the results is observed. This validates the developed new ray density normalization, as well as the implementation of ray tracing.

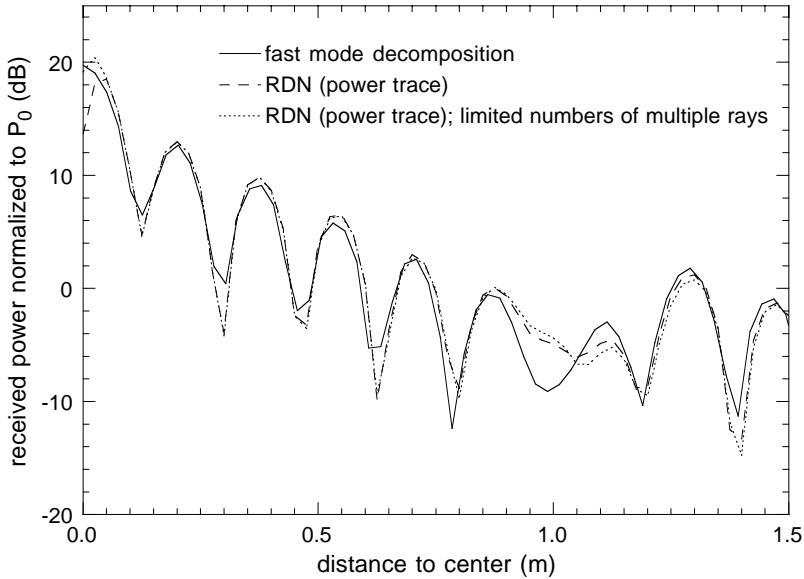


Figure 5.6: Comparison of RDN and mode decomposition in an ideal metallic corrugated circular waveguide from center to outer wall, distance to transmitter 10m, radius of the waveguide 2m, radius of the reception spheres $r_R = 4\text{cm}$, 80 receiver points, centric position of isotropic transmitter, $f = 1\text{GHz}$

5.2.3 Comparison of the different techniques in circular waveguide with dielectric boundary

After the theoretical validation of the RDN-based methods in the previous section, the different approaches applicable in curved geometry are compared amongst each other. The same geometry as in Fig. 5.5 is used and, as with the rectangular waveguide of section 5.1.3, the analysis is performed at distances from 10m to 20m from the transmitter. Figure 5.7 depicts the coherent and the incoherent analysis of the “raw” ray launching, the RDN-based methods, the IMR, and the method of power flow (incoherent analysis only). The same simulation parameters as in the rectangular waveguide have been chosen. The computation times are comparable to the ones given in Table 5.1.

A similar result as in the planar geometry is observed: the two RDN-based methods and the IMR are equivalent. The non-normalized curves, shown in the upper right corner of Fig. 5.7 on a different scale, are obviously wrong. The only difference between the different approaches is the behaviour of the power flow. Although the power flow approaches the RDN and IMR results

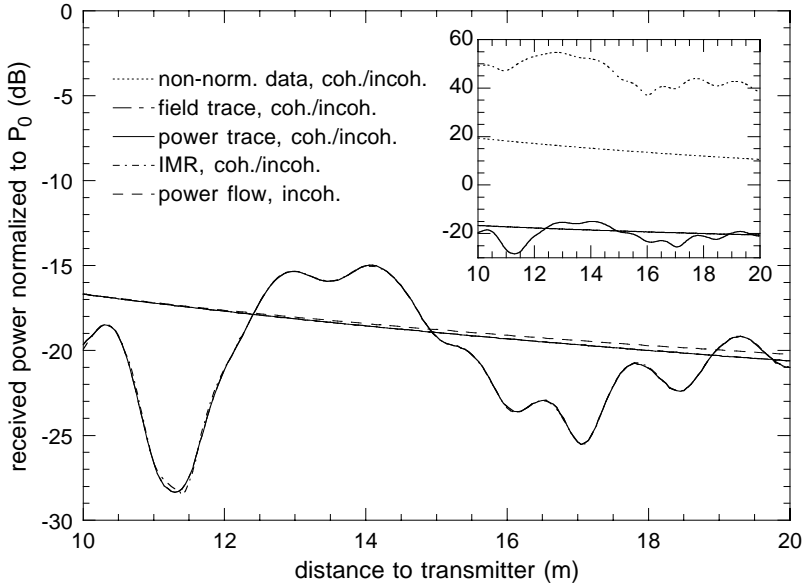


Figure 5.7: Coherent and incoherent comparison of the different approaches applicable in the circular waveguide of Fig. 5.5 made of dielectric boundaries with $\varepsilon_r = 5$, vertically polarized isotropic transmitter and receivers, $m_{max} = 10$, $r_R = 10\text{cm}$, 201 receiver points, $f = 1\text{GHz}$

rather closely, no perfect match is achieved for distances $> 14\text{m}$ to the transmitter. The reason for this lies in the “equi-energy-distribution” assumption for the power flow approach, which is approximately the case in the rectangular waveguide but not in the circular one. The accumulation of energy in some parts of the cross section becomes even more important in curved tunnels (known as whispering gallery effect [Wai67]) and is treated in the following two chapters in more detail.

The IMR method is not used in the remainder of this thesis because of the prohibitive memory requirements for the intermediate ray storage³ and the prolonged simulation times due to the post-processing and the storage itself. Furthermore, the IMR fails in and near caustics [SW98], as already mentioned in section 3.1.2.3.

³More than 500 megabyte were necessary only for the simulation presented in Fig. 5.7.

5.3 Stochastic scattering approach

In order to validate the stochastic scattering approach described in section 2.3.3.3, it is compared to the two rough-surface scattering Kirchhoff models [UMF83, GW98]. The first is the Kirchhoff model with scalar approximation for slightly rough surfaces, which states the mean value of the coherent scattering component. The second Kirchhoff model is based on a stationary phase approximation for very rough surfaces, which delivers the mean square value of the incoherent or diffuse scattering component. Unfortunately, the two Kirchhoff approximations are only applicable in different (opposite) validity regions and cannot be combined to yield the overall mean scattering intensity for arbitrary surface roughness, which is defined by the sum of coherent and incoherent components.

In contrast, the stochastic scattering approach developed here is able to deliver instantaneous realizations of a scattering process, which contain at the same time the coherent and the incoherent component. For a comparison with the Kirchhoff models, mean values of the different scattering components have to be generated, which can be obtained by averaging a sufficiently large number of realizations.

5.3.1 Arrangement and procedure

For the comparison, the scenario of Fig. 5.8 is chosen: a rough, rectangular plate of dimension $A_{rp} = L_x \times L_y$ is illuminated by a point source situated at θ_i , ϕ_i and r_i . The scattering of the rough plate is calculated by the stochastic scattering approach and the Kirchhoff models. For the stochastic scattering, the plate is hit by N rays, which are equally spaced in the x - and y -directions on the plate. Each ray is reflected according to the stochastic scattering approach of section 2.3.3.3, i.e. the local tangential planes at each reflection point are varied following (2.41) and a Gaussian height variation. At a distance r_s , the resulting electric field (coherent analysis) is calculated together with the power sum (incoherent analysis) with a resolution of $\Delta\theta$ and $\Delta\phi$. For the averaging, the procedure is repeated M times. The results have to be transformed to yield the polarimetric radar cross section (RCS) matrices per unit area, to allow a direct comparison with the analytical Kirchhoff models, which directly yield the RCS matrices.

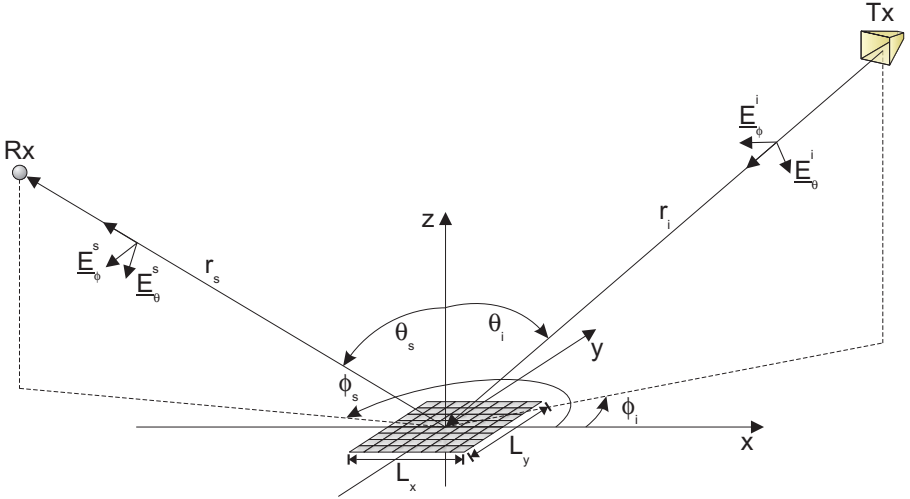


Figure 5.8: Scenario and alignment convention for the comparison of the stochastic scattering approach and the Kirchhoff models

5.3.1.1 Radar cross section per unit area

Generally, a scattering process is described by the complex polarimetric scattering matrix $[\underline{S}]$

$$\underline{\vec{E}}^s(r_s) = \frac{e^{-jk_0 r_s}}{r_s} [\underline{S}] \underline{\vec{E}}^i, \quad (5.3)$$

where $\underline{\vec{E}}^i$ and $\underline{\vec{E}}^s$ denote the incident plane wave and the scattered spherical wave in the far field, respectively, both given in their respective local θ and ϕ components following the alignment convention depicted in Fig. 5.8. According to the definition in (5.3), $[\underline{S}]$ is independent of the distance r_s . The radar cross section is now used to characterize the magnitude of the scattering. It is equivalent to the area absorbing the amount of power of the incident plane wave, which is necessary for an isotropic scatterer to cause the same radiation intensity at the point of interception as the actual (directive) scattering process [GW98]. The components of the polarimetric RCS matrix σ_{pq} are related to the components of the scattering matrix \underline{S}_{pq} by

$$\sigma_{pq} = 4\pi |\underline{S}_{pq}|^2, \quad (5.4)$$

where the polarization indices p, q stand for any combination of the θ and ϕ components. The dimension of σ_{pq} is square meter according to (5.3) and

(5.4). For area-extensive scatterers of area A , often the RCS matrix per unit area $[\sigma^0]$ with

$$[\sigma^0] = \frac{1}{A}[\sigma] \quad (5.5)$$

is used [RB⁺70, UMF83].

5.3.1.2 Determination of the RCS matrix by ray tracing using the stochastic scattering approach

For a given \vec{E}^s , the scattering coefficients can be obtained by the aid of (5.3)–(5.5). Thus, the RCS matrix is determined simply by substituting \vec{E}^s in (5.3) with the resulting field of the ray-tracing based stochastic scattering in the scenario of Fig. 5.8.

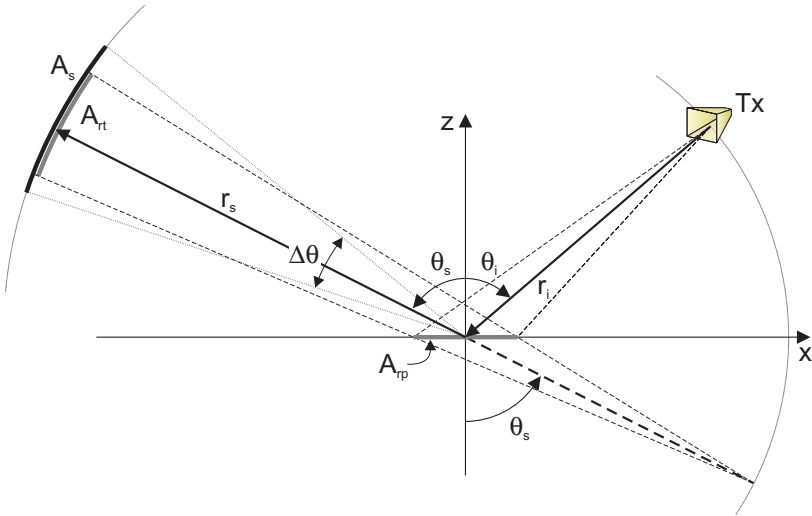


Figure 5.9: Divergence of scattered and incident ray tubes linked by the scattering plane A_{rp} , together with the reception areas A_s given by (5.7)

For the ray tracing, one has to consider that the scattered ray density n_d^s is related to the incident ray density n_d^i by (cf. Fig. 5.9)

$$n_d^s(r_s) = \frac{\cos \theta_i}{\cos \theta_s} \frac{r_i^2}{(r_i + r_s)^2} n_d^i, \quad (5.6)$$

where θ_i and θ_s denote the incident and the scattering angle, respectively. Note that for the specular direction given by $\theta_s = \theta_i$, (5.6) reduces to (3.3)

with $\rho_1^r = \rho_2^r = r_i$ and $s = r_s$. Furthermore, the reception areas determined by the angular spacing $\Delta\theta$ and $\Delta\phi$ at a large distance r_s from the center of the scattering plane are given by

$$A_s \approx r_s^2 \Delta\theta \Delta\phi \sin \theta_s. \quad (5.7)$$

The incident ray density is determined by

$$n_d^i = \frac{N}{A_{rp} \cos \theta_i}, \quad (5.8)$$

resulting in an actual number of rays N_s at the reception area A_s of

$$N_s = n_d^s(r_s) A_s = \frac{N \Delta\theta \Delta\phi \tan \theta_s}{A_{rp}} \frac{r_i^2 r_s^2}{(r_i + r_s)^2}. \quad (5.9)$$

For a reflection with one single locally plane wave (and therefore ray) impinging on A_{rp} , the correct number, taking into account the divergence of the reflected tube of rays, is

$$N_0 = \frac{r_i^2}{(r_i + r_s)^2} \frac{1}{A_{rp}} A_{rp} = \frac{r_i^2}{(r_i + r_s)^2}. \quad (5.10)$$

Since the number of rays is proportional to the power density, the electric field at the output of the ray tracing has to be weighted by the square root of the ratio N_0/N_s given by

$$\sqrt{\frac{N_0}{N_s}} = \sqrt{\frac{A_{rp} \cos \theta_s}{N A_s}} = \sqrt{\frac{A_{rp}}{N \Delta\theta \Delta\phi \tan \theta_s} \frac{1}{r_s}}. \quad (5.11)$$

Finally, the results are averaged over M different realizations. Using (5.11) together with (5.3)–(5.5), it turns out that the resulting RCS matrix per unit area is independent of both the distance r_s and the area A_{rp} of the scattering plane.

5.3.1.3 The Kirchhoff models

The Kirchhoff models with scalar approximation and stationary phase approximation directly yield the RCS matrices. The formulation of the models is e.g. given in [RB⁺70, chap. 9] or [UMF83, chap. 12].

The scalar approximation for the coherent scattering component implies that all points of reflection lie in the same plane. Under this assumption, all reflected elementary waves of an incident uniform plane wave are in phase and can therefore be combined coherently in the far field. The pattern produced

by the coherent component depends mainly on the diffraction pattern of the surface in the absence of roughness. The effect of a slight roughness is to reduce the magnitude of this pattern. In addition to the tangential plane assumption (2.44), the validity of this model is limited by

$$\frac{2\sigma_h}{L} < \frac{1}{2\sqrt{2}}. \quad (5.12)$$

The condition says that the RMS slope of the surface must be small.

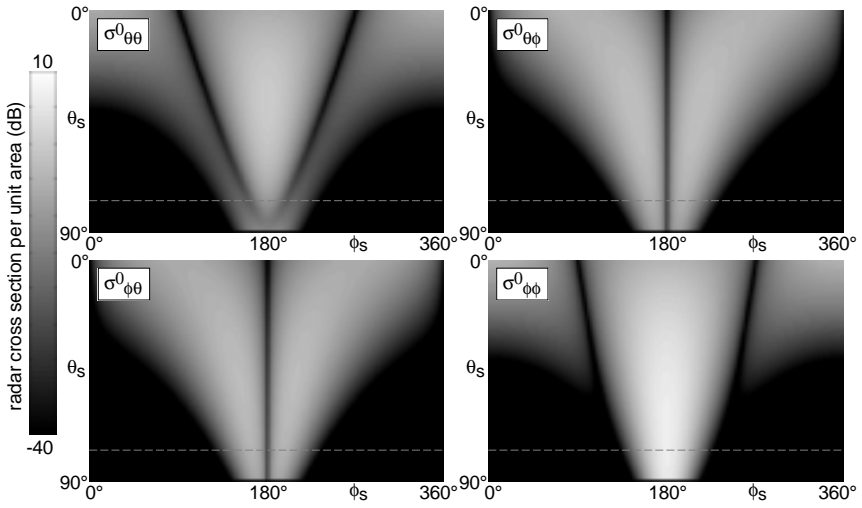
The stationary phase approximation of the diffuse scattering component is based on the contention that the averaged scattering from a very rough surface comes from the few areas, which specularly reflect. The additional condition for the validity of this model is given by

$$\left| 2\pi \frac{\sigma_h}{\lambda_0} (\cos \theta_i + \cos \theta_s) \right| > \pi. \quad (5.13)$$

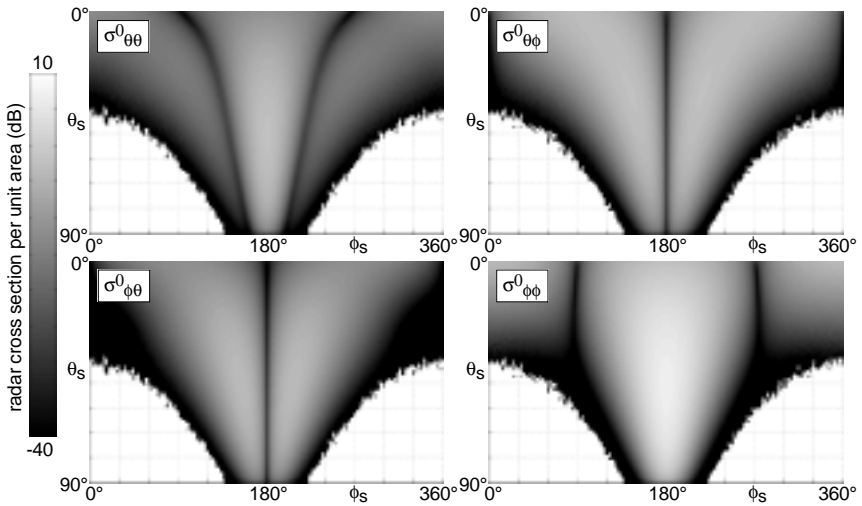
The condition requires that the root mean square (RMS) of the phase difference between two rays reflected at any two points on the surface has to be sufficiently large. Thus permitting to gather the scattered power from each specular point incoherently.

5.3.2 Comparison of the methods

First, a relatively rough surface with a standard deviation of the surface heights $\sigma_h = 0.7\lambda_0$, correlation length $L = 4\lambda_0$, $\underline{\varepsilon}_r = 10 - j3$ and $\underline{\mu}_r = 1$ of size $L_x = L_y = 8\lambda_0$ is considered. For the ray-optical stochastic scattering approach, the isotropic source is situated at $\theta_i = 60^\circ$ and $\phi_i = 0^\circ$, at a distance of $r_i = 2000\lambda_0$ from the plane. The rays impinge separated by $\lambda_0/10$ in the x - and y -direction on the surface, resulting in $N = 81 \times 81 = 6561$ rays per realization. The resulting field is determined in the upper hemisphere at a distance $r_s = 2000\lambda_0$ from the center of the plane, corresponding to approximately 8 times the far-field distance, with a quantization of $\Delta\theta = \Delta\phi = 1^\circ$. A total of $M = 10^5$ realizations is taken for the ensemble averaging. Figure 5.10 depicts the components of the RCS matrix per unit area of the diffuse (or incoherent) scattering component for the Kirchhoff model with stationary phase approximation (Fig. 5.10(a)) and for the stochastic scattering approach (Fig. 5.10(b)). The broken line in Fig. 5.10(a) indicates the limit of the validity region of the Kirchhoff model according to (5.13). The absence of colour in the lower corners in Fig. 5.10(b) indicates that no ray reaches these regions in the stochastic scattering approach. The absolute value in the specular direction of e.g. $\sigma_{\phi\phi}^0$ is in both cases 6.3dB. The coherent scattering component is negligible for this type of surface (more than 50dB below the incoherent component).

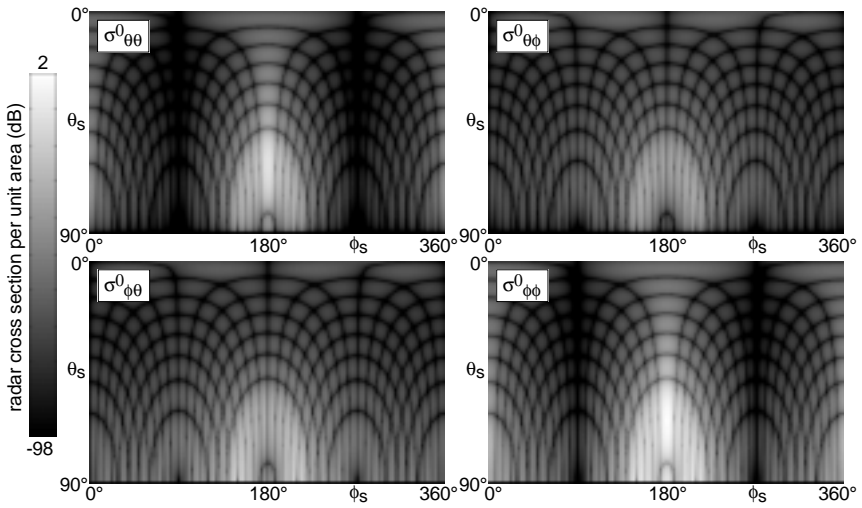


(a) Kirchhoff model with stationary phase approximation

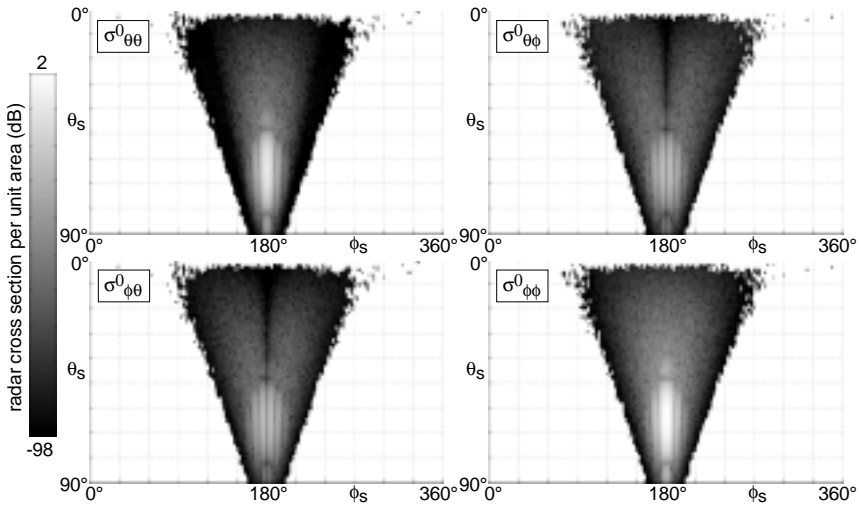


(b) stochastic scattering approach

Figure 5.10: RCS per unit area of the incoherent scattering component of the scenario according to Fig. 5.8 ($\sigma_h = 0.7\lambda_0$, $L = 4\lambda_0$, $L_x = L_y = 8\lambda_0$, $\theta_i = 60^\circ$, $\phi_i = 0^\circ$)



(a) Kirchhoff model with scalar approximation



(b) stochastic scattering approach

Figure 5.11: RCS per unit area of the coherent scattering component of the scenario according to Fig. 5.8 ($\sigma_h = 0.35\lambda_0$, $L = 4\lambda_0$, $L_x = L_y = 8\lambda_0$, $\theta_i = 60^\circ$, $\phi_i = 0^\circ$)

A direct comparison of the coherent scattering components of the stochastic scattering approach and the Kirchhoff model with scalar approximation is somewhat more delicate. The difficulty lies in the nature of the Kirchhoff model: the scattering intensity in a specific direction, as predicted by this model, is mainly determined by the diffraction pattern of the surface and not by its roughness. In fact, the influence of the surface roughness is most pronounced in the specular direction resulting in a reduced scattering intensity retaining the characteristic pattern produced by the geometry of the surface. Figure 5.11(a) depicts this type of pattern calculated by the Kirchhoff model with scalar approximation. The same surface as in the comparison of the diffuse components is used, but with half the roughness, i.e. $\sigma_h = 0.35\lambda_0$. The typical diffraction pattern of a rectangular plate [Bal89] can be distinguished, the influence of roughness, as already indicated, is restricted to a diminution of the intensity. Noting the large dynamic range of these images compared to the incoherent component of Fig. 5.10, it is obvious that the coherent component is only significant in the vicinity of the specular direction. Figure 5.11(b) displays the equivalent images obtained by the stochastic scattering approach. In contrast to the Kirchhoff model, these results solely reflect the influence of the surface roughness. For a perfectly smooth surface, the stochastic scattering approach would equal specular reflection, i.e. a single point. Also for the stochastic scattering approach, one can clearly distinguish the interference pattern introduced by the limited area-extend of the surface. The absolute value in the specular direction of e.g. $\sigma_{\phi\phi}^0$ is -0.7dB for the Kirchhoff model and 1.0dB for the stochastic scattering approach. For the incoherent scattering component, this value is 12.4dB for both models and thus still much larger than for the coherent scattering. According to (5.12), the value of $\sigma_h = 0.35\lambda_0$ lies outside the validity range of the Kirchhoff model with scalar approximation by a factor of two. A smaller value of the roughness leads to almost the same images for the Kirchhoff model, but with a larger maximum value. However, the actual influence of the surface roughness on the directional pattern, as given by the stochastic scattering approach, becomes less visible. Thus for visualization purposes, the value of $\sigma_h = 0.35\lambda_0$ was chosen.

The very good qualitative and quantitative agreement proves the validity of the proposed stochastic scattering approach, especially when bearing in mind that the Kirchhoff models are only approximate solutions. The great advantage of the stochastic scattering approach, as already mentioned, is its ability to deliver instantaneous realizations of the scattering process including both the coherent and the incoherent component.

This means that for each specific application an optimized technique is available: for coverage planning purposes, where the mean values of the received power levels are of interest, specular reflection together with the mod-

ified Fresnel reflection coefficients of section 2.3.3.2 are the best choice. For system design or evaluation purposes, however, the stochastic scattering approach should be used instead, with its ability to generate instantaneous (and therefore varying) realizations of the actual scattering processes.

5.4 Summary

In this chapter, the proposed ray-optical modelling techniques and the stochastic scattering approach have been verified theoretically with reference solutions available for simple geometries. In the next chapter, they are further validated by comparisons with measurements. Special emphasis is given to the performance in real three-dimensional curvature, which to date could not be evaluated theoretically due to the lack of reference solutions.

Chapter 6

Experimental verification by measurements in scaled model tunnels at 120GHz

In the previous chapter the proposed ray density normalization has been validated theoretically. This was only possible in idealized geometries for which reference solutions exist. To test the RDN in realistic geometry, measurements have been carried out at 120GHz in scaled model tunnels built of concrete and stoneware. The performance of the modelling approach in real three-dimensional curvature is therefore of primary interest. The choice of scaled model tunnels rather than real tunnels for the initial verification is primarily due to availability and to ensure reproducibility. Furthermore, the possibility of investigating different arrangements and scenarios together with the ability to perform analyses over the entire cross section of the model tunnels are additional advantages. Comparisons with measurements in real tunnel environments are performed in chapter 7.

The measurement setup and procedure are described in section 6.1. This is followed by the comparison of measurements and simulations in various configurations. In section 6.2, a straight concrete tube with and without a vehicle present is considered. In section 6.3, the modelling approach is validated in a curved stoneware tube. Finally, an entire model tunnel, including a straight and a curved stoneware section with a concrete road line is examined in section 6.4.

6.1 Measurement setup and procedure

The measurement setup is shown in Fig. 6.1, with the model tunnel investigated in section 6.4 as device under test (DUT).

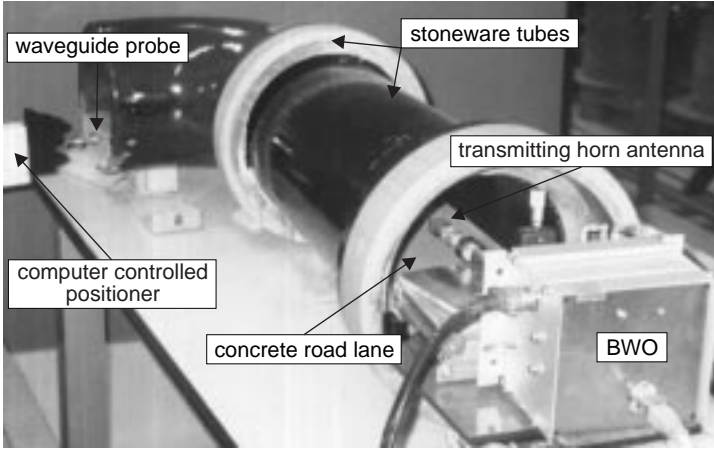


Figure 6.1: Measurement setup with scaled model tunnel; straight and curved stoneware tube with $\varepsilon_r \approx 8$, diameter: 20cm, total length: 107cm, concrete road lane with $\varepsilon_r \approx 5$, transmitter: D-band horn antenna at tunnel entrance, receiver: D-band waveguide probe for 2D-scans at tunnel exit (resolution: $2\text{mm} \times 2\text{mm}$), $f = 120\text{GHz}$

A standard gain pyramidal D-band (110GHz–170GHz) horn antenna is used as transmitter at $f = 120\text{GHz}$. The input power of the antenna $P_T \approx 10\text{dBm}$ is generated by a backward wave oscillator (BWO). The receiver is a D-band rectangular waveguide probe, which can be displaced computer controlled to generate two-dimensional (2D) scans with a resolution of $2\text{mm} \times 2\text{mm}$. The received power level is measured with a vector network analyzer (VNA). The measurement equipment was developed at the *Institut für Hochleistungsimpuls- und Mikrowellentechnik, Forschungszentrum Karlsruhe*, Germany [Arn97, Sch99]. To avoid noticeable side effects by the edges of the tubes, the transmitter as well as the waveguide probe are positioned at least 1cm inside the tubes. The directional patterns of the horn antenna and the waveguide probe are plotted in appendix D and are considered in the simulations.

Various sewer tubes of different kind and shape are used to build the model tunnels. The following tubes are utilized in the comparison:

1. a straight concrete tube with length of 1m and diameter of 20cm,

2. a bent stoneware tube with angle of curvature of 45° , length of 30cm and diameter of 20cm (DN 200 45°),
3. a bent stoneware tube with angle of curvature of 90° , length of 47cm and diameter of 20cm (DN 200 90°),
4. a straight stoneware tube with length of 60cm and diameter of 20cm.

The allowable tolerances for this type of sewer tubes are given in [DIN99], e.g. the curvature may vary up to $\pm 5^\circ$. The material parameters of the tubes have been determined at 200MHz–40GHz via measurements of reflection coefficients with a HP 8510 VNA (assuming that $\mu_r = 1$). The averaged permittivity values are used in the simulations at 120GHz. They are $\epsilon_r \approx 5$ for the concrete tube [SM⁺96] and $\epsilon_r \approx 8$ for the stoneware tubes. Various simulations suggested that the influence of the permittivity—even on the order of 50% variation—is of minor importance compared to the influence of geometrical parameters (cf. section 6.3), which coincides with results obtained in the literature [Mar92, Kle93, MLD94]. The surface roughness of the concrete tube is $\sigma_h \leq 0.1\text{mm}$. The roughness of the stained stoneware tubes is $\sigma_h \leq 0.05\text{mm}$ and thus negligible according to (2.29).

The frequency of $f = 120\text{GHz}$ in the scaled geometry is comparable to a frequency of 1GHz–3GHz in real tunnels. However, in contrast to scaled measurements¹ [JM84, YAS89, Kle93, KSB93], i.e. using the values measured at high frequency in a scaled geometry corresponding to a lower frequency in the unscaled geometry, the measurements and calculations in this chapter are both performed at $f = 120\text{GHz}$.

Despite the tolerances in the geometry of the different tubes and the extremely small wavelengths ($\lambda = 2.5\text{mm}$) a coherent analysis is chosen for comparison purposes in the following sections. The measured and simulated power levels are normalized to their respective maximum values. The agreement of the absolute values is confirmed by an initial free-space measurement.

To quantify the agreement between simulations and measurements, the standard deviation σ_M and the 2D correlation coefficient ρ_M of both results are calculated. In order to avoid large degradations of these values due to possible misalignment of the images, the images are shifted by a maximum of ± 3 pixels in each direction, performing a maximum search with regard to the correlation coefficient prior to the determination of σ_M and ρ_M . This technique is adopted from image processing [DH73, Jäh97]. Additionally, the results are processed by a 2D mean filter with rectangular transfer function of size 3×3 pixels resulting in a second set of “smoothed” $\sigma_{\bar{M}}$ and $\rho_{\bar{M}}$. A sufficient correlation

¹For scaled measurements, one has to ensure a correct scaling of the equivalent conductivity of the building materials, otherwise leading to false imaginary parts of ϵ_r (2.4) [Kle93].

between images is given for $\rho_{M, \bar{M}} > 0.5$, although strongly dependent on the image content.

6.2 Comparisons in a straight concrete tube

First, the straight concrete tube of Fig. 6.2 is examined.

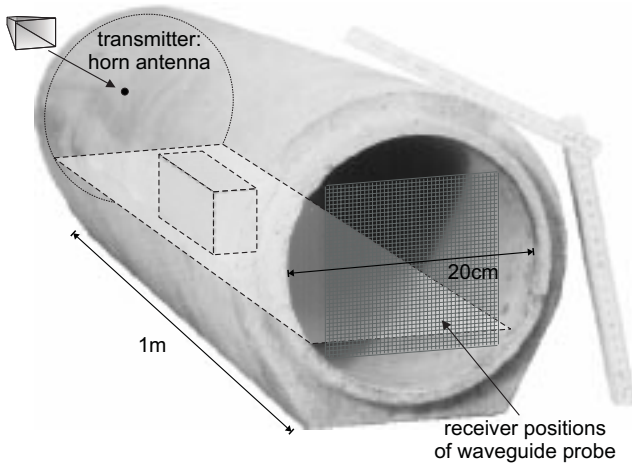


Figure 6.2: Measurement setup with a concrete tube; diameter: 20cm, length: 1m, $\epsilon_r \approx 5$, transmitter: horn antenna at tunnel entrance, receiver: waveguide probe for 2D cross-sectional scans at tunnel exit (resolution: $2\text{mm} \times 2\text{mm}$), $f = 120\text{GHz}$

Figure 6.3 shows the measured and simulated power level distribution (coherent analysis, vv -polarization) at the end of the tube for an eccentric transmitter position 5cm above the center at the tunnel entrance. The measurement and the simulation results agree very well. Only in the lower regions of the figures small discrepancies occur, which may be due to a small misalignment of the antennas. The standard deviation between the measurement and the calculation is $\sigma_M = 4.0\text{dB}$, the correlation between the two images is $\rho_M = 0.68$. The values after mean filtering are $\sigma_{\bar{M}} = 2.3\text{dB}$, $\rho_{\bar{M}} = 0.82$.

For simulation work $5 \cdot 10^7$ rays were traced with up to 10 reflections. One single reception plane was used and scattering was taken into account by the modified reflection coefficients according to (2.30). The simulation time was approximately three hours on the HP workstation, described in Table 5.1.

Then, a configuration with a road lane made of PVC ($\epsilon_r \approx 2.5$) and a matchbox car (“London Sightseeing Bus”) is used. The thickness of the lane is

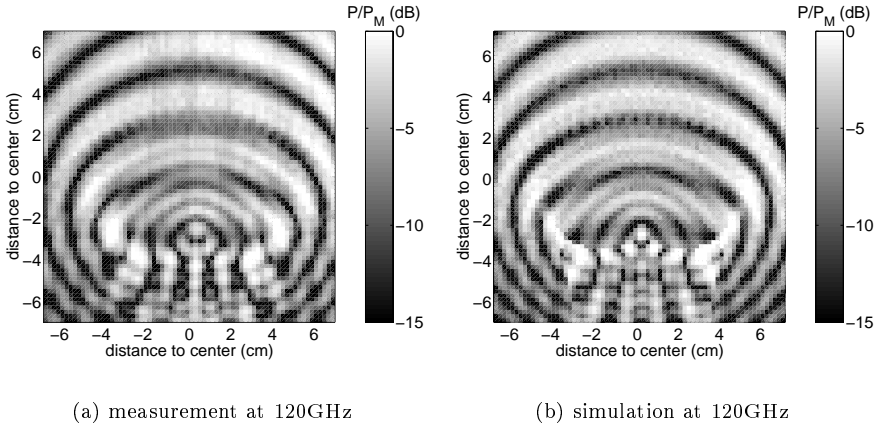
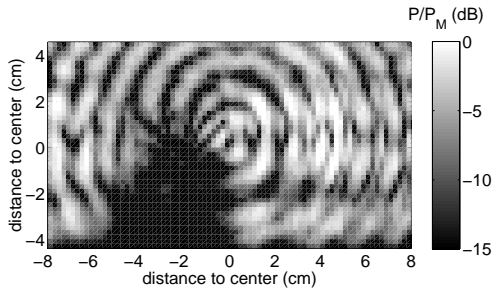


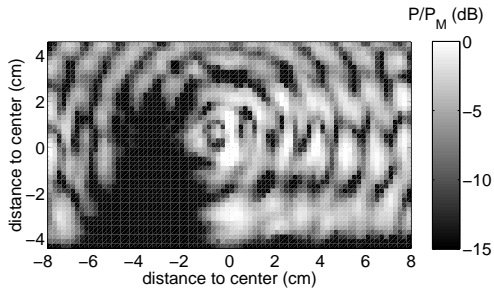
Figure 6.3: Results for measurement setup according to Fig. 6.2, transmitter 5cm above center, scanned area: 71×71 points, resolution: 2mm (coherent analysis, vv -polarization)

approximately 1cm. The vehicle resembles a rectangular box (length: 11.7cm, width: 3.6cm, height: 6.4cm, distance between lane and underbody of the car: 0.3cm) with various windows, whose dimensions are on the order of several wavelengths. The matchbox car is positioned inside the tunnel, 5cm from the tunnel exit, such that a distinct shadow is visible in the analysis. Although the vehicle is only modelled as a floating PEC rectangular box (cf. section 4.4), the measurement (Fig. 6.4(a)) and the simulation (Fig. 6.4(c)) are similar. Additionally, the same scenario has been re-measured with a metallic rectangular box instead of the matchbox car (Fig. 6.4(b)). The outline of the measured box is obviously larger than the one of the matchbox car and therefore closer to the result obtained by the simulation. In all figures the circular structures coincide, as well as the horizontal stripes of high (respectively low) reception levels. Also the boundary condition for grazing incidence is visible at the surface of the lane, which calls for a minimum of the received power level.

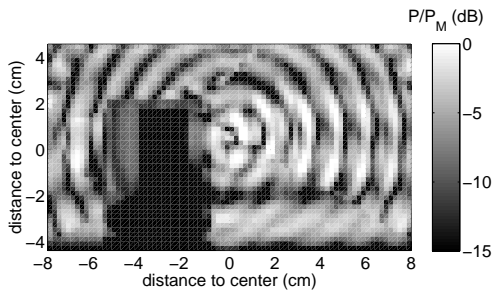
The standard deviation and correlation between the measurement with the matchbox car and the simulation is $\sigma_M = 11.0\text{dB}$ ($\sigma_{\bar{M}} = 9.7\text{dB}$) and $\rho_M = 0.7$ ($\rho_{\bar{M}} = 0.81$), respectively. For the measurement with the metallic box, the corresponding values are $\sigma_M = 10.1\text{dB}$ and $\rho_M = 0.78$ ($\sigma_{\bar{M}} = 8.8\text{dB}$, $\rho_{\bar{M}} = 0.86$). If only the right halves of the pictures in Fig. 6.4 are considered, i.e. if the shadow region of the obstructing object is neglected in the quantitative



(a) measurement: "London Sightseeing Bus"



(b) measurement: metallic rectangular box



(c) simulation (PEC rectangular box)

Figure 6.4: Results for measurement setup according to Fig. 6.2 with PVC-floor ($\epsilon_r \approx 2.5$) and box-like vehicle or metallic rectangular box, centric transmitter position, scanned area: 81×46 points, resolution: 2mm (coherent analysis, vv -polarization)

comparison, the values are $\sigma_M = 4.1\text{dB}$ ($\sigma_{\bar{M}} = 2.7\text{dB}$), $\rho_M = 0.58$ ($\rho_{\bar{M}} = 0.65$) for the matchbox car and $\sigma_M = 5.2\text{dB}$ ($\sigma_{\bar{M}} = 3.5\text{dB}$), $\rho_M = 0.4$ ($\rho_{\bar{M}} = 0.47$) for the metallic box, respectively. The simulation time was about 5.5 hours on a HP workstation with $1 \cdot 10^8$ rays.

6.3 Comparisons in a bent stoneware tube

The measurements in the previous section show a very good agreement with the simulations in a straight tube of circular or arched cross section. To validate the modelling in real 3D curvature, a bent stoneware tube depicted in Fig. 6.5 is used as the device under test in this section.

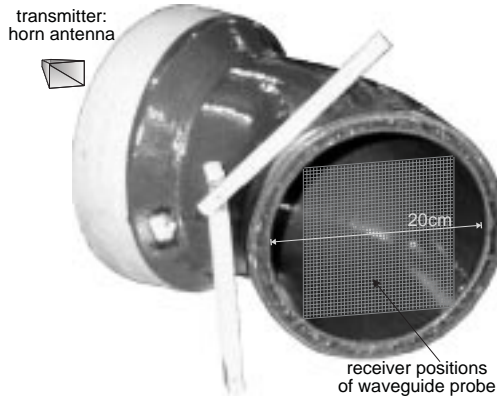


Figure 6.5: Measurement setup with a bent stoneware tube; angle of curvature: 45° , diameter: 20cm, length: 30cm, $\epsilon_r \approx 8$, transmitter: horn antenna at tunnel entrance, receiver: waveguide probe for 2D cross-sectional scans at tunnel exit (resolution: $2\text{mm} \times 2\text{mm}$), $f = 120\text{GHz}$

Figure 6.6(a) shows a schematic plot of the longitudinal profile of such a tube. A closer inspection reveals that the tube is actually constituted by two short straight sections and an intermediate (generally non-circular) bend. For the modelling, the curvature is approximated by a circular arc, resulting in the geometry plotted in Fig. 6.6(b).

In order to validate the performance of the modelling, and—at the same time—to examine the influence of 3D curvature on the propagation properties, the bent tube of Fig. 6.5 has been measured and compared with three different simulation setups:

1. a straight tube with the same length and diameter as the actual probe,

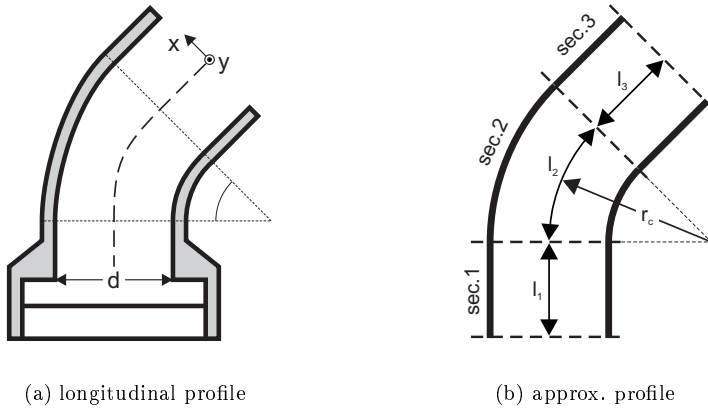


Figure 6.6: (a) Schematic plot of the longitudinal profile of a bent stoneware tube with corresponding approximative tri-sectional geometry used in the simulation (b)

2. a tube constituted by one single circular arc, having the same angle of curvature (45°), the same length and the same diameter as the actual probe ($d = 20\text{cm}$),
3. a bent stoneware tube modelled according to Fig. 6.6(b), with a first straight section of length $l_1 = 7.5\text{cm}$, a second curved section of length $l_2 = 14.85\text{cm}$, a radius of curvature $r_c = 18.91\text{cm}$, and a third straight section of length $l_3 = l_1 = 7.5\text{cm}$.

The transmitter is situated at the entrance of the tube in an eccentric position 5cm from the center in direction of the bend. Figure 6.7 depicts the measurement and the simulations at the other end of the model tunnel. Although the actual geometry of the bent stoneware tube is only roughly approximated by the tri-sectional geometry of Fig. 6.6(b), the measurement in Fig. 6.7(a) and the simulation in Fig. 6.7(b) suggest a good agreement over a large area. The effects of the relatively strong bend can be identified by comparing the images with the results obtained for the pure (and therefore less distinct) bend in Fig. 6.7(c), and for the equivalent straight tube in Fig. 6.7(d). The correlations and the standard deviations between the measurement and the calculations are given in Table 6.1. In addition to the comparison of the entire images, the values are also determined for the portions of the images containing the most distinct parts of the interference patterns, extending from $[-2\text{cm}, 6.5\text{cm}]$ over the x -axis, and from $[-4\text{cm}, 4\text{cm}]$ over the y -axis (the axes' orientations

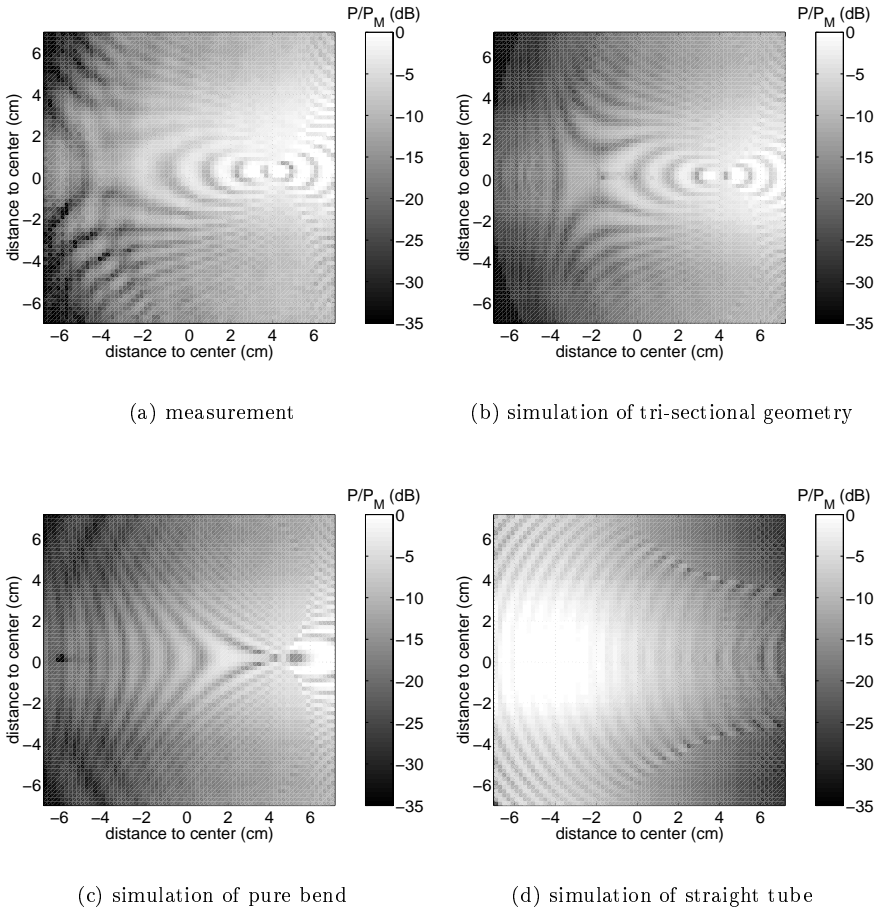
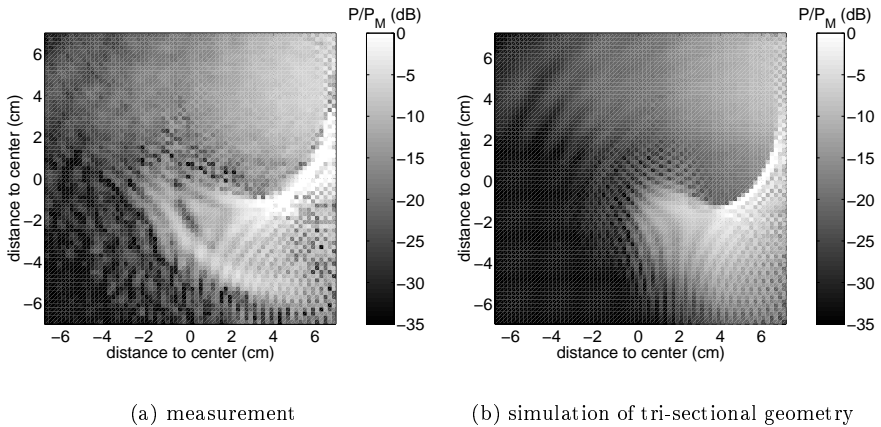


Figure 6.7: Results for measurement setup according to Fig. 6.5, transmitter in eccentric position 5cm from the center in the direction of the bend, scanned area: 71×71 points, resolution: 2mm (coherent analysis, vv -polarization)

are depicted in Fig. 6.6(a)). It is apparent from the figures that the actual shape (i.e. the course) of the simulated tunnels is of major importance. The differences between the straight tube, the pure bend, and the tri-sectional geometry are significant. The comparison between the measurement in the bent tube and the simulation of the straight section even leads to a negative correlation. Thus, a precise modelling of the tunnel's geometry including curvature is

Table 6.1: Correlations and standard deviations between the measurement and the simulations of Fig. 6.7 together with computation times of the simulations

entire images:			
	straight section (Fig. 6.7(d))	pure bend (Fig. 6.7(c))	tri-sectional bend (Fig. 6.7(b))
$\rho_M(\rho_{\bar{M}})$	-0.4 (-0.43)	0.89 (0.94)	0.91 (0.95)
$\sigma_M(\sigma_{\bar{M}})$	11.9dB (11.7dB)	3.3dB (2.5dB)	3.0dB (2.2dB)
parts of the images ($x \in [-2\text{cm}, 6.5\text{cm}]$, $y \in [-4\text{cm}, 4\text{cm}]$):			
	straight section	pure bend	tri-sectional bend
$\rho_M(\rho_{\bar{M}})$	-0.33 (-0.39)	0.68 (0.8)	0.74 (0.88)
$\sigma_M(\sigma_{\bar{M}})$	7.7dB (7.4dB)	3.4dB (2.3dB)	2.5dB (1.6dB)
simulation times			
	straight section	pure bend	tri-sectional bend
t	1:04h	1:10h	1:20h

Figure 6.8: Results for measurement setup according to Fig. 6.5, transmitter 5cm above center, scanned area: 71×71 points, resolution: 2mm (coherent analysis, vv -polarization)

mandatory to predict the results with sufficient accuracy. For all simulations, $5 \cdot 10^7$ rays have been launched and up to 20 reflections have been considered.

The simulation times are given in Table 6.1.

The results are also very sensitive to the location of the transmitter, in addition to the geometry of the tube. In Fig. 6.8 simulations and measurements are compared with a different transmitter position being situated 5cm above the center of the bent tube. Apart from that the same scenario as for the previous figures is assumed. The measured (Fig. 6.8(a)) and the simulated (Fig. 6.8(b)) power distribution differ significantly from the ones obtained in Figs. 6.7(a) and 6.7(b). The agreement between the measurement and the simulation is very encouraging, with $\sigma_M = 4.9\text{dB}$, $\sigma_{\bar{M}} = 3.2\text{dB}$, $\rho_M = 0.89$, and $\rho_{\bar{M}} = 0.96$. Again, $5 \cdot 10^7$ rays have been launched, resulting in a simulation time of 1:20h.

6.4 Comparisons in a model tunnel built of straight and curved sections

After the analyses of single pieces of tubes, two stoneware tubes are combined to build an entire model tunnel. The model tunnel consists of a straight section of length $l_s = 60\text{cm}$ and a 90° -bend of length $l_b = 47\text{cm}$, resulting in a total length of $l_t = 107\text{cm}$. Due to the tolerances in the geometry of the two tubes, the transition from the straight to the curved tube is not homogeneous, but leaves a gap of approximately 0.5cm width. Furthermore a concrete road lane is cemented into the tunnel up to a height of 5.5cm above the lowest point of the tubes. Figure 6.1 shows the measurement setup with the entire model tunnel.

The aim of the measurements in the model tunnel is in analogy to the previous sections to validate the RDN-based modelling approach. Moreover, the focusing of energy introduced by a concave curvature is investigated. For this purpose, horizontal scans into the tunnel rather than scans over the cross section of the tunnel are carried out. The geometry for this type of analysis is depicted in Fig. 6.9.

The first horizontal scan is performed before the concrete road lane is put into the model tunnel. The transmitter is situated in a centric position, the scan is taken 10cm above the lowest point of the (still circular) cross section. After the inclusion of the road lane, a second horizontal scan is measured at the same position (i.e. 4.5cm above the road), with the transmitter 9.5cm above the road at the tunnel entrance. Figure 6.10 shows the two measured (Figs. 6.10(a), 6.10(b)) together with the corresponding predicted results (Figs. 6.10(c), 6.10(d)).

For the simulations the bent tube is, according to the previous section, approximated by a tri-sectional geometry, i.e. a first straight section with $l_1 =$

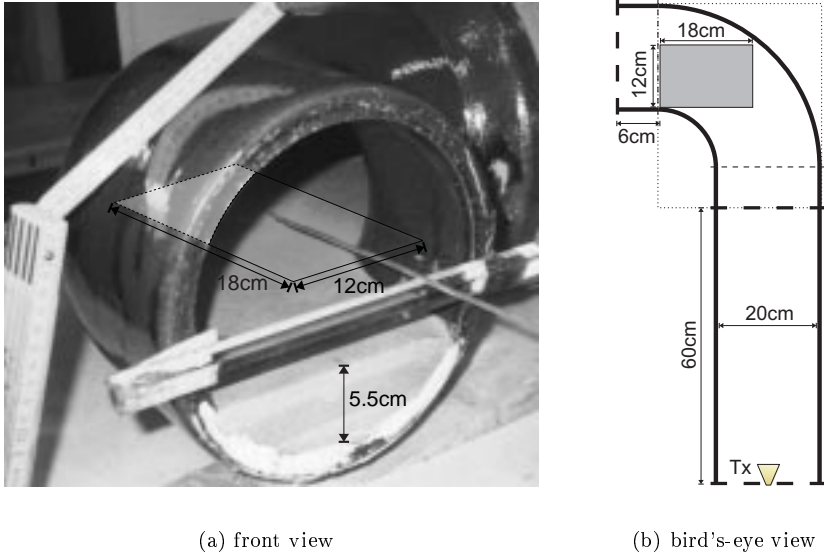


Figure 6.9: Measurement setup for horizontal scan in the scaled model tunnel of Fig. 6.1, height of concrete road lane: 5.5cm, scanned area 4.5cm above road lane, 18cm \times 12cm at 6cm from the tunnel exit (resolution: 2mm \times 2mm), $f = 120\text{GHz}$

5.5cm, a second curved section with $l_2 = 36.1\text{cm}$ and $r_c = 21.8\text{cm}$, and a third straight section with $l_3 = l_1 = 5.5\text{cm}$. The utilized permittivities are $\epsilon_r = 8$ for the stoneware tubes and $\epsilon_r = 5$ for the concrete road lane. The roughness of the surfaces is $\sigma_h < 0.05\text{mm}$, which is negligible. A horizontal reception plane is used in the simulation. A significant part of the launched rays is intersecting the horizontal reception plane near grazing incidence. Therefore, the number of rays has to be significantly large to ensure a sufficient convergence compared to a cross-sectional analysis (cf. section 4.5). For the results shown in Figs. 6.10(c) and 6.10(d), $5 \cdot 10^8$ rays have been launched and up to 20 reflections were traced. The computation time was about 4 days.

Bearing in mind that the real geometry of the model tunnel cannot be constructed perfectly in the simulation (especially the gap on the order of two wavelengths and the geometry of the bend), the measurements and the simulations in Fig. 6.10 agree surprisingly well. The standard deviations and the correlations between the measurements and the simulations are calculated for the right halves of the images, containing the most distinct parts of the inter-

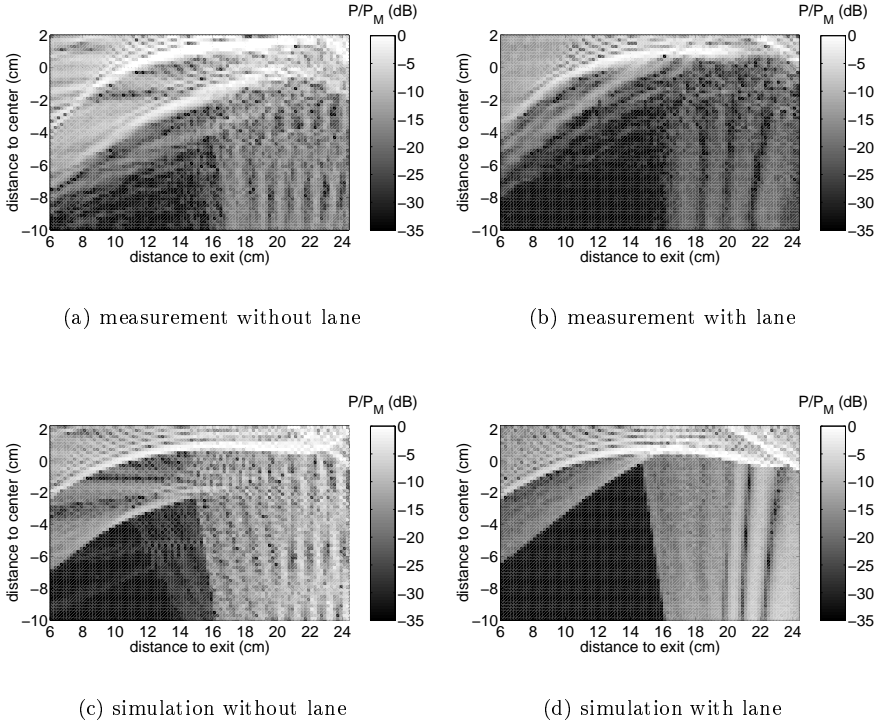
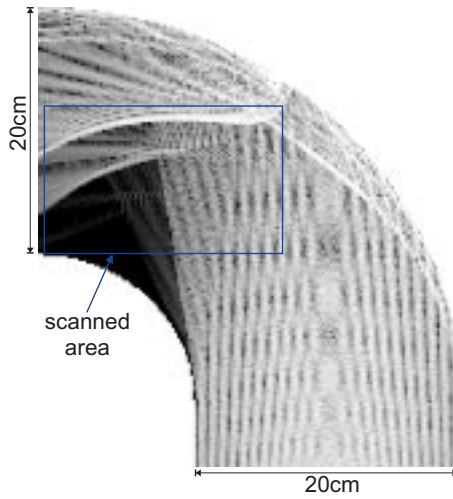


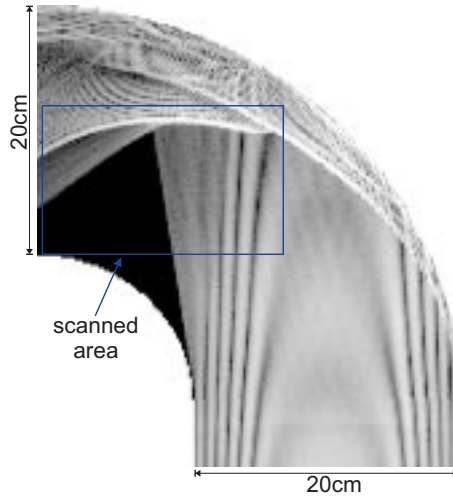
Figure 6.10: Results for the scenario of Fig. 6.1, measurement setup according to Fig. 6.9, scanned horizontal area: 92×60 points, resolution: 2mm (coherent analysis, vv -polarization)

ference patterns². The values are $\sigma_M = 7.8\text{dB}$ ($\sigma_{\bar{M}} = 5.5\text{dB}$) and $\rho_M = 0.33$ ($\rho_{\bar{M}} = 0.53$) for the tunnel without road lane, and $\sigma_M = 6.7\text{dB}$ ($\sigma_{\bar{M}} = 4.9\text{dB}$) and $\rho_M = 0.5$ ($\rho_{\bar{M}} = 0.63$) for the tunnel with road lane. In the upper parts of the images, the focusing effect of the bend becomes clearly visible by the light “stripes” (focal lines) indicating a high level of received power. Thus, for the first time, the RDN-based ray-optical modelling approach enables a precise prediction of electromagnetic wave propagation in curved tunnels including the focusing of energy, without the problems of traditional GO solutions in the vicinity of caustics. Figure 6.11 depicts the same simulations but over the

²Otherwise the strong influence of the shadow regions, indicated by the dark areas in the lower left corners of the images, would dominate the determination of the correlation.



(a) simulation without road lane



(b) simulation with road lane

Figure 6.11: Horizontal analysis in the curved section of the model tunnel (dotted rectangle in Fig. 6.9(b)), resolution: $2\text{mm} \times 2\text{mm}$ (coherent analysis, vv -polarization)

whole bent area of the model tunnel. It is seen that the transitions from the straight to the curved section can be clearly distinguished and the influence of the road lane is pronounced.

6.5 Summary

In this chapter, the proposed ray density normalization (RDN) was verified by measurements in scaled model tunnels at 120GHz. In particular the performance in real 3D curvature was investigated and validated. The various qualitative and quantitative comparisons identify the RDN as a very powerful approach. All relevant effects in straight tunnels, curved tunnels, and tunnels with vehicles are predicted with sufficient accuracy when compared to measurements.

After the theoretical validation in chapter 5 and the validation by measurements under “laboratory-like” conditions, the next chapter deals with the ability of the technique to cope with “real life” scenarios. For this purpose, measurements in the Berlin subway have been performed.

Chapter 7

Scenarios and applications

In the previous two chapters, the practicality of the proposed ray density normalization (RDN) was proven both theoretically and experimentally by measurements in scaled model tunnels of different shapes. In this chapter, the application of the RDN in real tunnels, which are mostly of non-idealized geometry, is investigated. For this purpose, a measurement campaign has been carried out in the Berlin subway. Further to verify the modelling approach, the behaviour of electromagnetic wave propagation in different scenarios and its sensitivity to parameter changes are investigated. Moreover, the effects of exterior transmitting antenna locations and the influence of curves on the power distribution inside the tunnels are determined, and the ability of the modelling approach to estimate broadband channel parameters is pointed out.

Section 7.1 is devoted to the measurements and comparisons in the Berlin subway. First, the measurement setup and the different tunnels are described (section 7.1.1). Second, the measurements are compared with simulations in section 7.1.2, together with several analyses of the influence of the geometry on the prediction accuracy and on the power distribution in curved tunnels. Scenarios with different antenna positions in front of a tunnel's entrance are examined in section 7.2. Finally, the impact of moving vehicles on the delay and Doppler spread is shown in section 7.3.

7.1 The Berlin subway

In order to characterize wave propagation in underground railroad tunnels in the GSM900 and GSM1800 frequency bands, a measurement campaign was carried out in the Berlin subway. The propagation scenario of subway tunnels is by far less homogeneous than the idealized geometries of the model tunnels in

the previous chapter. Hence, this environment can be seen as “worst-case” scenario to test the applicability and performance of the modelling approach. Two tunnels of different shape, length, and building materials are investigated. Furthermore, different transmitting antenna positions are analysed. The received power levels at 945MHz and 1853.4MHz are used to evaluate the attenuation and the fading characteristics of the different constellations and environments.

7.1.1 Measurement setup and procedure

7.1.1.1 Measurement equipment

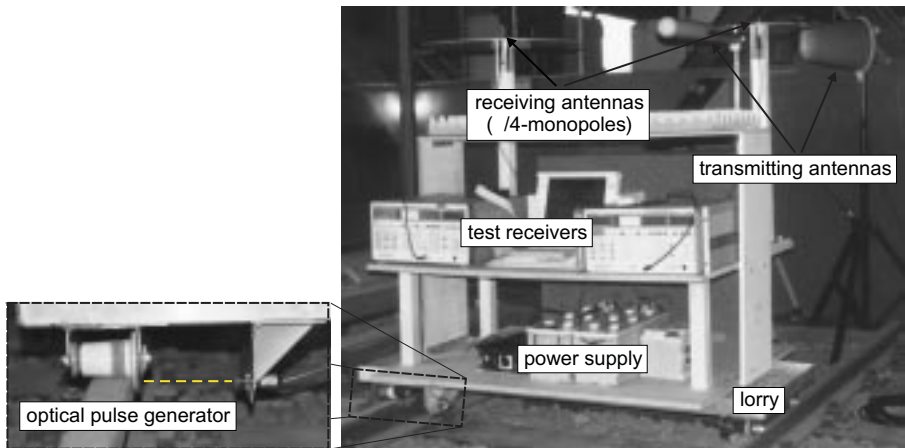


Figure 7.1: Measurement setup with transmitting antennas and receiving equipment mounted on a lorry with an optical pulse generator

The measurements were performed using a Ballmann STX-GSM 2 GSM900 test transmitter, a Rhode&Schwarz SME 23 GSM1800 test transmitter, and two Rhode&Schwarz extended test receivers ESVD for digital mobile radio networks. The transmitters generated two harmonic signals at $f_{GSM} = 945\text{MHz}$ and $f_{DCS} = 1853.4\text{MHz}$, respectively. The intermediate frequency (IF) measurement bandwidth was 10kHz. For the GSM900 band, a log-periodic (LogPer), vertically polarized transmitting antenna with 12dBi gain was used (Kathrein K73226), whereas for the GSM1800 band, a wide-band Yagi antenna with 17dBi gain (Jaybeam J7360) was employed [Bal97, chapter 10]. Both are standard antennas for the deployment in tunnel environments. As receiving antennas, two $\lambda/4$ -monopoles were chosen due to their omnidirectional antenna patterns. The patterns of the transmitting antennas and the

monopoles are given in appendix D. The battery-driven receivers were mounted on a lorry which was manually pulled through the tunnels at an average speed of 1.5m/s. The measurements were recorded approximately every 30cm, where each measured value corresponds to the averaged received signal during a 10ms time interval. The actual measurement location was retrieved with a pulse-generator coupled to the wheels of the lorry (cf. Fig. 7.1). Each measurement was run and recorded twice in order to determine the time variance of the transmission channel. Furthermore, the two corresponding measurements were compared and aligned to each other to ensure a reasonable precision in the absolute location of the measured values. This was necessary due to the imprecise performance of the pulse generator, which provided an impulse approximately every 17.9cm with a precision of $\pm 0.5\text{cm}$. The positions of the transmitting antennas were varied for each measurement. The receiving monopoles were fixed on the lorry at a height of $h_R = 1.47\text{m}$ above the rails.

The measured path loss has been deduced from the ratio of the measured received power to the input power of the transmitting antennas, including the antennas characteristics. The attenuation of the connecting cables was taken into account, and an additional 1.5dB loss was assumed for any kind of mismatch in both the receiving and transmitting branches. The simulated path loss obtained by (2.54), normalized to P_T , also includes the antenna characteristics.

7.1.1.2 Measurement environment

Two different tunnels are investigated:

1. a short straight rectangular, wide-profile, single-lane tunnel section (part of subway U5 between “Friedrichsfelde” and “Tierpark”), built in the early 70’s,
2. a curved arched, single-lane tunnel (subway U8 between “Karl-Bonhoeffer-Nervenklinik” and “Rathaus Reinickendorf”), built in the late 80’s.

The width of the rectangular tunnel section is $w_{U5} \approx 3.8\text{m}$, its height $h_{U5} \approx 4.3\text{m}$, and its length $l_{U5} \approx 110\text{m}$. The main building material is reinforced concrete, the side walls are covered by a variety of cables (e.g. power supply- and phone-lines) and mountings. The rail sleepers lie on gravel. The roughness of the walls was estimated to $\sigma_h = 2\text{cm}$, the roughness of the floor to $\sigma_h = 5\text{cm}$.

The cross section of the arched tunnel is constituted by a circular shape of radius $r_{cs} \approx 2.9\text{m}$ with an elevated floor 1.2m above the lowest point of the circle (cf. Fig. 7.3). A schematic plot of the tunnel’s course is shown in Fig. 7.2. It consists of nine different sections and can roughly be described by a first straight part, followed by a left bend with large radius of curvature and a right bend with smaller radius of curvature. For simulation work, the

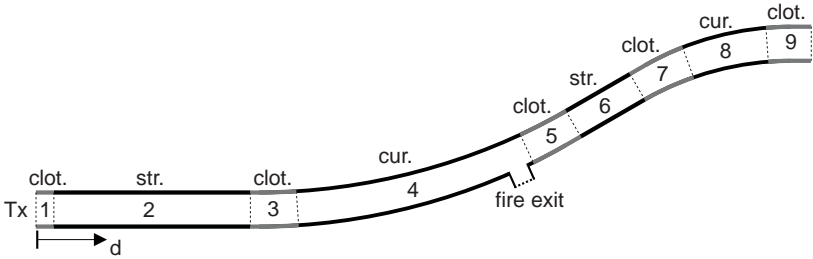


Figure 7.2: Schematic course plot of the arched shaped tunnel (U8), with a total length of $l_{U8} \approx 1079\text{m}$



Figure 7.3: View into the arched shaped tunnel (U8) of Fig. 7.2 from “Karl-Bonhoeffer-Nervenklinik” ($d = 0\text{m}$)

nine sections are modelled according to section 4.1. The total length of the tunnel is $l_{U8} \approx 1079\text{m}$, the maximum measured distance is $d \approx 1000\text{m}$. At distances $d > 420\text{m}$ from the transmitter, the receiver and the transmitter have no longer a direct line-of-sight (LOS). At distance $d_{\text{exit}} = 620\text{m}$ from the transmitter, an open connection (fire exit) exists for security reasons between the actual and the second tube, which runs in parallel, extending over an area of approximately 25m^2 (cf. Fig. 7.2). Figure 7.3 depicts the view into the tunnel from the station “Karl-Bonhoeffer-Nervenklinik”, with the transmitters situated at the beginning of the tube.

It is apparent from Fig. 7.3, that the walls are not smooth but that they have a periodic structure due to the special construction by screwed prefabricated elements. Consequently, the occurring (large scale) height variations of the tunnel walls are not resulting from a statistically rough surface in a strict sense, but rather from a periodically rough surface¹. Nevertheless, the concept of rough surface scattering can be applied in an approximate way by adapting the mean roughness of the walls with growing distances: at small distances from the transmitter, where most rays impinge under oblique incidence (i.e. with small incident angles) onto the walls, a mean roughness of $\sigma_h = 2\text{cm}$ is assumed. At larger distances, where most rays impinge under near grazing incidence onto the walls, the mean roughness—and thus the attenuation—is increased (up to $\sigma_h = 15\text{cm}$), to reflect the shadowing behaviour of the special wall structure.

For both tunnels, the parameters of the building materials in the simulation correspond to dry concrete ($\epsilon_r = 5 - j 0.1$). The roughness of the walls is taken into account by the modified Fresnel reflection coefficients.

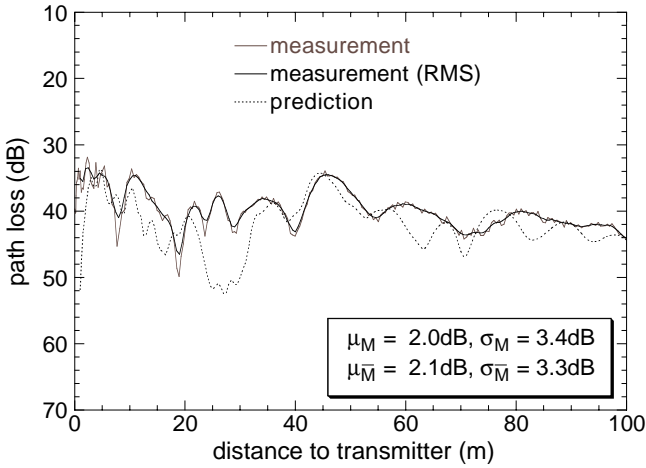
7.1.2 Results

In both tunnels, several transmitting antenna constellations were measured at the two frequencies. First, the short straight tunnel section (U5) is considered. In this rectangular geometry, image theory, as a ray-optical reference solution, can be used to determine the achievable accuracy by simulations. Thereafter, the measurements in the curved tunnel with arched cross section (U8) are used in exemplary analyses.

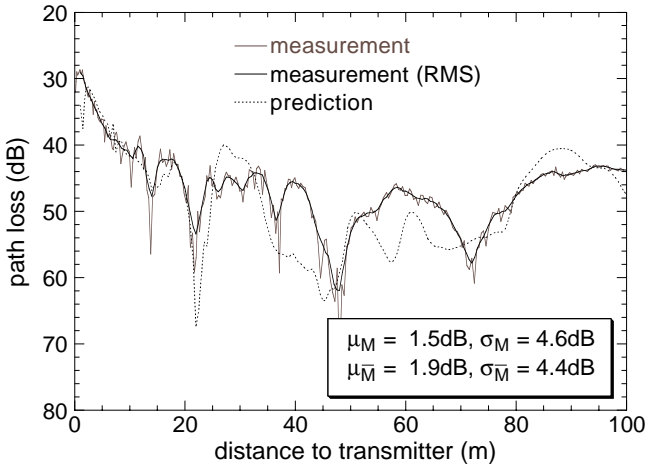
7.1.2.1 Achievable accuracy in the rectangular straight tunnel (U5)

Figure 7.4 depicts the measured and predicted path loss in the straight rectangular tunnel (U5) for two different constellations. For Fig. 7.4(a), the transmitting GSM900 antenna was situated at a height of $h_T = 2.82\text{m}$, 0.88m to the left of the tunnel center. For the scenario in Fig. 7.4(b), the transmitting GSM1800 antenna was situated at a height of $h_T = 2.2\text{m}$, 0.04m to the right of the center. The predicted path loss was calculated by image theory at 200 receiver locations for up to 10 reflections per ray. The simulation time was a few minutes on a standard HP workstation. To quantify the agreement of predictions and measurements, mean values μ_M and standard deviations σ_M of the difference (in dB) between the measured and the predicted losses are determined. Like in the previous chapter, the values are either obtained by

¹A periodically rough surface generally results in scattering patterns with specific preferential directions.



(a) GSM900



(b) GSM1800

Figure 7.4: Comparisons of measurements and predictions in the straight rectangular-shaped tunnel section (U5) with different transmitter positions at $f_{GSM} = 945\text{MHz}$ and $f_{DCS} = 1853.4\text{MHz}$, running RMS window length for the measurement: 1m (whereas for the prediction, no RMS generation is performed due to a reception-sphere spacing of 0.5m)

a direct “raw” comparison, indicated by the subscript M , or after a previous running root mean square (RMS) generation (cf. section 7.1.2.5), indicated by the subscript \bar{M} leading to $\mu_{\bar{M}}$ and $\sigma_{\bar{M}}$. The imperfect match of the measurements and predictions confirms the already indicated “worst-case” character of the environment of subway tunnels for propagation modelling. This mismatch is due to the irregular structure of the tunnel, modelled as being straight and rectangular. The mean values and standard deviations obtained in this grossly simplified scenario serve as benchmarks for the following comparisons. In the remainder of this section, the curved tunnel of Figs. 7.2 and 7.3 is examined.

7.1.2.2 Path loss in the curved arched-shaped tunnel (U8)

In the curved arched-shaped tunnel (U8), several transmitter locations were deployed. Figures 7.5 and 7.6 depict the comparisons for the configuration shown in Fig. 7.3.

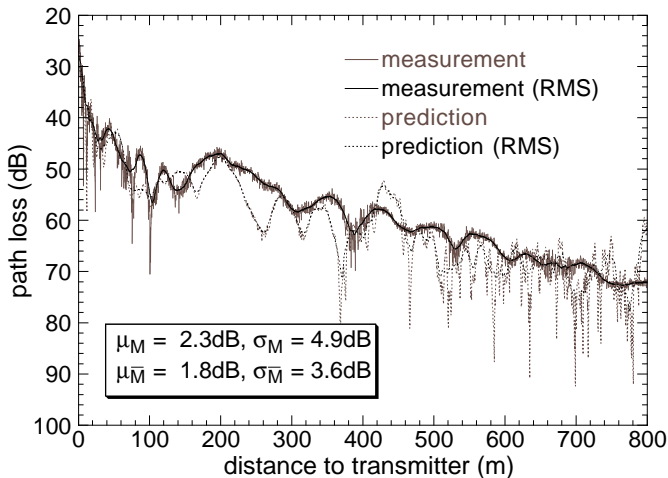


Figure 7.5: Comparison of measurement and simulation in the curved arched-shaped tunnel (U8) at $f_{GSM} = 945\text{MHz}$, running RMS window length: $40\lambda_0$ (right transmitting antenna in Fig. 7.3)

The GSM900 antenna was situated at a height of $h_T = 2.5\text{m}$, 0.98m to the right of the tunnel’s center (right transmitting antenna in Fig. 7.3). The GSM1800 antenna was positioned at $h_T = 2.45\text{m}$, 0.93m to the left of the center (left transmitting antenna in Fig. 7.3). The receiving antennas were aligned accordingly with the GSM900 monopole on the right side and the GSM1800 monopole on the left side of the lorry. The path loss was simulated

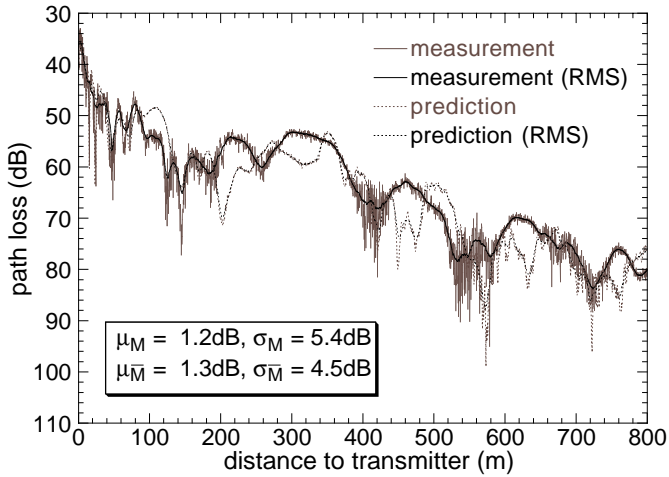


Figure 7.6: Comparison of measurement and simulation in the curved arched-shaped tunnel (U8) at $f_{DCS} = 1853.4\text{MHz}$, running RMS window length: $60\lambda_0$ (left transmitting antenna in Fig. 7.3)

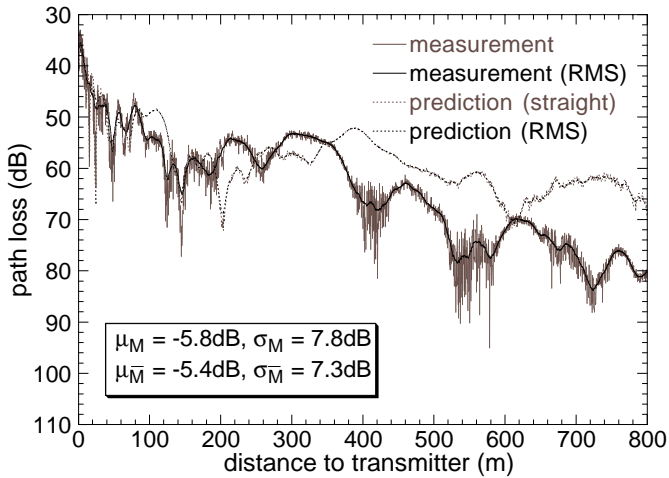


Figure 7.7: Comparison of measurement and simulation of Fig. 7.6, but assuming a fictitious straight tunnel course for the simulation

by the RDN-based power trace method. 150 million rays were traced with up to 40 reflections. The calculation time for the 1600 receivers was about 40h. The good agreement of the measured and the predicted path loss validates the RDN modelling approach. The small mean errors ($\mu_{\bar{M}} = 1.8\text{dB}$ in Fig. 7.5 and $\mu_{\bar{M}} = 1.3\text{dB}$ in Fig. 7.6) and standard deviations ($\sigma_{\bar{M}} = 3.6\text{dB}$ in Fig. 7.5 and $\sigma_{\bar{M}} = 4.5\text{dB}$ in Fig. 7.6) emphasize the good performance of the model, especially bearing in mind the imprecise assignment of the absolute measurement location (cf. section 7.1.1.1).

7.1.2.3 Influence of curves on the simulation accuracy

In order to determine the influence of curves on the propagation behaviour, the same measurements as depicted in Fig. 7.6 (U8 scenario at $f_{DCS} = 1853.4\text{MHz}$) are compared with simulations, where the bend of the tunnel is approximated by a straight line. Compared to the simulation of the actual curved course in Fig. 7.6, one can clearly distinguish the deviation of the prediction from the measurement in Fig. 7.7. For distances $d > 350\text{m}$, the deviation becomes noticeable, which is the region where the left bend of the tunnel starts. Although the radius of curvature of the left bend is as large as $r_{cs} = 850\text{m}$, the deviation is rather significant. The predicted mean level is increased by 7dB and the standard deviation is almost doubled. This example shows the importance of an adequate modelling of a tunnel's curvature, being possible by the proposed novel RDN-based techniques.

7.1.2.4 Influence of the cross-sectional shape on the simulation accuracy

It is commonly assumed that the actual shape of the cross section is of minor influence on the propagation behaviour in a tunnel, as long as its actual cross-sectional area is preserved [YA⁺85, ZH98a]. Figures 7.8, 7.9 and 7.10 show comparisons of the GSM1800 scenario in Fig. 7.3 on the first 100m with different cross-sectional shapes used for the simulations. In addition to the arched cross section (Fig. 7.8), a pure circular cross section with radius $r_{cs} = 2.675\text{m}$ (Fig. 7.9), and a rectangular cross section of width $w = 5.25\text{m}$ and height $h = 4.28\text{m}$ (Fig. 7.10) are applied, all covering the same area. The mean errors and standard deviations are calculated on the first 100m. Again, it turns out that the correct modelling of the tunnel's cross section affects the accuracy of the modelling results significantly.

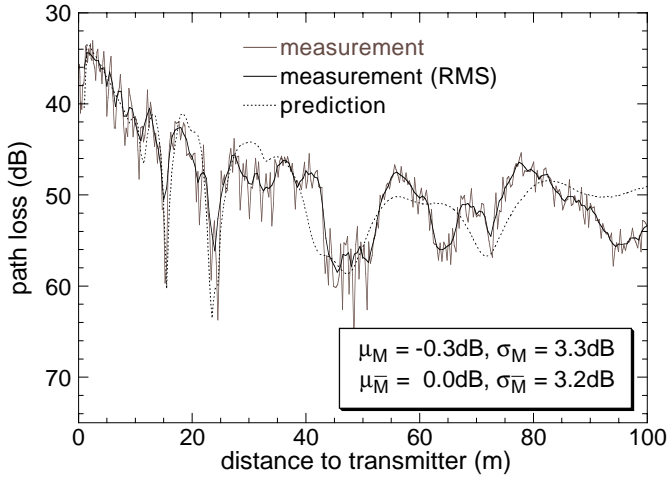


Figure 7.8: Comparison of measurement and simulation with arched cross section, parameters according to Fig. 7.6, $f_{DCS} = 1853.4\text{MHz}$, running RMS window length: 1m (re-plot of Fig. 7.6 on the first 100m)

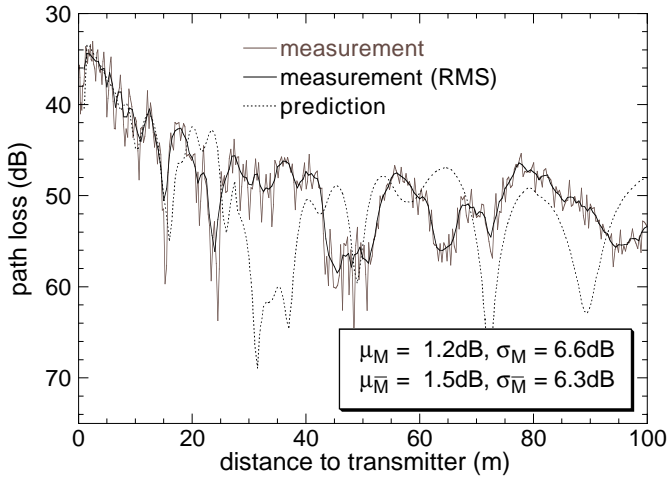


Figure 7.9: Comparison of measurement and simulation with circular cross section, parameters according to Fig. 7.6, $f_{DCS} = 1853.4\text{MHz}$, running RMS window length: 1m

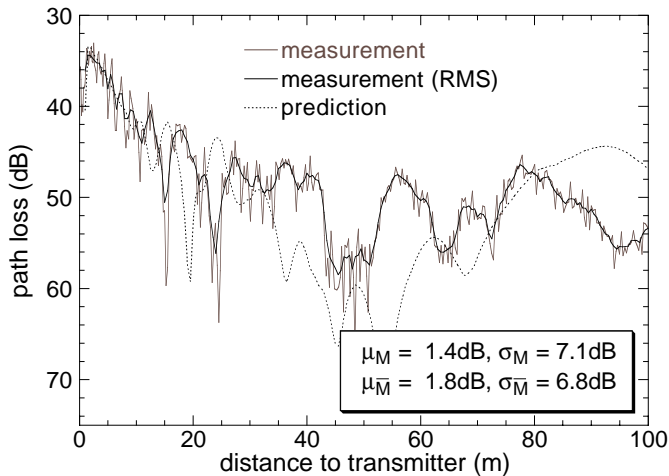


Figure 7.10: Comparison of measurement and simulation with rectangular cross section, parameters according to Fig. 7.6, $f_{DCS} = 1853.4\text{MHz}$, running RMS window length: 1m

7.1.2.5 Fast fading characteristics

An interesting question is, whether the fast fading in a tunnel, i.e. the fluctuation of the received signal on a small-scale basis, can be characterized by a standard probability density function (PDF). The fast fading envelope is obtained by normalizing the received signal to its local root mean square (RMS) value. Generally, a window length of at least 40 wavelengths is chosen for the RMS determination [Lee82, Lee89, Ste92]. The resulting fading envelope is compared to the following classical distribution functions: Gaussian (normal), lognormal, Nakagami, Rayleigh, Rician and Weibull [ITU1057, Lor79, Pap84, Pro89]. In order to determine the parameters of the respective distributions, a least-mean-square (LMS) based parameter fitting can be used [KE95]. The LMS optimization is based on a simplex method [NM65]. As an example, Figs. 7.11 and 7.12 show the results of the LMS optimization for the GSM1800 measurement² of Fig. 7.6.

The best fits for all measurements are achieved using Rician distributions at both frequencies, which is congruent with the literature [LD98]. Nevertheless, except for the Rayleigh distribution, all other densities lead to similar

²Generally, a sampling of at least $\lambda_0/2$ is required for a non-ambiguous fast fading characterization. This requirement is clearly violated by the performed measurements. Nevertheless, for all GSM900 and GSM1800 measurements the obtained fading characteristics led to similar results.

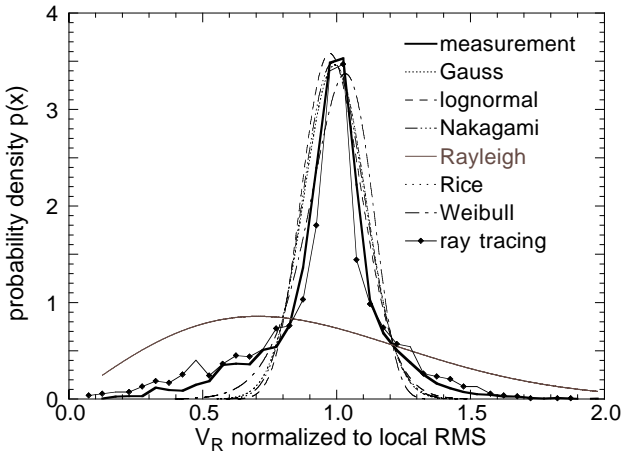


Figure 7.11: Least-mean-square (LMS) best fit probability density functions (PDF) for the measurement of Fig. 7.6, RMS window length: $60\lambda_0$

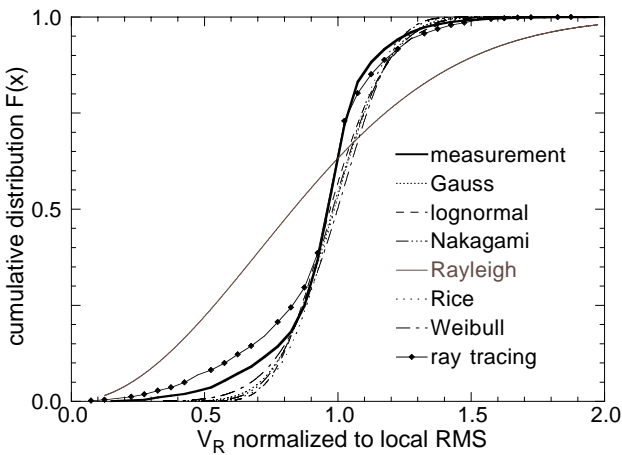


Figure 7.12: Least-mean-square (LMS) best fit cumulative distribution functions (CDF) for the measurement of Fig. 7.6, RMS window length: $60\lambda_0$

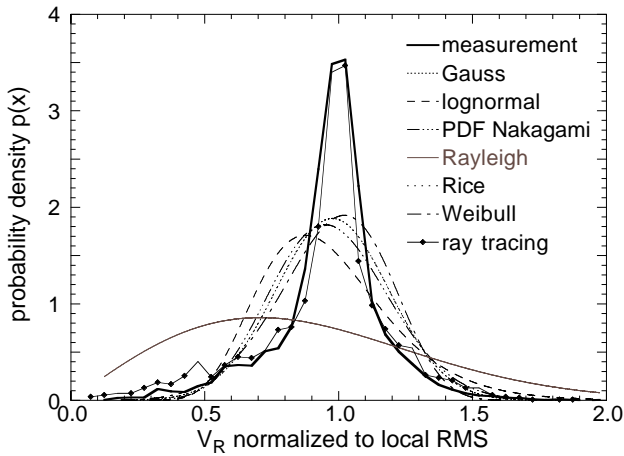


Figure 7.13: Chi-square best fit probability density functions (PDF) for the measurement of Fig. 7.6, RMS window length: $60\lambda_0$

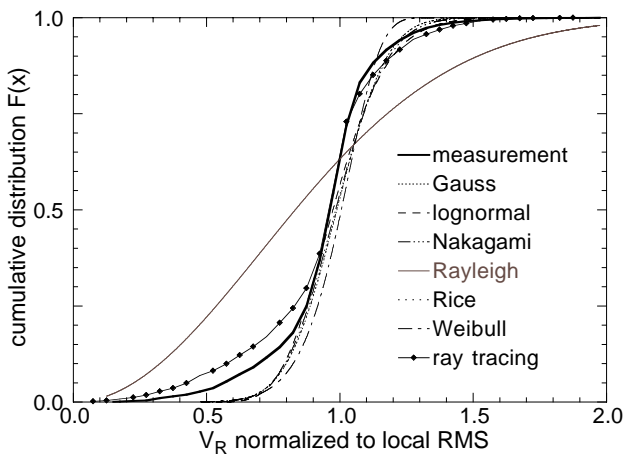


Figure 7.14: Kolmogorov-Smirnov best fit cumulative distribution functions (CDF) for the measurement of Fig. 7.6, RMS window length: $60\lambda_0$

results, as indicated by Figs. 7.11 and 7.12. The interesting area of the curves, however, is in the lower V_R -range corresponding to very low received signal levels, the so-called deep-fades. In this region, none of the curves obtained by the LMS optimization leads to satisfactory results. Another way to determine the parameters of the various densities is given by a recursive application of the chi-square and Kolmogorov-Smirnov goodness-of-fit tests [Pap84, Ste92]. The chi-square test is particularly suited for a fitting in the area of low received values due to its sensitivity in regions of low probability. Figure 7.13 shows the results for the PDF's obtained by a simplex optimization with the chi-square criterion. The fitted curves now approximate the measurement for low received values more closely for the chi-square fitting compared to the LMS fitting (Fig. 7.13 compared to Fig. 7.11). However, an overall match could not be achieved by neither of the analytical densities. Figure 7.14 depicts the cumulative distribution functions (CDF) obtained with the Kolmogorov-Smirnov criterion. Again, no significant improvement can be achieved compared to the LMS fitting in Fig. 7.12. Consequently, a complete characterization of the fast fading characteristics in a tunnel by standard analytical density functions appears to be impossible. In contrast, the PDF and CDF extracted from the prediction in Fig. 7.6 approach the measurement more closely over the entire range of V_R . The corresponding predicted curves are drawn in all figures, marked by black diamonds (and "ray tracing").

7.1.2.6 Distribution of the propagating power in curves

In the previous chapter, focusing of energy due to bends has been observed in the model tunnel by measurements and simulations (cf. section 6.4). In the curved subway tunnel, the opposite effect is noticeable: a rapid decrease of the received power level at the inner side of a curve. The measurement in the GSM900 band plotted in Fig. 7.5 was performed over the total length of the subway tunnel (U8). As already indicated, the transmitting antenna and the receiving monopole were both situated on the right side of the tunnel axis referring to Fig. 7.3. Following the tunnel's course depicted in Fig. 7.2, the receiver was on the outer side in the left curve and, consequently, on the inner side in the following right curve at the end of the tunnel. The averaged measured path loss is plotted Fig. 7.15. At 850m to 950m from the transmitter, the curve is dropping by almost 8dB. This is the area of the right bend, with the receiver situated at the inner side of the curve.

In the same figure, the path loss predicted by the method of power flow is indicated by the dotted line. To allow a direct comparison, the gain of the receiving monopole in the horizontal direction ($\theta = 90^\circ$) was considered in the simulations. Although the overall propagation slope is predicted very well, the defocusing effect can obviously not be predicted by the integral method

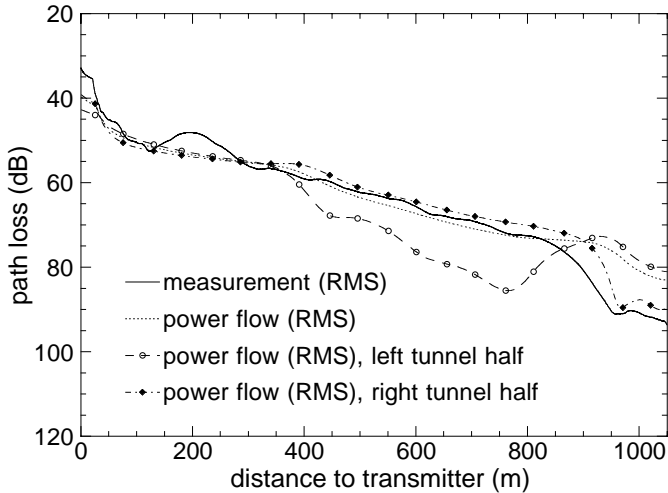


Figure 7.15: Total propagating power through the curved tunnel (U8) calculated by the method of power flow, compared to the averaged measurement of Fig. 7.5 at $f_{GSM} = 945\text{MHz}$ (RMS window length: $200\lambda_0$)

of power flow. In order to enable the power flow to detect such a shift of energy, the area of analysis is split. Instead of working on the total cross section of the tunnel, the method of power flow is now applied separately on the left and the right halves of the cross section. The power flow in the right half, shown by the curve with the black diamonds in Fig. 7.15, follows the measurement quite closely. Furthermore, the power flow in the left half is drawn in the figure. On the first 350m, where the tunnel is approximately straight, the energy is equally distributed on both sides of the tunnel. In the left curve (between 350m and 800m), the energy is focused on the right half of the tunnel. In the following right bend, the energy is shifted from the inner (right) side of the curve to the outer (left) side of the curve. The break-even point is at about 900m from the transmitter, after which most of the energy is gathered in the left tunnel half. This result again indicates the effect of curves on the propagation behaviour, and the requirement for an appropriate modelling approach. For the power flow, a total of $1 \cdot 10^5$ rays were launched with up to 40 reflections. The spacing between the reception planes was 5m. The simulation time for the power flow was about 3min, which translates to a factor of 800 times below the computation time of the power trace.

7.2 Influence of exterior antenna positions on the propagation behaviour

After the investigations in the Berlin subway in the previous section, the remainder of this chapter is dealing with the influence of exterior transmitter positions and the impact of moving vehicles on wave propagation. The different scenarios are examined by simulations.

7.2.1 Difference of interior and exterior positions

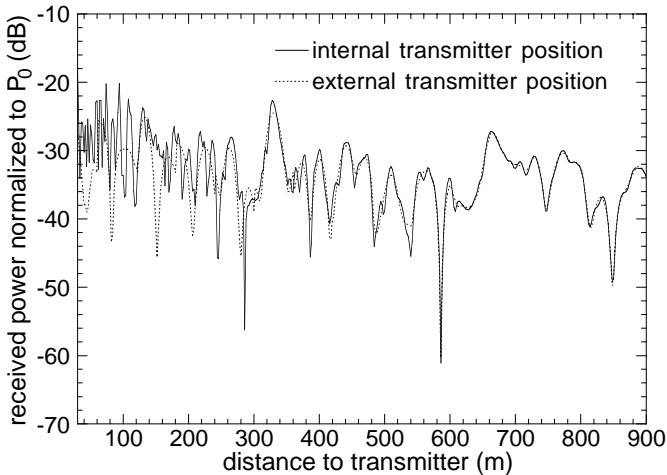


Figure 7.16: Influence of an exterior transmitter location on the received power level compared to a transmitter situated inside a straight rectangular tunnel

The influence of an exterior transmitting antenna on the received power level compared to a transmitter situated inside a tunnel is investigated by two initial simulations in a straight rectangular tunnel. The cross section of the tunnel is 10m wide and 5m high. For the first simulation, an omnidirectional transmitter is situated inside at the beginning of the tunnel at a height of 2.5m in a centric position. Secondly, the same transmitter is positioned outside, 30m in front of the tunnel entrance at the same height. Figure 7.16 shows the predicted received power levels as a function of the distance to the two respective transmitters. The power levels are computed with image theory and normalized to the reference power P_0 (3.35), according to chapter 5.

At small distances, the power level for the interior antenna relative to the exterior antenna is significantly higher. Also, the fluctuations of the power level

are more pronounced. At larger distances, however, the two curves converge. The reason for this is quite evident. In the vicinity of the interior antenna, many rays impinge almost homogeneously spread over a solid angle of 2π , resulting in a high reception level and a highly fluctuating interference pattern. Consider an increasing distance from the transmitter. The rays reaching the receivers via multiple reflections under large angles with respect to the tunnel axis, are highly attenuated. These rays can be interpreted as belonging to highly attenuated propagation modes. The remaining rays almost exclusively hit the receivers from the frontal direction, reflecting under grazing incidence, which corresponds to the less attenuated modes. For the exterior antenna position, only rays of the latter type enter the tunnel, resulting in the convergence of the two curves at large distances, where for the interior antenna position also the less-attenuated rays dominate.

7.2.2 Exterior antenna locations

7.2.2.1 Description of the scenario

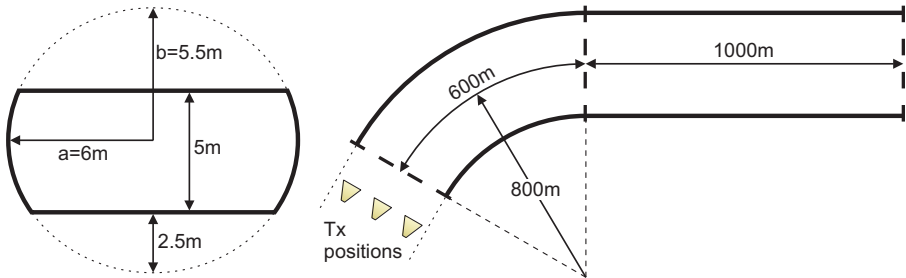


Figure 7.17: Cross section and course of the tunnel used for the simulations with exterior transmitting antenna locations

To integrally characterize the influence of different exterior transmitting antenna positions, the method of power flow is applied in the following. For all simulations, the tunnel illustrated in Fig. 7.17 is used. The basic form of the cross section is an ellipse with a horizontal half axis of $a = 6\text{m}$, and a vertical half axis of $b = 5.5\text{m}$. The floor is situated 2.5m above the lowest point of the ellipse, the total height of the tunnel is 5m . The course consists of two sections: a right bend of length $l_1 = 600\text{m}$ with radius of curvature $r_c = 800\text{m}$, followed by a straight section of length $l_2 = 1000\text{m}$. The transmitting antenna, a vertically polarized dipole, is located at different positions in front of the tunnel entrance. The mean received power level is calculated by the power flow approach over the entire cross section for each meter inside

the tunnel. The walls of the tunnel are smooth with a relative permittivity of $\epsilon_r = 5$, the frequency in all simulations is $f = 1\text{GHz}$.

7.2.2.2 Antenna height

First, the transmitting antenna is situated at a distance $d = 20\text{m}$ in front of the tunnel entrance at three different heights: $h_{T,1} = 0.5\text{m}$, $h_{T,2} = 2.5\text{m}$, and $h_{T,3} = 4.5\text{m}$. The predicted power level for each position is plotted in Fig. 7.18. Not surprisingly, the centric position ($h_{T,2} = 2.5\text{m}$) leads to the lowest path loss. The difference between the curves for $h_{T,1}$ and $h_{T,3}$ is partially due to the ground reflected rays in front of the tunnel entrance and the asymmetric shape of the cross-section.

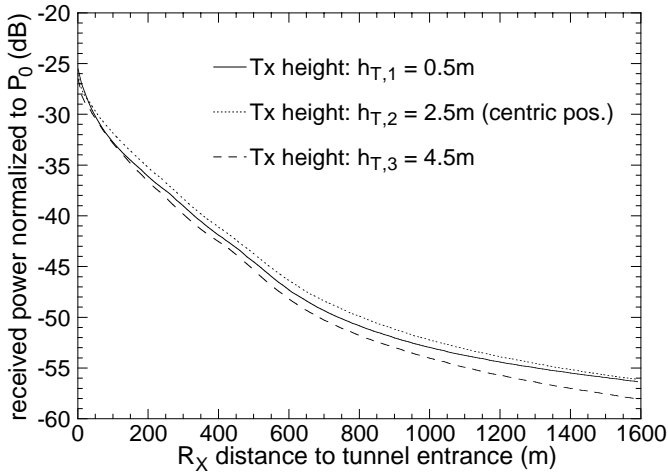


Figure 7.18: Comparison of the mean received power level for exterior antenna positions with different heights

7.2.2.3 Distance from the tunnel entrance

To determine the influence of the distance between the transmitter and the tunnel entrance, several simulations with a spacing of 1m, 20m, 50m, 80m and 120m between the transmitting antenna and the tunnel entrance are carried out. The height of the transmitters is always $h_T = 2.5\text{m}$. Figure 7.19 shows the results for various distances. The larger the distance from the transmitter to the tunnel entrance, the lower is the coupled power into the tunnel. Deep inside the tunnel, however, the curves are converging in analogy to the observations of

section 7.2.1. For a Tx-spacing of 80m, there exists a break-even point at about 800m from the tunnel entrance. Such a break-even point is only possible in curved geometries. Its occurrence strongly depends on the actual geometry of the tunnel and the (lateral) transmitter location, which will become apparent in the following section.

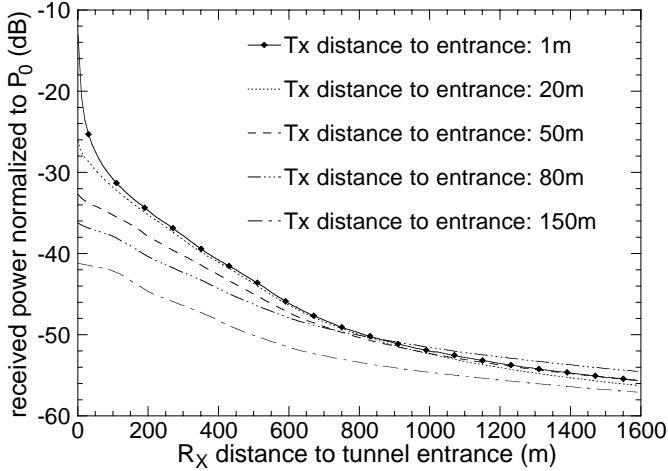


Figure 7.19: Comparison of the mean received power level for exterior antenna positions with varying distance to the tunnel entrance

7.2.2.4 Lateral placement

In the preceding cases, no lateral displacement of the transmitting antennas was examined. For the scenario of Fig. 7.17, the impact of such a lateral shift is investigated. At two distances $d = 20\text{m}$ and $d = 80\text{m}$ from the tunnel entrance, three different transmitting antenna locations are used, respectively. The first is the centric position, the second position is shifted by 5.5m to the left, whereas the third position is shifted accordingly by the same amount to the right. The Tx height at all positions equals $h_T = 2.5\text{m}$. As one would expect, the transmitting antenna at the left position results in the highest received power level, due to the largest area of direct tunnel illumination compared to the two other locations. Additionally, the difference in received power between the left and right Tx position is smaller for the larger spacing ($d = 80\text{m}$). Furthermore, no crossing of the curves is observed for the left Tx position, like in the case of a purely straight tunnel. It can therefore be concluded that the influence of a curve is less pronounced for a transmitter position moved

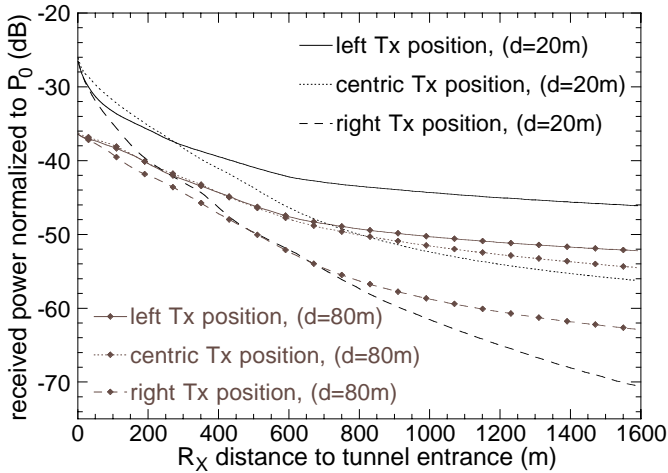


Figure 7.20: Comparison of the mean received power level for exterior antennas at different lateral positions

towards the outside of the curve.

To summarize, the simulations reveal a significant influence of the exterior transmitting antenna position on the electromagnetic wave propagation.

7.3 Moving vehicles and broadband analysis

In this section, the influence of moving vehicles on the propagation channel is considered. Three moving vehicles are situated in a straight rectangular tunnel. The tunnel is 9.9m wide and has a height of 4.8m. A truck with a speed of $v_1 = 15\text{m/s}$ and two cars with $v_2 = v_3 = 20\text{m/s}$ are driving through the tunnel. An omnidirectional transmitter is positioned at the tunnel entrance 1m below the ceiling. The frequency is $f = 1\text{GHz}$. This scenario has been calculated with a time interval of 1s at three consecutive time instants. Figure 7.21 depicts the results on the first 44m of the tunnel at a height of 1m above the floor obtained by the RDN-based power trace method. The resolution of the employed horizontal reception plane is $0.1\text{m} \times 0.1\text{m}$, resulting in $440 \times 99 = 43560$ discrete points. The vehicles are modelled as floating rectangular boxes according to section 4.4. Due to the horizontal orientation of the reception plane, a large number of 200 million rays has been traced to ensure sufficient convergence (cf. sections 4.5 and 6.4). Because of the PEC boundaries of the vehicles, up to 200 reflections were considered in the

simulation. The overall simulation time was about 5 days.

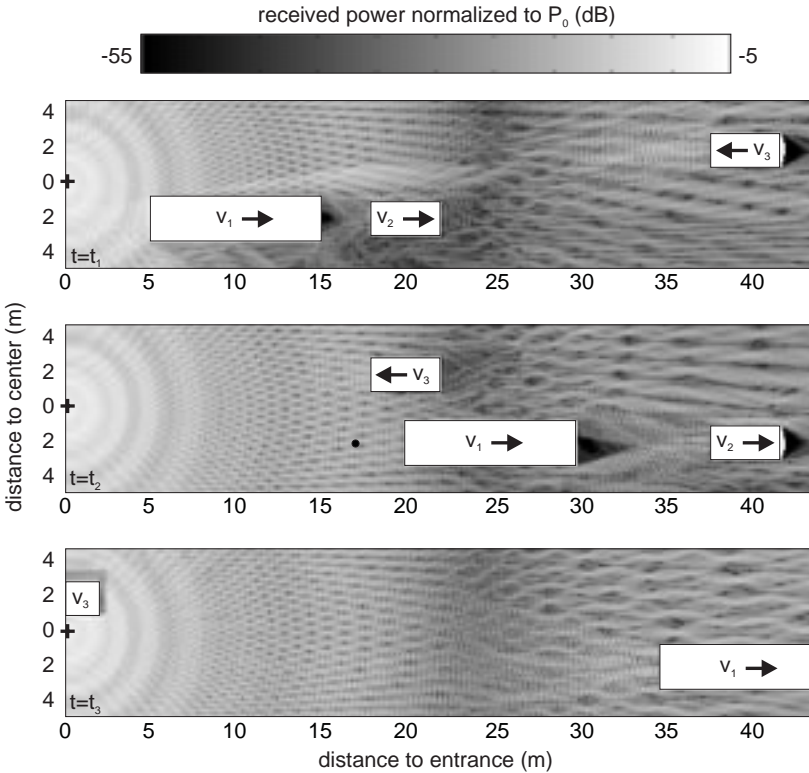


Figure 7.21: Power distribution in a straight rectangular tunnel with moving vehicles at three consecutive time instants at $f = 1\text{GHz}$, $v_1 = 15\text{m/s}$, $v_2 = v_3 = 20\text{m/s}$, (black dot at time instant $t = t_2$ indicates Rx position for power delay profile in Fig. 7.23)

In Fig. 7.21, various interference (standing wave) patterns can be identified resulting from reflections at the vehicles' boundaries. Delay and Doppler spreads at the second time instant $t = t_2$ are shown in Fig. 7.22. The delay spread is very small and thus negligible. The Doppler spread, however, is significant, exceeding 130Hz.

Finally, the power delay profile (PDP) at the receiver position indicated by a black dot in Fig. 7.21 is plotted in Fig. 7.23. The height of the receiver is 2m above the floor. The PDP is normalized to the input power P_T of the transmitting antenna, and thus obtained by the magnitude squared of (2.59). The first contribution corresponds to the direct path, which reaches the

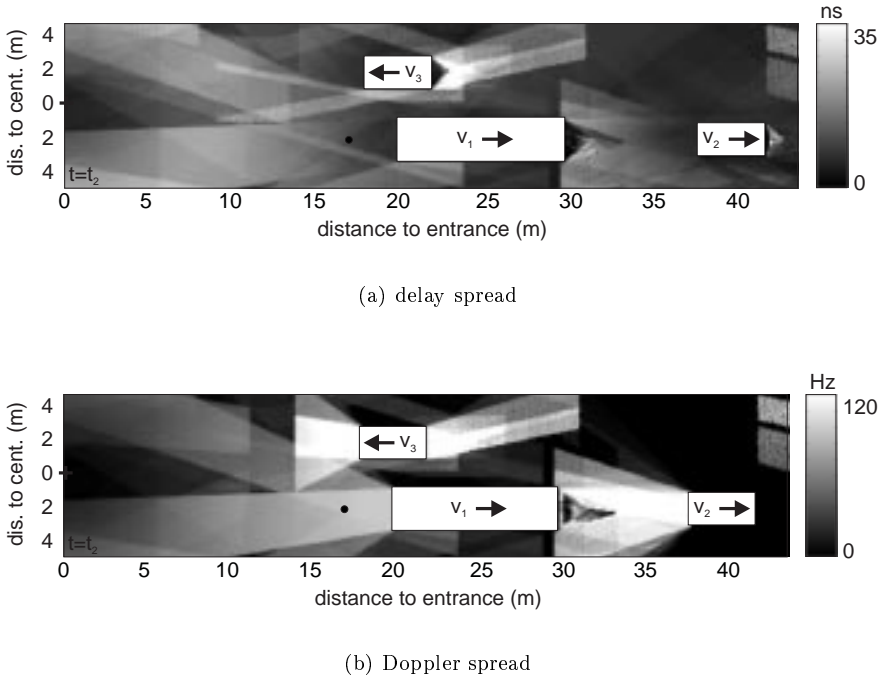


Figure 7.22: Delay and Doppler spreads at the time instant $t = t_2$ of Fig. 7.21

receiver with a delay of $\tau = 55.8\text{ns}$. The impulses with a black square indicate contributions by single reflected rays. In total, five rays reach the receiver via a single reflection. The first four are either reflected on the ground, the ceiling, or at the two side walls of the tunnel. The last single reflected contribution belongs to a backward reflected ray at the rear of the truck. It has the lowest attenuation of all reflected rays because of the lossless PEC boundary of the vehicle. Due to the relatively short delay lengths for this scenario, a system bandwidth of at least 100MHz (i.e. 10%-bandwidth) would be necessary to resolve the important multipath components.

In general, the Doppler spread in tunnels, especially road tunnels, can reach considerably large values and thus become important from a system point of view. The delay spread is less critical due to the absence of significant distant scatterers, unlike the scenarios for urban or rural environments [Lee82].

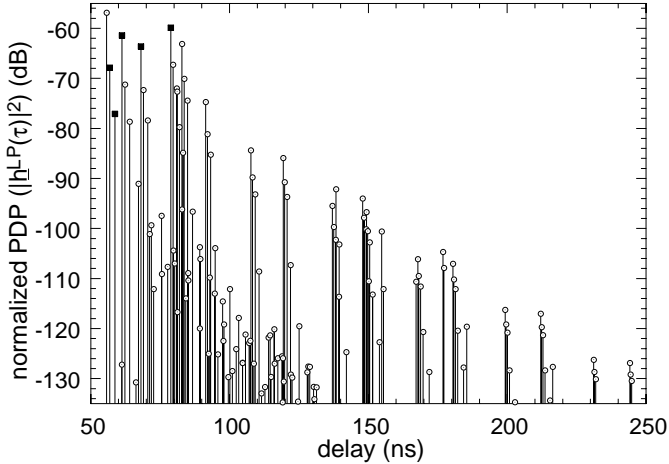


Figure 7.23: Power delay profile (PDP) at the receiver position indicated in Fig. 7.21 at the time instant $t = t_2$ at $f = 1\text{GHz}$, single reflected rays marked by black squares

7.4 Summary

In this chapter, the effectiveness of the proposed new modelling techniques has been proven. The approaches were applied to a variety of different scenarios and were able to deliver valuable prediction results. By comparison to measurements in the Berlin subway, it was shown that the geometry of tunnels, especially the cross-sectional shape and curves, have a major impact on the propagation behaviour. In order to obtain sufficiently accurate path loss predictions, it is mandatory to describe the special geometry of tunnels in propagation modelling adequately. It was also shown that the fast fading in tunnels cannot be characterized by standard analytical probability density functions over the entire range of values. The densities derived from propagation modelling provide a superior fit. Furthermore, the impact of exterior transmitting antenna locations was examined. Finally, the ability of the ray-based modelling approach to deliver broadband channel parameters has been pointed out.

Chapter 8

Conclusions

The research conducted in this thesis deals with the prediction of electromagnetic wave propagation in arbitrarily shaped tunnels on a ray-optical basis. The main motivation for this work was the inadequate knowledge of the propagation channel in such tunnels, and the lack of a technique for its sound description and analysis.

The necessary fundamentals in ray-optical wave propagation modelling, i.e. geometrical optics (GO) and ray-tracing techniques, were presented. It has been shown that the available methods were not able to accurately determine wave propagation in curved geometries. In order to overcome this shortcoming a new approach has been derived. The proposed ray density normalization (RDN) proves to be a powerful tool, able to predict electromagnetic wave propagation in arbitrarily shaped tunnels at frequencies in and above the UHF frequency range ($> 300\text{MHz}$) with an adequate precision. Additionally, the failure at caustics, which is inherent to GO, can be avoided by this new RDN approach. Furthermore, a fast, approximate way to determine the power flux through a tunnel has been presented. The inclusion of directive rough surface scattering in the deterministic propagation modelling, retaining the stochastic nature of the scattering process, has been developed for the use in system simulations. All techniques were verified theoretically using canonical examples. Experimental verifications in scaled model tunnels at 120GHz proved the validity of the RDN in real three-dimensional curvature in an impressive way. Finally, the applicability and performance of the approaches has been tested in real tunnel environments. For this purpose, measurements in the Berlin subway were conducted. It has been shown that the geometry of a tunnel, especially the cross-sectional shape and the course, is of major impact on the propagation behaviour and thus on the accuracy of the modelling. In

order to obtain reliable prediction results, the joint use of an adequate calculation technique, such as the presented RDN-based methods, and a correct modelling of the tunnel's geometry is required.

The major contributions of this work can be summarized as follows:

- a novel technique has been developed to calculate wave propagation in arbitrarily curved geometries with sufficient accuracy on a ray-optical basis,
- the failure of conventional GO-based ray tracing in the vicinity of caustics is overcome,
- the stochastic nature of rough surface scattering is included in a deterministic wave propagation model.

The application of this work together with the performed measurements led to novel insights regarding the propagation environment of a tunnel. In particular, the following:

- electromagnetic wave propagation in tunnels can be modelled properly and efficiently by ray techniques,
- the major influence on the prediction accuracy is the precision of the tunnel geometry model.

As a result, the concepts derived in this thesis offer new perspectives for both system analysis and coverage planning in arbitrarily shaped tunnels. For the former realistic time series, broadband parameters, and statistical analyses are obtained by a ray approach, including the effect of rough surface scattering. For the latter, sufficiently accurate path-loss predictions may now be obtained, including for the first time the actual geometry of a tunnel, the influence of the antennas, and polarization effects.

As a field for further research, the inclusion of leaky feeders in the modelling can be envisaged, and again, ray techniques seem to be a promising candidate [Mor99].

Appendix A

Principal radii of curvature of reflected astigmatic tube of rays

The principal radii of curvature $\rho_{1,2}^r$ and $\rho_{1,2}^i$ of the reflected and incident wavefront, respectively, are related in the following way [KP74, Bal89] (cf. Fig. 2.4)

$$\frac{1}{\rho_{1,2}^r} = \frac{1}{2} \left(\frac{1}{\rho_1^i} + \frac{1}{\rho_2^i} \right) + \frac{1}{f_{1,2}}. \quad (\text{A.1})$$

In general, f_1 and f_2 can be obtained by

$$\begin{aligned} \frac{1}{f_{1,2}} = & \frac{\cos \theta_i}{|\theta|^2} \left(\frac{\theta_{22}^2 + \theta_{12}^2}{R_1} + \frac{\theta_{21}^2 + \theta_{11}^2}{R_2} \right) \\ & \pm \frac{1}{2} \left\{ \left(\frac{1}{\rho_1^i} - \frac{1}{\rho_2^i} \right)^2 + \left(\frac{1}{\rho_1^i} - \frac{1}{\rho_2^i} \right) \frac{4 \cos \theta_i}{|\theta|^2} \left(\frac{\theta_{22}^2 - \theta_{12}^2}{R_1} + \frac{\theta_{21}^2 - \theta_{11}^2}{R_2} \right) \right. \\ & \left. + \frac{4 \cos^2 \theta_i}{|\theta|^4} \left[\left(\frac{\theta_{22}^2 + \theta_{12}^2}{R_1} + \frac{\theta_{21}^2 + \theta_{11}^2}{R_2} \right)^2 - \frac{4|\theta|^2}{R_1 R_2} \right] \right\}^{1/2}, \quad (\text{A.2}) \end{aligned}$$

where the plus sign is used for f_1 and the minus sign for f_2 . $R_{1,2}$ are the radii of curvature of the reflecting surface; for a convex surface $R_{1,2} > 0$, for a concave surface $R_{1,2} < 0$. $\theta_{j,k}$ and $|\theta|$ are determined by the principal directions of the radii of curvature of the reflecting surface ($\hat{u}_{1,2}$) and of the incident tube of

rays ($\hat{X}_{1,2}^i$)

$$[\theta] = \begin{bmatrix} \theta_{11} & \theta_{12} \\ \theta_{21} & \theta_{22} \end{bmatrix} = \begin{bmatrix} \hat{X}_1^i \cdot \hat{u}_1 & \hat{X}_1^i \cdot \hat{u}_2 \\ \hat{X}_2^i \cdot \hat{u}_1 & \hat{X}_2^i \cdot \hat{u}_2 \end{bmatrix} \quad (\text{A.3a})$$

$$|\theta| = \det[\theta] = (\hat{X}_1^i \cdot \hat{u}_1)(\hat{X}_2^i \cdot \hat{u}_2) - (\hat{X}_2^i \cdot \hat{u}_1)(\hat{X}_1^i \cdot \hat{u}_2). \quad (\text{A.3b})$$

In addition to the radii of curvature of the tube of rays, their principal directions are modified at the reflection. They are determined with the aid of the symmetric curvature matrix for the reflected wave front [Q^r]

$$[Q^r] = \begin{bmatrix} Q_{11}^r & Q_{12}^r \\ Q_{12}^r & Q_{22}^r \end{bmatrix}, \quad (\text{A.4})$$

whose entries are

$$Q_{11}^r = \frac{1}{\rho_1^i} + \frac{2 \cos \theta_i}{|\theta|^2} \left(\frac{\theta_{22}^2}{R_1} + \frac{\theta_{21}^2}{R_2} \right) \quad (\text{A.5a})$$

$$Q_{12}^r = -\frac{2 \cos \theta_i}{|\theta|^2} \left(\frac{\theta_{22}\theta_{12}}{R_1} + \frac{\theta_{11}\theta_{21}}{R_2} \right) \quad (\text{A.5b})$$

$$Q_{22}^r = \frac{1}{\rho_2^i} + \frac{2 \cos \theta_i}{|\theta|^2} \left(\frac{\theta_{12}^2}{R_1} + \frac{\theta_{11}^2}{R_2} \right). \quad (\text{A.5c})$$

The principal directions $\hat{X}_{1,2}^r$ of the reflected wave front can now be written as

$$\hat{X}_1^r = \frac{\left(Q_{22}^r - \frac{1}{\rho_1^r} \right) \hat{e}_1^r - Q_{12}^r \hat{e}_2^r}{\sqrt{\left(Q_{22}^r - \frac{1}{\rho_1^r} \right)^2 + (Q_{12}^r)^2}} \quad (\text{A.6a})$$

$$\hat{X}_2^r = -\hat{k}^r \times \hat{X}_1^r, \quad (\text{A.6b})$$

with

$$\hat{e}_{1,2}^r = \hat{X}_{1,2}^i - 2(\hat{n} \cdot \hat{X}_{1,2}^i) \hat{n}. \quad (\text{A.7})$$

Notes on the implementation:

- The initial principal directions of the wavefront curvature can be chosen arbitrarily¹, because for a point source, the radii of curvature are equal and therefore have no specific direction.
- The radii of curvature of the reflecting curved surfaces, i.e. the tunnel's walls, and their directions are given in appendix B.

¹Arbitrarily in this context still means perpendicular to each other and to the direction of propagation.

Appendix B

Intersection algorithms

Let a ray be defined by the equation

$$\vec{r} = \vec{b}_r + \lambda \hat{d}_r, \tag{B.1}$$

where \vec{b}_r is the base and \hat{d}_r is the direction of the ray. In the following intersection algorithms, the parameter λ is determined, such that the actual intersection points of the ray and the respective objects can be obtained by inserting λ into (B.1).

The algorithms for the plane, the rectangle, the sphere and the circular cylinder are all based on geometrical considerations and are taken from the literature [Gla89, Gla95, Web96]. The algorithms for the elliptical cylinder and the torus are derived applying analytical geometry [SW98].

For the cylinders and the torus, in addition to the intersection algorithms, the normal vectors in the intersection points, as well as the principal radii of curvature and their directions are given, since they are needed for the calculation of the reflected tube of rays (cf. section 2.3.2 and appendix A).

The orientation of the respective objects in space is chosen in accordance to their usage in the simulation approach.

B.1 Plane

Let a plane be defined by its normal form

$$(\vec{x} - \vec{b}_p) \cdot \hat{n} = 0, \tag{B.2}$$

where \vec{b}_p is the base and \hat{n} is the normal of the plane. The parameter λ , which defines the intersection point of the plane and the ray of (B.1), is obtained by

substituting (B.1) in (B.2) [Gla89, chap. 2], [Web96]

$$\lambda = \frac{(\vec{b}_p - \vec{b}_r) \cdot \hat{n}}{\hat{d}_r \cdot \hat{n}}. \quad (\text{B.3})$$

B.2 Rectangle

Rectangles are used in the simulation approach for any planar boundary (i.e. walls, floors, ceilings, reception planes, the boundary of vehicles etc.). Let a rectangle be defined by a base point \vec{b}_\square , which is one of the corners of the rectangle, and the two orthogonal vectors $\vec{d}_{\square,1/2}$ with length $|\vec{d}_{\square,1/2}|$ and direction $\hat{d}_{\square,1/2}$.

Beforehand, the intersection point \vec{Q} of the ray and the plane, which contains the rectangle, has to be determined (cf. appendix B.1). The intersection point \vec{Q} lies in the rectangle, if [Gla89, chap. 2]

$$0 \leq (\vec{Q} - \vec{b}_\square) \cdot \hat{d}_{\square,1/2} \leq |\vec{d}_{\square,1/2}|. \quad (\text{B.4})$$

B.3 Sphere

Spheres are used in the simulation approach for the reception spheres and bounding boxes of vehicles. Let the sphere be defined by its central point \vec{b}_\circ and its radius r_\circ . The parameters λ , which define the two possible intersection points of the sphere and the ray of (B.1), are given by [Gla89, chap. 2], [Gla95, vol. I, chap. 7]

$$\lambda = a \mp b, \quad (\text{B.5})$$

with

$$a = (\vec{b}_\circ - \vec{b}_r) \cdot \hat{d}_r, \quad (\text{B.6a})$$

$$b = \sqrt{r_\circ^2 - (|\vec{b}_\circ - \vec{b}_r|^2 - a^2)}, \quad (\text{B.6b})$$

where a is the distance between the base point of the ray and the central point of the sphere projected in the direction of the ray, b is half the distance between the two intersection points. These two solutions only exist, if the radical in (B.6b) is non-negative. For $b = 0$, there is obviously only one possible intersection point.

B.4 Circular cylinder

Circular cylinders are used in the simulation approach for the side walls of curved rectangular tunnel sections. Let a circular cylinder be defined by its radius r_{cc} and its axis, which is identical to the z -axis of a cartesian coordinate system with direction \hat{e}_z . The minimum distance from the ray to the axis of the cylinder (subscript: rta) is given by

$$d_{rta} = \left| \vec{b}_r \cdot \frac{\hat{d}_r \times \hat{e}_z}{|\hat{d}_r \times \hat{e}_z|} \right|. \quad (\text{B.7})$$

The distance from the base of the ray \vec{b}_r to the point of minimum distance (subscript: btp) is given by

$$d_{btp} = \frac{(\hat{e}_z \times \vec{b}_r) \cdot \frac{\hat{d}_r \times \hat{e}_z}{|\hat{d}_r \times \hat{e}_z|}}{|\hat{d}_r \times \hat{e}_z|}. \quad (\text{B.8})$$

The distance of the point of minimum distance to the intersection points of the ray with the cylinder (subscript: pti) is given by

$$d_{pti} = \left| \frac{\sqrt{r_{cc}^2 - d_{rta}^2}}{\hat{d}_r \cdot \hat{h}} \right| \quad (\text{B.9a})$$

$$\hat{h} = \frac{\frac{\hat{d}_r \times \hat{e}_z}{|\hat{d}_r \times \hat{e}_z|} \times \hat{e}_z}{\left| \frac{\hat{d}_r \times \hat{e}_z}{|\hat{d}_r \times \hat{e}_z|} \times \hat{e}_z \right|}. \quad (\text{B.9b})$$

The parameters λ , which define the intersection points of the ray defined by (B.1) with the circular cylinder are therefore given by [Gla95, vol. IV, chap. 5]

$$\lambda = d_{btp} \mp d_{pti}. \quad (\text{B.10})$$

In the simulation approach of section 4.1, where the circular cylinder is used to model the side walls of a curved tunnel with rectangular cross section, only the smaller λ —corresponding to the “minus”-sign—is required.

Let the intersection point \vec{Q} be given in cartesian coordinates by $\vec{Q} = (x_q, y_q, z_q)^T$. Then, a vector in the direction of the normal to the circular cylinder in \vec{Q} is determined by

$$\vec{n} = (\pm x_q, \pm y_q, 0)^T, \quad (\text{B.11})$$

where the “plus”-sign is used for the “inner” side of the curve and the “minus”-sign for the “outer” one. The first principal radius of curvature in \vec{Q} is given

by the radius of the cylinder

$$R = \pm r_{cc}, \quad (\text{B.12})$$

with the corresponding principal direction

$$\hat{u} = \frac{\vec{n} \times \hat{e}_z}{|\vec{n} \times \hat{e}_z|}. \quad (\text{B.13})$$

Since a cylinder only has a 2D-curvature, the second radius of curvature in the direction \hat{e}_z is infinite.

B.5 Elliptical cylinder

Elliptical cylinders are used in the simulation approach for straight circular, elliptical, or arched tunnel sections. Let an elliptical cylinder be defined by

$$\frac{x^2}{a^2} + \frac{z^2}{b^2} = 1, \quad (\text{B.14})$$

where a and b denote the half-axes of the elliptical cross section of the cylinder. The axis of the cylinder is identical to the y -axis of a cartesian coordinate system with direction \hat{e}_y . The ray equation in cartesian coordinates is given by

$$\vec{r} = (x_r, y_r, z_r)^T = (x_{r0} + \lambda x_{dr}, y_{r0} + \lambda y_{dr}, z_{r0} + \lambda z_{dr})^T, \quad (\text{B.15})$$

where the index dr is used for the direction of the ray. Inserting (B.15) into (B.14) leads to the quadric equation [SW98]

$$A\lambda^2 + 2B\lambda + C = 0 \quad (\text{B.16a})$$

$$A = x_{dr}^2 + \frac{a^2}{b^2} z_{dr}^2 \quad (\text{B.16b})$$

$$B = x_{r0}x_{dr} + \frac{a^2}{b^2} z_{r0}z_{dr} \quad (\text{B.16c})$$

$$C = x_{r0}^2 + \frac{a^2}{b^2} z_{r0}^2 - a^2. \quad (\text{B.16d})$$

The parameters λ , which define the intersection points of the ray defined by (B.15) with the elliptical cylinder, are therefore given by

$$\lambda = \frac{-B \pm \sqrt{B^2 - AC}}{A}. \quad (\text{B.17})$$

In the simulation approach of section 4.1, where the elliptical cylinder is used to partially model the boundary of a straight arched tunnel, only the positive λ —corresponding to the “plus”-sign—is needed. The second (negative) root of (B.16a) is not of interest, because it leads to an intersection point in the reverse propagation direction of the ray.

Let the intersection point \vec{Q} be given in cartesian coordinates by $\vec{Q} = (x_q, y_q, z_q)^T$. Then, a vector in the direction of the normal to the elliptical cylinder in \vec{Q} (pointing to the inner side of the cylinder) is determined by

$$\vec{n} = (-b^2 x_q, 0, -a^2 z_q)^T. \quad (\text{B.18})$$

The principal radius of curvature in \vec{Q} is given by [BS⁺99]

$$R = -a^2 b^2 \left(\frac{x_q^2}{a^4} + \frac{z_q^2}{b^4} \right)^{\frac{3}{2}}, \quad (\text{B.19})$$

with the corresponding principal direction

$$\hat{u} = \frac{\vec{n} \times \hat{e}_y}{|\vec{n} \times \hat{e}_y|}. \quad (\text{B.20})$$

Because a cylinder has only a 2D-curvature, the second radius of curvature in the direction \hat{e}_y is obviously infinite.

Notice, that a general algorithm to intersect a ray with a quadric surface has been proposed [Gla95, vol. III, chap. 6], which can be used alternatively for the elliptical cylinder.

B.6 Elliptical torus

Elliptical tori are used in the simulation approach for curved circular, elliptical, or arched tunnel sections. Let an elliptical torus be defined by

$$\frac{\left(\sqrt{x^2 + y^2} - r_t \right)^2}{a^2} + \frac{z^2}{b^2} = 1, \quad (\text{B.21})$$

where a, b denote the half-axes of the elliptical cross section and r_t the radius of the torus. Inserting the ray equation (B.15) into (B.21) leads to the 4th-order equation (quartic)

$$A\lambda^4 + B\lambda^3 + C\lambda^2 + D\lambda + E = 0, \quad (\text{B.22})$$

with [SW98]

$$A = \left(x_{dr}^2 + y_{dr}^2 + \frac{a^2}{b^2} z_{dr}^2 \right)^2 \quad (\text{B.23a})$$

$$B = 4 \left(x_{dr}^2 + y_{dr}^2 + \frac{a^2}{b^2} z_{dr}^2 \right) \left(x_{r0} x_{dr} + y_{r0} y_{dr} + \frac{a^2}{b^2} z_{r0} z_{dr} \right) \quad (\text{B.23b})$$

$$C = 2 \left(x_{dr}^2 + y_{dr}^2 + \frac{a^2}{b^2} z_{dr}^2 \right) \left(x_{r0}^2 + y_{r0}^2 + \frac{a^2}{b^2} z_{r0}^2 - r_t^2 - a^2 \right) \\ + 4r_t^2 \frac{a^2}{b^2} z_{dr}^2 + 4 \left(x_{r0} x_{dr} + y_{r0} y_{dr} + \frac{a^2}{b^2} z_{r0} z_{dr} \right)^2 \quad (\text{B.23c})$$

$$D = 4 \left(x_{r0}^2 + y_{r0}^2 + \frac{a^2}{b^2} z_{r0}^2 - r_t^2 - a^2 \right) \left(x_{r0} x_{dr} + y_{r0} y_{dr} + \frac{a^2}{b^2} z_{r0} z_{dr} \right) \\ + 8r_t^2 \frac{a^2}{b^2} z_{r0} z_{dr} \quad (\text{B.23d})$$

$$E = \left(x_{r0}^2 + y_{r0}^2 + \frac{a^2}{b^2} z_{r0}^2 \right) \left(x_{r0}^2 + y_{r0}^2 + \frac{a^2}{b^2} z_{r0}^2 - 2(r_t^2 + a^2) \right) \\ + 4r_t^2 \frac{a^2}{b^2} z_{r0}^2 + (r_t^2 - a^2)^2. \quad (\text{B.23e})$$

Equation (B.22) is transformed to its reduced form by substituting $\lambda = \zeta - \frac{B}{4A}$. A reduced quartic can be solved via its *resolvent cubic* [BS⁺99], which is a third order equation. A further substitution of $\zeta = \gamma - \varrho$, with

$$\varrho = \frac{1}{A^2} \left(\frac{2}{3} AC - \frac{1}{4} B^2 \right), \quad (\text{B.24})$$

leads to the reduced form of the resolvent cubic

$$\gamma^3 + p\gamma + q = 0, \quad (\text{B.25})$$

with

$$p = \frac{1}{A^2} \left(BD - 4AE - \frac{1}{3} C^2 \right) \quad (\text{B.26a})$$

$$q = \frac{1}{(3A)^3} \left(72ACE - 27(AD^2 + B^2E) + 9BCD - 2C^3 \right). \quad (\text{B.26b})$$

The roots of any reduced cubic—and thus of (B.25)—are given by *Cardano's* formulas [BS⁺99]

$$\gamma_1 = \mu + \nu \quad (\text{B.27a})$$

$$\gamma_2 = -\frac{\mu + \nu}{2} + \frac{\mu - \nu}{2} j \sqrt{3} \quad (\text{B.27b})$$

$$\gamma_3 = -\frac{\mu + \nu}{2} - \frac{\mu - \nu}{2} j \sqrt{3}, \quad (\text{B.27c})$$

with

$$\mu = \sqrt[3]{-\frac{q}{2} + \sqrt{\delta}}, \quad \nu = -\frac{p}{3\mu}, \quad \delta = \left(\frac{p}{3}\right)^3 + \left(\frac{q}{2}\right)^2. \quad (\text{B.28})$$

The parameters λ in (B.22) can now be obtained from the solutions of the cubic resolvent given by

$$\zeta_i = \gamma_i - \varrho \quad \forall i \in \{1, 2, 3\}, \quad (\text{B.29})$$

leading to

$$\lambda_1 = \frac{1}{2}(\sqrt{\zeta_1} + \sqrt{\zeta_2} - \sqrt{\zeta_3}) - \frac{B}{4A} \quad (\text{B.30a})$$

$$\lambda_2 = \frac{1}{2}(\sqrt{\zeta_1} - \sqrt{\zeta_2} + \sqrt{\zeta_3}) - \frac{B}{4A} \quad (\text{B.30b})$$

$$\lambda_3 = \frac{1}{2}(-\sqrt{\zeta_1} + \sqrt{\zeta_2} + \sqrt{\zeta_3}) - \frac{B}{4A} \quad (\text{B.30c})$$

$$\lambda_4 = \frac{1}{2}(-\sqrt{\zeta_1} - \sqrt{\zeta_2} - \sqrt{\zeta_3}) - \frac{B}{4A}. \quad (\text{B.30d})$$

Additionally to the sign convention of (B.30), the values of the radicals¹ have to be chosen to satisfy

$$\sqrt{\zeta_1}\sqrt{\zeta_2}\sqrt{\zeta_3} = \frac{D}{A} - \frac{BC}{2A^2} + \frac{B^3}{8A^3}. \quad (\text{B.31})$$

In the simulation approach of section 4.1, the elliptical torus is used to partially model the boundary of a curved arched tunnel. Therefore only the smallest positive non-complex λ leads to the desired intersection point of the ray and the elliptical torus.

Again, let the point of intersection \vec{Q} be given in cartesian coordinates by $\vec{Q} = (x_q, y_q, z_q)^T$. Then, a vector in the direction of the normal to the elliptical torus in \vec{Q} (pointing to the inner side of the torus) is determined by [SW98]

$$\vec{n} = \left(x_q \left(r_t - \sqrt{x_q^2 + y_q^2} \right), y_q \left(r_t - \sqrt{x_q^2 + y_q^2} \right), -\frac{a^2}{b^2} z_q \sqrt{x_q^2 + y_q^2} \right)^T. \quad (\text{B.32})$$

The previous equation is obtained from (B.18) by a variable transformation.

¹I.e. the signs of the square roots.

The principal radii of curvature in \vec{Q} are given by

$$R_1 = -a^2 b^2 \left(\left(\frac{r_t - \sqrt{x_q^2 + y_q^2}}{a^2} \right)^2 + \left(\frac{z_q}{b^2} \right)^2 \right)^{\frac{3}{2}} \quad (\text{B.33a})$$

$$R_2 = \frac{\sqrt{x_q^2 + y_q^2}}{\hat{n} \cdot \hat{R}_Q} = \frac{|\vec{n}|}{\left(r_t - \sqrt{x_q^2 + y_q^2} \right)}, \quad (\text{B.33b})$$

with the corresponding principal directions

$$\hat{u}_1 = \frac{\vec{n} \times \hat{u}_2}{|\vec{n} \times \hat{u}_2|} \quad (\text{B.34a})$$

$$\hat{u}_2 = \frac{\vec{Q} \times \hat{e}_z}{|\vec{Q} \times \hat{e}_z|}. \quad (\text{B.34b})$$

In (B.33b), \hat{R}_Q denotes the direction of \vec{Q} projected into the xy -plane

$$\hat{R}_Q = \frac{1}{\sqrt{x_q^2 + y_q^2}} (x_q, y_q, 0)^T, \quad (\text{B.35})$$

\hat{n} the direction, and $|\vec{n}|$ the length of \vec{n} given by (B.32). (B.33a) follows directly from (B.19) by substituting x_q with $r_t - \sqrt{x_q^2 + y_q^2}$, (B.33b) follows from the theorem of *Meusnier* [BS⁺99].

Notice, that a general quartic roots solver has been proposed by [Gla95, vol. I, chap. 8], which can be used alternatively for intersecting a ray with an elliptical torus [Gla95, vol. II, chap. 5].

Appendix C

Determination of the send-range for exterior antenna positions

The send-range determines, in which directions the rays have to be launched for an exterior antenna placement, in order to enter the tunnel directly or via an intermediate ground reflection (cf. section 4.3). The send-range is expressed in spherical coordinates by the two limiting angles ϕ_{min} and ϕ_{max} in azimuth, and by the two angles $\theta_{min}(\phi)$ and $\theta_{max}(\phi)$ in elevation, with $\phi_{min} \leq \phi \leq \phi_{max}$. For $\theta = 0$ the rays are launched in the direction of \hat{e}_z , for $\theta = \frac{\pi}{2}$ and $\phi = 0$ they are launched in the direction of \hat{e}_y ¹, which is along the tunnel axis. \hat{e}_x , \hat{e}_y and \hat{e}_z are defined according to Figs. C.1 and C.2.

C.1 Rectangular cross section

The scenario of an exterior transmitting antenna placed in front of a rectangular tunnel is depicted in Fig. C.1. Let the width of the tunnel be given by w_{\square} and its height by h_{\square} . Let the distance between transmitter tunnel entrance be d_T , its height h_T , and its eccentricity, i.e. its distance from the middle of the road, be Δ_T , where a positive Δ_T indicates a shift in the direction of \hat{e}_x (to the right lane, whilst looking towards the entrance), whereas a negative Δ_T indicates a shift in the opposite direction. The send-range in azimuth² is

¹Not \hat{e}_x !

² ϕ is taken in the mathematical positive sense.

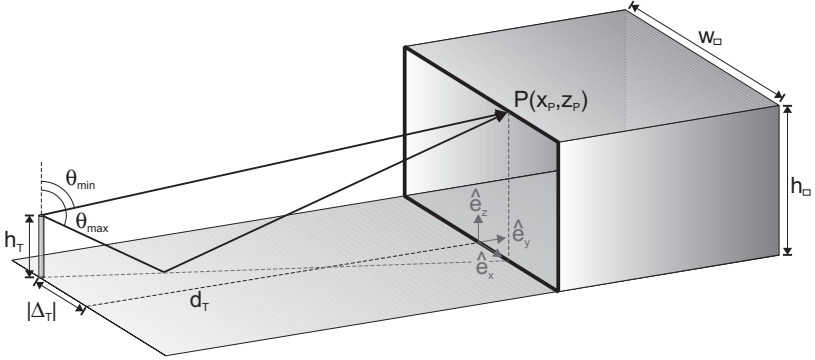


Figure C.1: Geometry of a rectangular tunnel entrance with exterior antenna placement for the determination of the send-range

therefore given by

$$\phi_{min} = 2\pi - \arctan\left(\frac{\frac{w_{\square}}{2} - \Delta_T}{d_T}\right) \quad (\text{C.1a})$$

$$\phi_{max} = \arctan\left(\frac{\frac{w_{\square}}{2} + \Delta_T}{d_T}\right). \quad (\text{C.1b})$$

The send-range in elevation is first stated in dependence of the x -component x_P of the point P in Fig. C.1, which is

$$\theta_{min}(x_P) = \arctan\left(\frac{\sqrt{(\Delta_T - x_P)^2 + d_T^2}}{h_{\square} - h_T}\right) \quad (\text{C.2a})$$

$$\theta_{max}(x_P) = \frac{\pi}{2} + \arctan\left(\frac{h_{\square} + h_T}{\sqrt{(\Delta_T - x_P)^2 + d_T^2}}\right). \quad (\text{C.2b})$$

Using the relation

$$x_P = \Delta_T - d_T \tan \phi, \quad (\text{C.3})$$

one finally obtains [CG99]

$$\theta_{min}(\phi) = \arctan\left(\frac{d_T}{(h_{\square} - h_T) \cos \phi}\right) \quad (\text{C.4a})$$

$$\theta_{max}(\phi) = \frac{\pi}{2} + \arctan\left(\frac{(h_{\square} + h_T) \cos \phi}{d_T}\right). \quad (\text{C.4b})$$

C.2 Elliptical (arched) cross section

The scenario of an exterior transmitting antenna placed in front of an elliptical (arched) tunnel is depicted in Fig. C.2. Let the horizontal half-axis of the ellipse be given by a , the vertical half-axis by b , and the height of the road/rail level be given by h_o . The transmitting antenna position is given by Δ_T , d_T , and h_T , like in the previous section.

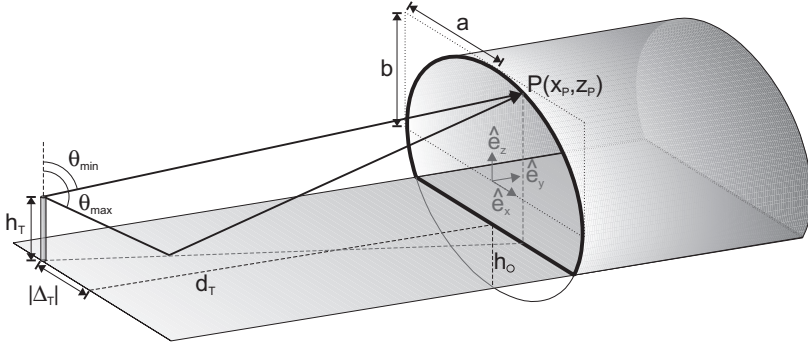


Figure C.2: Geometry of an elliptical (arched) tunnel entrance with exterior antenna placement for the determination of the send-range

If the road/rail level is lower than the vertical half-axis of the ellipse, i.e. if $h_o \leq b$, the send-range in azimuth is determined by

$$\phi_{min} = 2\pi - \arctan\left(\frac{a - \Delta_T}{d_T}\right) \quad (\text{C.5a})$$

$$\phi_{max} = \arctan\left(\frac{a + \Delta_T}{d_T}\right). \quad (\text{C.5b})$$

Otherwise, for $h_o > b$, it is given by

$$\phi_{min,o} = 2\pi - \arctan\left(\frac{a\sqrt{1 - \left(\frac{h_o}{b} - 1\right)^2} - \Delta_T}{d_T}\right) \quad (\text{C.6a})$$

$$\phi_{max,o} = \arctan\left(\frac{a\sqrt{1 - \left(\frac{h_o}{b} - 1\right)^2} + \Delta_T}{d_T}\right). \quad (\text{C.6b})$$

The send-range in elevation is first stated in dependence of the x - and z -components x_P , z_P of the point P in Fig. C.2. Furthermore, the send-range

has to be split for the direct ray entry and the ray entry via intermediate ground reflection. For the direct rays, the elevation is limited by

$$\theta_{min,max}^d(x_P, z_P) = \arctan \left(\frac{\sqrt{(\Delta_T - x_P)^2 + d_T^2}}{\pm z_P + b - h_T - h_o} \right). \quad (C.7)$$

For the reflected rays it becomes

$$\theta_{min,max}^r(x_P, z_P) = \frac{\pi}{2} + \arctan \left(\frac{\mp z_P + b + h_T - h_o}{\sqrt{(\Delta_T - x_P)^2 + d_T^2}} \right). \quad (C.8)$$

Using the equation of the ellipse (B.14) and (C.3), one finally obtains

$$\theta_{min,max}^d(\phi) = \arctan \left(\frac{d_T}{\left(\pm b \sqrt{1 - \frac{(\Delta_T - d_T \tan \phi)^2}{a^2}} + b - h_T - h_o \right) \cos \phi} \right) \quad (C.9)$$

and

$$\theta_{min,max}^r(\phi) = \frac{\pi}{2} + \arctan \left(\frac{\left(\mp b \sqrt{1 - \frac{(\Delta_T - d_T \tan \phi)^2}{a^2}} + b + h_T - h_o \right) \cos \phi}{d_T} \right). \quad (C.10)$$

For $\phi_{min,o} \leq \phi < 2\pi$ and $0 \leq \phi \leq \phi_{max,o}$, which is always the case for $h_o \geq b$, the two send ranges join and can thus be bound by $\theta_{min} = \theta_{min}^d$ and $\theta_{max} = \theta_{max}^r$.

If a ceiling is present in the tunnel, an additional test has to be performed: if the height of the ceiling³ is larger than the actual distance from point $P(\phi)$ to the street/rail level, the send range in elevation is calculated according to (C.9) and (C.10), otherwise it is calculated according to (C.4).

³The height of the ceiling is measured from the road/rail level to the ceiling.

Appendix D

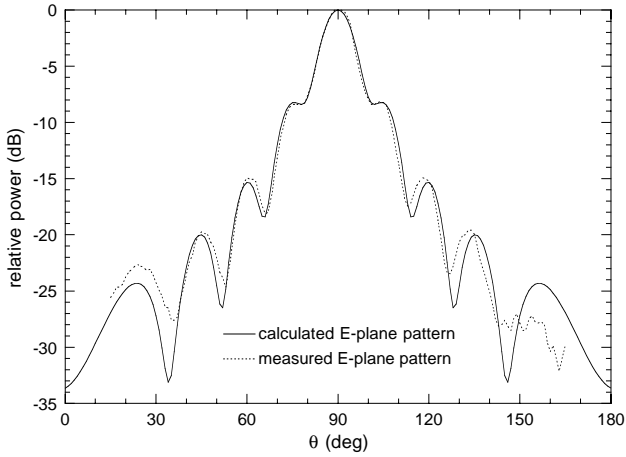
Directional antenna patterns

In the following, the directional patterns of the antennas used in chapters 6 and 7 are given.

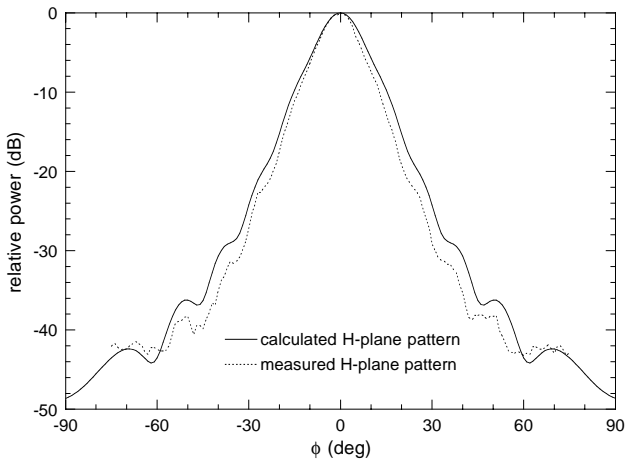
D.1 D-band standard gain horn and waveguide probe

The directional patterns of the D-band (110GHz–170GHz) standard gain horn and the waveguide probe have been measured and calculated at $f = 120\text{GHz}$. The calculation was done according to the usual procedure for pyramidal horns based on the equivalence principle techniques [Bal97, chap. 13].

For the standard gain horn, the measured and calculated patterns coincide very well (cf. Fig. D.1). Therefore the measured patterns are taken in the simulations of the scaled model tunnels of chapter 6. The measured patterns of the waveguide probe, however, are heavily oscillating, although following the same trend as the calculations (cf. Fig. D.2). The reason for this might be an induced current in the aperture edges having a finite thickness, which leads to additional field components neglected by the calculation method. Since the measured patterns itself could not be reproduced, the calculated patterns are used in the simulations of chapter 6.

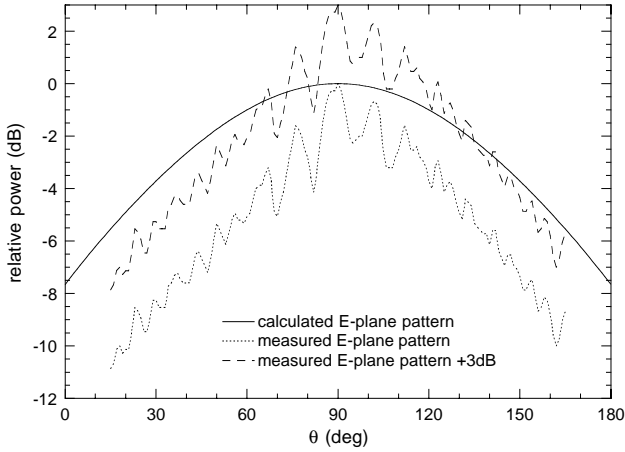


(a) E-plane pattern

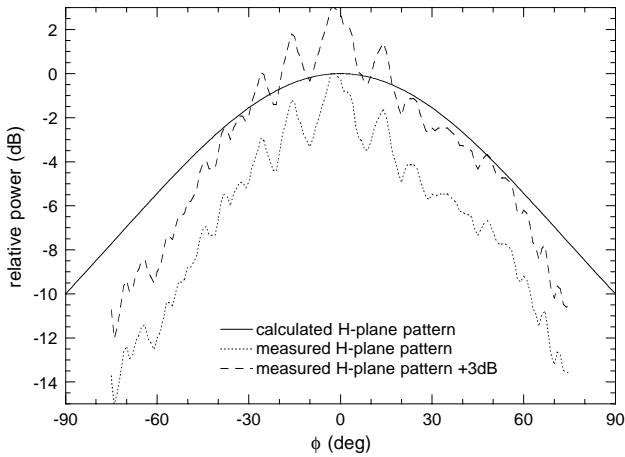


(b) H-plane pattern

Figure D.1: Measured and calculated directional E- and H-plane patterns of the D-band standard gain horn, $f = 120\text{GHz}$, gain: $G = 22\text{dBi}$



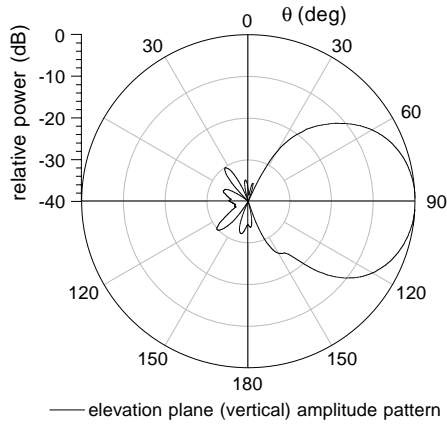
(a) E-plane pattern



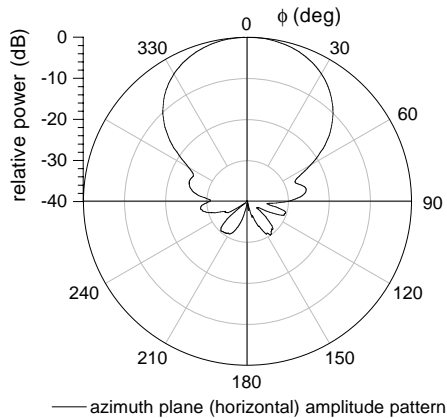
(b) H-plane pattern

Figure D.2: Measured and calculated directional E- and H-plane patterns of the D-band waveguide probe, $f = 120\text{GHz}$, gain: $G = 3.6\text{dBi}$

D.2 Kathrein K73226X (LogPer)



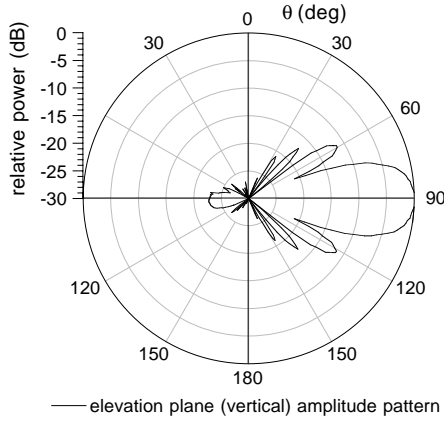
(a) elevation plane (vertical)



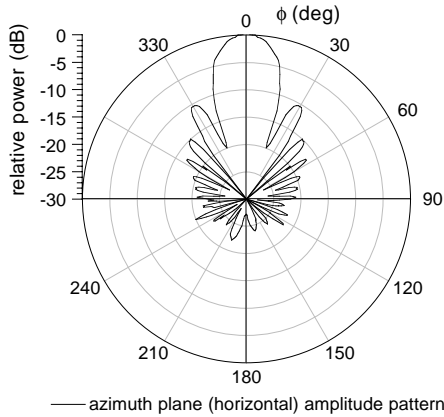
(b) azimuth plane (horizontal)

Figure D.3: Directional patterns of the Kathrein K73226X (LogPer) antenna, $f = 947.5\text{MHz}$, gain: $G = 12.3\text{dBi}$, source: Kathrein-Werke KG, Rosenheim, Germany

D.3 Jaybeam J7360 (Yagi)



(a) elevation plane (vertical)



(b) azimuth plane (horizontal)

Figure D.4: Directional patterns of the Jaybeam J7360 (Yagi) antenna, $f = 1830\text{MHz}$, gain: $G = 17\text{dBi}$, source: Jaybeam Ltd, Northampton, England

D.4 $\lambda/4$ -monopoles with circular ground plane

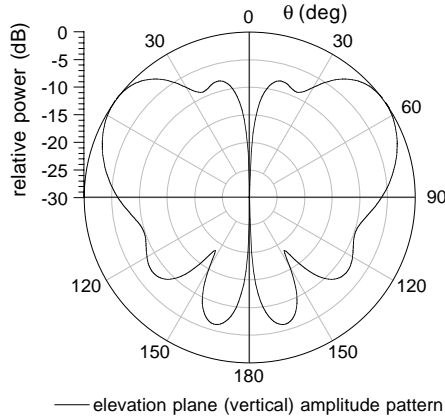
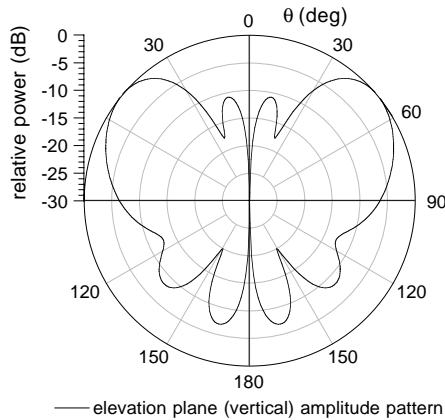
(a) 945MHz, gain: $G = 4.5\text{dBi}$ (b) 1853.4MHz, gain: $G = 4.9\text{dBi}$

Figure D.5: Directional elevation plane (vertical) amplitude patterns of the two $\lambda/4$ -monopoles with circular ground plane, calculated by the method of moments (MoM) with FEKO, EMSS, Stellenbosch, South Africa

Bibliography

- [AF78] R. Axeline and A.K. Fung, "Numerical computation of scattering from a perfectly conducting random surface," *IEEE Transactions on Antennas and Propagation*, vol. 26, no. 3, pp. 482–488, 1978.
- [AGV98] P. Aikio, R. Gruber, and P. Vainikainen, "Wideband radio channel measurements for train tunnels," in *IEEE Int. Vehicular Technology Conference (VTC'98)*, Ottawa, Canada, May 1998, pp. 460–464.
- [Arn97] A. Arnold, *Entwicklung eines vektoriiellen mm-Wellen-Netzwerkanalysators mit hoher Meßdynamik und Messungen an überdimensionierten Wellenleiterkomponenten*, diploma thesis, IHE, Universität Karlsruhe (TH), Germany, 1997, and *Wissenschaftliche Berichte*, FZKA 6108, Forschungszentrum Karlsruhe, Nov. 1998, (in German).
- [AS72] M. Abramowitz and I.A. Stegun, *Handbook of Mathematical Functions*, Dover Publ., New York, 1972.
- [Bal89] C.A. Balanis, *Advanced Engineering Electromagnetics*, John Wiley & Sons, New York, 1989.
- [Bal97] C.A. Balanis, *Antenna Theory, Analysis and Design*, John Wiley & Sons, New York, 1997.
- [Bar68] D.E. Barrick, "Rough surface scattering based on the specular point theory," *IEEE Transactions on Antennas and Propagation*, vol. 16, no. 4, pp. 449–454, 1968.
- [BBD75] J. Bach Andersen, S. Berntsen, and P. Dalsgaard, "Propagation in rectangular waveguides with arbitrary internal and external media," *IEEE Transactions on Microwave Theory and Techniques*, vol. 23, no. 7, pp. 555–560, 1975.
- [Bec96] T.C. Becker, *Verfahren und Kriterien zur Planung von Gleichwellennetzen für den digitalen Hörrundfunk DAB (Digital Audio Broadcasting)*, Ph.D. thesis, Universität Karlsruhe (TH), Germany, 1996, (in German).
- [Bel63] P.A. Bello, "Characterization of Randomly Time-Variant Linear Channels," *IEEE Transactions on Communications Systems*, vol. 11, pp. 360–393, Dec. 1963.

- [BHK93] M. Bossert, B. Hätty, and P. Klund, "Propagation aspects on railway environment in the GSM frequency range," in *ITG-Fachbericht Mobile Kommunikation 124*, Neu Ulm, Germany, Sep. 1993, pp. 319–330.
- [BK97] M.V. Berry and S. Klein, "Die Farben von Kaustiken—Katasrophen in Regentropfen und Strukturglas," *Physik Blätter*, vol. 53, no. 11, pp. 1095–1098, 1997, (in German).
- [BL74] E. Beyer and K. Lange, *Verkehrsbauten: Brücken, Hochstraßen, Tunnel*, Beton-Verlag, Düsseldorf, 1974, (in German).
- [BS63] P. Beckmann and A. Spizzichino, *The Scattering of Electromagnetic Waves from Rough Surfaces*, Pergamon Press, Oxford, 1963.
- [BS⁺99] I.N. Bronstein, K.A. Semendjajew, G. Musiol, and H. Mühlig, *Taschenbuch der Mathematik*, Verlag Harri Deutsch, Thun, 4th edition, 1999, (in German).
- [BU88] A. Büyükkaksoy and G. Uzgören, "Diffraction of high-frequency waves by a cylindrically curved surface with different face impedances," *IEEE Transactions on Antennas and Propagation*, vol. 36, no. 5, pp. 690–695, 1988.
- [CF94] L.M. Correia and P.O. Francês, "Estimation of materials characteristics from power measurements at 60 GHz," in *IEEE Int. Symposium on Personal, Indoor and Mobile Radio Communications (PIMRC'94)*, The Hague, The Netherlands, Sep. 1994, pp. 510–513.
- [CG99] J.M. Canabal Muñoz and C. Galdón Durá, *Implementation and verification of a quick method for the determination of the power-flow as well as the coupling of electromagnetic waves in tunnels*, diploma thesis, IHE, Universität Karlsruhe (TH), Germany, 1999.
- [CI⁺78] J. Chiba, T. Inaba, Y. Kuwamoto, O. Banno, and R. Sato, "Radio communication in tunnels," *IEEE Transactions on Microwave Theory and Techniques*, vol. 26, no. 6, pp. 439–443, 1978.
- [Cic94] D.J. Cichon, *Strahlenoptische Modellierung der Wellenausbreitung in urbanen Mikro- und Pikofunkzellen*, Ph.D. thesis, Universität Karlsruhe (TH), Germany, 1994, (in German).
- [CJ95] S.-H. Chen and S.-K. Jeng, "An SBR/image approach for indoor radio propagation in a corridor," *IEICE Trans. Electron.*, vol. E78-C, no. 8, pp. 1058–1062, 1995.
- [CJ96a] S.-H. Chen and S.-K. Jeng, "SBR image approach for radio wave propagation in tunnels with and without traffic," *IEEE Transactions on Vehicular Technology*, vol. 45, no. 3, pp. 570–578, 1996.
- [CJ96b] S.-H. Chen and S.-K. Jeng, "SBR/image approach for indoor radio propagation in large empty buildings," *IEICE Trans. Commun.*, vol. E79-B, no. 9, pp. 1184–1191, 1996.

- [CJ97] S.-H. Chen and S.-K. Jeng, "An SBR/image approach for radio wave propagation in indoor environments with metallic furniture," *IEEE Transactions on Antennas and Propagation*, vol. 45, no. 1, pp. 98–106, 1997.
- [CKW93] D.J. Cichon, T. Kürner, and W. Wiesbeck, "Modellierung der Wellenausbreitung in urbanem Gelände," *Frequenz*, vol. 47, no. 1/2, pp. 2–11, 1993, (in German).
- [Col91] R.E. Collin, *Field Theory of Guided Waves*, IEEE Press, Piscataway, 2nd edition, 1991.
- [COST207] COST Action 207, *Digital Land Mobile Radio Communications—Final Report*, European Cooperation in the Field of Scientific and Technical Research, European Commission, EUR 12160 EN, Luxembourg, 1989.
- [COST231] COST Action 231, *Digital Mobile Radio Towards Future Generation Systems—Final Report*, European Cooperation in the Field of Scientific and Technical Research, European Commission, EUR 18957, Luxembourg, 1999.
- [COST235] COST Action 235, *Radiowave propagation effects on next-generation fixed-services terrestrial telecommunications systems—Final Report*, European Cooperation in the Field of Scientific and Technical Research, European Commission, EUR 16992 EN, Luxembourg, 1996.
- [CP⁺98] M.F. Catedra, J. Perez, F. Saez de Adana, and O. Gutierrez, "Efficient ray-tracing techniques for 3D analyses of propagation in mobile communications: Application to picocell and microcell scenarios," *IEEE Antennas and Propagation Magazine*, vol. 40, no. 2, pp. 15–28, 1998.
- [CZL95] D.J. Cichon, T. Zwick, and J. Lähteenmäki, "Ray optical indoor modeling in multi-floored buildings: simulations and measurements," in *IEEE Antennas and Propagation Society Int. Symposium (AP-S'95)*, Newport Beach, California, USA, June 1995, pp. 522–525.
- [CZW96] D.J. Cichon, T. Zwick, and W. Wiesbeck, "Ray optical modeling of wireless communication in high-speed railway tunnels," in *IEEE Int. Vehicular Technology Conference (VTC'96)*, Atlanta, GA, USA, Apr./May 1996, pp. 546–550.
- [DD⁺70] R. De Keyser, P. Delogne, J. Janssens, and R. Liegeois, "Radiocommunication and control in mines and tunnels," *IEE Electronics Letters*, vol. 6, no. 24, pp. 767–768, 1970.
- [DD⁺99] D. Didascalou, M. Döttling, T. Zwick, and W. Wiesbeck, "A novel ray optical approach to model wave propagation in curved tunnels," in *IEEE Int. Vehicular Technology Conference (VTC'99-Fall)*, Amsterdam, The Netherlands, Sep. 1999, pp. 2313–2317.
- [Del76] P. Delogne, "Basic mechanisms of tunnel propagation," *Radio Science*, vol. 11, no. 4, pp. 295–303, 1976.

- [Del82] P. Delogne, *Leaky Feeders and Subsurface Radio Communication*, Peter Peregrinus Ltd., New York, 1982.
- [Del87] P. Delogne, "Small holes and leaky feeders," *Radio Science*, vol. 22, no. 7, pp. 1179–1189, 1987.
- [Del91] P. Delogne, "EM propagation in tunnels," *IEEE Transactions on Antennas and Propagation*, vol. 39, no. 3, pp. 401–405, 1991.
- [Der78] L. Deryck, "Natural propagation of electromagnetic waves in tunnels," *IEEE Transactions on Vehicular Technology*, vol. 27, no. 3, pp. 145–150, 1978.
- [Des72] G.A. Deschamps, "Ray techniques in electromagnetics," *Proceedings of the IEEE*, vol. 60, no. 9, pp. 1022–1035, 1972.
- [DH73] R.O. Duda and P.E. Hart, *Pattern Classification and Scene Analysis*, John Wiley & Sons, New York, 1973.
- [DIN99] Standard DIN EN 295, *Steinzeugrohre und Formstücke sowie Rohrverbindungen für Abwasserleitungen und -kanäle*, Deutsches Institut für Normung e.V., Beuth Verlag GmbH, Berlin, 1999, (in German).
- [DKW99] D. Didascalou, F. Küchen, and W. Wiesbeck, "A novel normalization technique for ray-optical wave propagation modelling in arbitrarily shaped tunnels," *Frequenz*, vol. 53, no. 9/10, pp. 182–188, 1999, (in German).
- [DU94] R.D. De Roo and F.T. Ulaby, "Bistatic specular scattering from rough dielectric surfaces," *IEEE Transactions on Antennas and Propagation*, vol. 42, no. 2, pp. 220–231, 1994.
- [DZW97] M. Döttling, T. Zwick, and W. Wiesbeck, "Ray tracing and imaging techniques in urban pico and micro cell propagation modeling," in *IEE Int. Conference on Antennas and Propagation (ICAP'97)*, Edinburgh, UK, Apr. 1997, pp. 2.311–2.315.
- [ELS75] A.G. Emslie, R.L. Lagace, and P.F. Strong, "Theory of the propagation of UHF radio waves in coal mine tunnels," *IEEE Transactions on Antennas and Propagation*, vol. 23, no. 2, pp. 192–205, 1975.
- [Feh97] L.E. Feher, *Simulationsrechnungen zur verfahrenstechnischen Anwendung von Millimeterwellen für die industrielle Materialprozeßtechnik*, Ph.D. thesis, Universität Karlsruhe (TH), Germany, 1997, and *Wissenschaftliche Berichte*, FZKA 5885, Forschungszentrum Karlsruhe, Aug. 1997, (in German).
- [FG⁺93] G. Fröhlingdorf, M. Göller, K.-D. Masur, and U. Weber, "Messergebnisse und Parameter zur Modellierung von Bahn-Mobilfunkkanälen im 900-MHz-Band," *Nachrichtentech., Elektron.*, vol. 6, no. 43, pp. 290–295, 1993, (in German).
- [Fin98] R. Finkle, *A Polarimetric Millimetre Wave Sensor System for Road Surface Classification*, Ph.D. thesis, Cranfield University, UK, July 1998.

- [FL96] B.H. Fleury and P.E. Leuthold, "Radiowave propagation in mobile communications: An overview of European research," *IEEE Communications Magazine*, vol. 34, no. 2, pp. 70–81, 1996.
- [Fle90] B.H. Fleury, *Charakterisierung von Mobil- und Richtfunkkanälen mit schwach stationären Fluktuationen und unkorrelierter Streuung (WS-SUS)*, Ph.D. thesis, ETH Zürich, Switzerland, 1990, (in German).
- [Foc65] V.A. Fock, *Electromagnetic Diffraction and Propagation Problems*, Pergamon Press, Oxford, 1965.
- [Fun94] A. Fung, *Microwave Scattering and Emission Models and Their Applications*, Artech House, London, 1994.
- [FvD⁺94] J.D. Foley, A. van Dam, S.K. Feiner, J.F. Hughes, and R.L. Phillips, *Grundlagen der Computergraphik - Einführung, Konzepte, Methoden*, Addison-Wesley, Bonn, 1994.
- [GDW71] R. Gabillard, P. Degauque, and J.R. Wait, "Subsurface electromagnetic telecommunication—a review," *IEEE Transactions on Communication Technology*, vol. 19, no. 6, pp. 1217–1228, 1971.
- [Gen96] N. Geng, *Modellierung der Ausbreitung elektromagnetischer Wellen in Funksystemen durch Lösung der parabolischen Approximation der Helmholtz-Gleichung*, Ph.D. thesis, Universität Karlsruhe (TH), Germany, 1996, (in German).
- [Gla95] A.S. Glassner, Ed., *Graphics Gems*, vol. I–V of *The Graphics Gems Series*, AP Professional, Boston, 1990–95.
- [Gla89] A.S. Glassner, Ed., *An Introduction to Ray Tracing*, Academic Press, San Diego, 1989.
- [GM92a] M. Göller and K.-D. Masur, "Ergebnisse von Funkkanalmessungen im 900-MHz-Bereich auf Neubaustrecken der Deutschen Bundesbahn, Teil 1+2," *Nachrichtentech., Elektron.*, vol. 42, no. 4, pp. 143–146, and vol. 42, no. 5, pp. 206–210, 1992, (in German).
- [Gsc95] B.E. Gschwendtner, *Adaptive Wellenausbreitungsmodelle für die Funknetzplanung*, Ph.D. thesis, Universität Stuttgart, Germany, 1995, (in German).
- [GW⁺95] B.E. Gschwendtner, G. Wölfle, B. Burk, and F.M. Landstorfer, "Ray tracing vs. ray launching in 3D microcell modelling," in *European Personal and Mobile Communications Conference (EPMCC'95)*, Bologna, Italy, Nov. 1995, pp. 74–79.
- [GW96] N. Geng and W. Wiesbeck, "Feldtheoretische Modellierung der Wellenausbreitung in Funksystemen," *Frequenz*, vol. 50, pp. 274–284, 1996, (in German).
- [GW98] N. Geng and W. Wiesbeck, *Planungsmethoden für die Mobilkommunikation, Funknetzplanung unter realen physikalischen Ausbreitungsbedingungen*, Springer, Berlin, 1998, (in German).

- [Hag66] T. Hagfors, "Relationship of geometric optics and autocorrelation approaches to the analysis of lunar and planetary radar," *Journal of Geophysical Research*, vol. 71, no. 2, pp. 379–383, 1966.
- [Hal79] M.P.M. Hall, *Effects of the Troposphere on Radio Communications*, Peter Peregrinus Ltd., New York, 1979.
- [Har68] R.F. Harrington, *Field Computation by Moment Methods*, Macmillan, New York, 1968.
- [HB⁺92] W. Honcharenko, H.L. Bertoni, J.L. Dailing, J. Qian, and H.D. Yee, "Mechanisms governing UHF propagation on single floors in modern office buildings," *IEEE Transactions on Vehicular Technology*, vol. 41, no. 4, pp. 496–504, 1992.
- [HCC98] S.-C. Hung, C.-C. Chiu, and C.-H. Chen, "Wireless communication characteristics for tunnels with and without traffic," in *IEEE Int. Conf. on Universal Personal Communications (ICUPC'98)*, Florence, Italy, Oct. 1998, pp. 117–122.
- [ITU676] ITU-R Rep. 676-1, *Propagation in Non-Ionized Media: Attenuation by Atmospheric Gases in the Frequency Range 1–350 GHz*, International Telecommunications Union (ITU), Geneva, 1992.
- [ITU1057] ITU-R Rec. PN.1057, *Probability distributions relevant to radiowave propagation modelling*, International Telecommunications Union (ITU), Geneva, 1994.
- [ITU1075] ITU-R Rec. M.1075, *Leaky feeder systems in the land mobile services*, International Telecommunications Union (ITU), Geneva, 1994.
- [ITU1238] ITU-R Rec. P.1238, *Propagation data and prediction models for the planning of indoor radiocommunications systems and radio local area networks in the frequency range 900 MHz to 100 GHz*, International Telecommunications Union (ITU), Geneva, 1997.
- [Jäh97] B. Jähne, *Digitale Bildverarbeitung*, Springer, Berlin, 1997, (in German).
- [Jam86] G.L. James, *Geometrical Theory of Diffraction for Electromagnetic Waves*, Peter Peregrinus Ltd., London, 3rd edition, 1986.
- [JM84] B. Jacard and O. Maldonado, "Microwave modeling of rectangular tunnels," *IEEE Transactions on Microwave Theory and Techniques*, vol. 32, no. 6, pp. 576–581, 1984.
- [Kat97] R. Kattenbach, *Charakterisierung zeitvarianter Indoor-Funkkanäle anhand ihrer System- und Korrelationsfunktionen*, Ph.D. thesis, Universität Kassel, Aachen, Germany, 1997, (in German).
- [KB94] T. Klemenschts and E. Bonek, "Radio coverage of road tunnels at 900 and 1800 MHz by discrete antennas," in *IEEE Int. Symposium on Personal, Indoor and Mobile Radio Communications (PIMRC'94)*, The Hague, The Netherlands, Sep. 1994, pp. 411–415.

- [KCW93] T. Kürner, D.J. Cichon, and W. Wiesbeck, "Concepts and results for 3D digital terrain based wave propagation models—an overview," *IEEE Journal on Selected Areas in Communications*, vol. 11, no. 7, pp. 1002–1012, 1993.
- [KE95] R. Kattenbach and T. Englert, "Auswertung statistischer Eigenschaften von Impulsantworten zeitvarianter Indoor-Funkkanäle," *Kleinheubacher Berichte*, vol. 39, pp. 321–332, 1995, (in German).
- [Kel62] J.B. Keller, "Geometrical theory of diffraction," *Journal Opt. Soc. Amer.*, vol. 52, no. 2, pp. 116–130, 1962.
- [Kil90] P.-S. Kildal, "Artificially soft and hard surfaces in electromagnetics," *IEEE Transactions on Antennas and Propagation*, vol. 38, no. 10, pp. 1537–1544, 1990.
- [Kin90] F. Kind-Barkauskas, *Gestaltung von Ingenieurbauwerken an Straßen: Brücken, Tunnel, Stützwände*, Beton-Verlag, Düsseldorf, 1990, (in German).
- [KK98] V.K. Kiseliiov and T.M. Kushta, "Ray representation of the electromagnetic field in a circular hollow dielectric waveguide used as a facility for scattering measurements," *IEEE Transactions on Antennas and Propagation*, vol. 46, no. 7, pp. 1116–1117, 1998.
- [Kle93] T. Klemenschits, *Mobile Communications in Tunnels*, Ph.D. thesis, Universität Wien, Austria, 1993.
- [Kli51] M. Kline, "An asymptotic solution of Maxwell's equation," in *The Theory of Electromagnetic Waves*. Interscience, New York, 1951.
- [Kli91] R. Klingler, "Radio coverage for road and rail tunnels in the frequency range 75 to 1000 MHz," in *IEEE Int. Vehicular Technology Conference (VTC'91)*, St. Louis, MO, May 1991, pp. 433–438.
- [KP74] R.G. Kouyoumjian and P.H. Pathak, "A uniform geometrical theory of diffraction for an edge in a perfectly conducting surface," *Proceedings of the IEEE*, vol. 62, no. 11, pp. 1448–1461, 1974.
- [KSB93] T. Klemenschits, A. Scholtz, and E. Bonek, "Microwave measurements in scaled road tunnels modeling 900 MHz propagation," in *IEEE Int. Vehicular Technology Conference (VTC'93)*, Secaucus, NJ, May 1993, pp. 70–72.
- [Küc98] F. Küchen, *Auf Wellenausbreitungsmodellen basierende Planung terrestrischer COFDM-Gleichwellennetze für den mobile Empfang*, Ph.D. thesis, Universität Karlsruhe (TH), Germany, 1998, (in German).
- [Kür93] T. Kürner, *Charakterisierung digitaler Funksysteme mit einem breitbandigen Wellenausbreitungsmodell*, Ph.D. thesis, Universität Karlsruhe (TH), Germany, 1993, (in German).
- [Lan57] E. Langsdorf, *Ultrakurzwellen-Zugfunk in irregulärem Gelände*, Ph.D. thesis, Universität Karlsruhe (TH), Germany, 1957, (in German).

- [Laq94] C. Laqué, *Simulation der Funkübertragung im Hochgeschwindigkeitstunnel*, diploma thesis, IHE, Universität Karlsruhe (TH), Germany, 1994, (in German).
- [LB⁺94] M. Lienard, S. Baranowski, P. Degauque, and J. Vandamme, "Theoretical and experimental study of radio coverage in tunnels using radiating cables," *Ann. Telecommun.*, vol. 49, no. 3/4, pp. 143–153, 1994.
- [LC⁺88] M. Lecours, J.-Y. Chouinard, G.Y. Delisle, and J. Roy, "Statistical modeling of the received signal envelope in a mobile radio channel," *IEEE Transactions on Vehicular Technology*, vol. 37, no. 4, pp. 204–212, 1988.
- [LCL89] H. Ling, R.-C. Chou, and S.-W. Lee, "Shooting and bouncing rays: Calculating the RCS of an arbitrarily shaped cavity," *IEEE Transactions on Antennas and Propagation*, vol. 37, no. 2, pp. 194–205, 1989.
- [LD98] M. Lienard and P. Degauque, "Propagation in wide tunnels at 2 GHz: A statistical analysis," *IEEE Transactions on Vehicular Technology*, vol. 47, no. 4, pp. 1322–1328, 1998.
- [Leb91] M. Leberherz, *Wellenausbreitungsmodelle zur Versorgungsplanung im VHF/UHF Bereich unter Berücksichtigung der Mehrwegeausbreitung*, Ph.D. thesis, Universität Karlsruhe (TH), Germany, 1991, (in German).
- [Lee82] W.C.Y. Lee, *Mobile Communications Engineering*, McGraw-Hill, New York, 1982.
- [Lee89] W.C.Y. Lee, *Mobile Cellular Telecommunications Systems*, McGraw-Hill, New York, 1989.
- [Leh90] G. Lehner, *Elektromagnetische Feldtheorie für Ingenieure und Physiker*, Springer, Berlin, 1990, (in German).
- [LFR96] O. Landron, M.J. Feuerstein, and T.S. Rappaport, "A comparison of theoretical and empirical reflection coefficients for typical exterior wall surfaces in a mobile radio environment," *IEEE Transactions on Antennas and Propagation*, vol. 44, no. 3, pp. 341–351, 1996.
- [LL98] J.S. Lamminmäki and J.J.A. Lempiäinen, "Radio propagation characteristics in curved tunnels," *IEE Proceedings—Microwaves, Antennas and Propagation*, vol. 145, no. 4, pp. 327–331, 1998.
- [LM88] E.A. Lee and D.G. Messerschmitt, *Digital Communication*, Kluwer, London, 1988.
- [LM94] M.C. Lawton and J.P. McGeehan, "The application of a deterministic ray launching algorithm for the prediction of radio channel characteristics in small-cell environments," *IEEE Transactions on Vehicular Technology*, vol. 43, no. 4, pp. 955–968, 1994.
- [Lor79] R.W. Lorenz, "Theoretical distribution functions of multipath fading processes in the mobile radio and determination of their parameters by measurements," Tech. Rep. FI 455 TBr 66, Deutsche Bundespost, Forschungsinstitut beim FTZ, May 1979, (in German).

- [LS76] K.D. Laakmann and W.H. Steier, "Waveguides: characteristic modes of hollow rectangular dielectric waveguides," *Applied Optics*, vol. 15, no. 5, pp. 1334–1340, 1976.
- [LS99] E.S. Li and K. Sarabandi, "Low grazing incidence millimeter-wave scattering models and measurements for various road surfaces," *IEEE Transactions on Antennas and Propagation*, vol. 47, no. 5, pp. 851–861, 1999.
- [Lun64] R.K. Luneburg, *Mathematical Theory of Optics*, University of California Press, Berkeley, California, 1964.
- [LWK92] M. Lebherz, W. Wiesbeck, and W. Krank, "A versatile wave propagation model for the VHF/UHF range considering three dimensional terrain," *IEEE Transactions on Antennas and Propagation*, vol. 40, no. 10, pp. 1121–1131, 1992.
- [Mah74] S.F. Mahmoud, "Characteristics of electromagnetic guided waves for communication in coal mine tunnels," *IEEE Transactions on Communications*, vol. 22, no. 10, pp. 1547–1554, 1974.
- [Mah91] S.F. Mahmoud, *Electromagnetic Waveguides, Theory and Practice*, Peter Peregrinus Ltd., London, 1991.
- [Mar70] J.R. Martin, "Radiocommunication in mines and tunnels," *IEE Electronics Letters*, vol. 6, no. 18, pp. 563–564, 1970.
- [Mar86] L. Marsolek, *BASIC im Bau- und Vermessungswesen*, B.G. Teubner, Stuttgart, 1986, (in German).
- [Mar89] L. Mariel, "Using radiating cables for RF propagation," *Communications International*, vol. 16, no. 4, pp. 70–71, 1989.
- [Mar92] P. Mariage, *Etude théorique et expérimentale de la propagation des ondes hyperfréquences en milieu confiné ou urbain*, Ph.D. thesis, Université de Lille, France, 1992, (in French).
- [Mar93] K. Martinek, "Entwicklung von Tunnelquerschnitten für Neubaustrecken und Ausbaustrecken," *Ingenieurbauwerke der Neubaustrecken der Deutschen Bundesbahn, Archiv für Eisenbahntechnik*, vol. 44, pp. 115–130, 1993, (in German).
- [MC94] K. Matsui and J. Chiba, "The propagation characteristic of the crank-tunnel with reflector," *IEEE Transactions on Vehicular Technology*, vol. 43, no. 4, pp. 1145–1147, 1994.
- [MG92] Meinke and Gundlach, *Taschenbuch der Hochfrequenztechnik*, vol. I–III, Springer, Berlin, 5th edition, 1992, (in German).
- [MH91] J.W. McKown and R.L. Hamilton, "Ray tracing as a design tool for radio networks," *IEEE Network Magazine*, vol. 5, no. 6, pp. 27–30, 1991.
- [Mic98] G. Michel, *Feldprofilanalyse und -synthese im Millimeterwellenbereich*, Ph.D. thesis, Universität Karlsruhe (TH), Germany, 1998, and *Wissenschaftliche Berichte*, FZKA 6216, Forschungszentrum Karlsruhe, Dec. 1998, (in German).

- [Mit75] R. Mittra, Ed., *Numerical and Asymptotic Techniques in Electromagnetics*, Springer Verlag, New York, 1975.
- [MLD94] P. Mariage, M. Lienard, and P. Degauque, "Theoretical and experimental approach of the propagation of high frequency waves in road tunnels," *IEEE Transactions on Antennas and Propagation*, vol. 42, no. 1, pp. 75–81, 1994.
- [Mor99] S.P. Morgan, "Prediction of indoor wireless coverage by leaky coaxial cable using ray tracing," *IEEE Transactions on Vehicular Technology*, vol. 48, no. 6, pp. 2005–2014, 1999.
- [MP78] J.N. Murphy and H.E. Parkinson, "Underground mine communications," *Proceedings of the IEEE*, vol. 66, no. 1, pp. 26–50, 1978.
- [MPM90] D.A. McNamara, C.W.L. Pistorius, and J.A.G. Malherbe, *Introduction to the Uniform Geometrical Theory of Diffraction*, Artech House, London, 1990.
- [MT99] G. Michel and M. Thumm, "Spectral domain techniques for field pattern analysis and synthesis," *Surveys on Mathematics for Industry, Special Issue on Scientific Computing in Electrical Engineering*, vol. 8, pp. 259–270, 1999.
- [Mü191] P.H. Müller, Ed., *Lexikon der Stochastik*, Akademie Verlag, Berlin, 5th edition, 1991, (in German).
- [Mü194a] A. Müller, "Monte-Carlo modelling and simulation of multipath mobile radio channels," in *Proc. 8. Aachener Kolloquium Signaltheorie*, Aachen, Germany, 1994, pp. 341–346.
- [Mü194b] A. Müller, "Monte-Carlo multipath simulation of ray tracing channel models," in *IEEE Global Telecommunications Conference (GLOBE-COM'94)*, San Francisco, Nov./Dec. 1994, vol. 3, pp. 1446–1450.
- [MW74a] S.F. Mahmoud and J.R. Wait, "Geometrical optical approach for electromagnetic wave propagation in rectangular mine tunnels," *Radio Science*, vol. 9, no. 12, pp. 1147–1158, 1974.
- [MW74b] S.F. Mahmoud and J.R. Wait, "Guided electromagnetic waves in a curved rectangular mine tunnel," *Radio Science*, vol. 9, no. 5, pp. 567–572, 1974.
- [Nie94] K. Niederer, "Funkversorgung in Tunnels," *Signal+Draht*, vol. 86, no. 7/8, pp. 232–237, 1994, (in German).
- [NM65] J.A. Nelder and R. Mead, "A simplex method for function minimization," *The Computer Journal*, vol. 7, pp. 308–313, 1964/65.
- [OS⁺90] Y. Ohtaki, M. Sengoku, K. Sakurai, Y. Yamaguchi, and T. Abe, "Propagation characteristics in open-groove waveguides surrounded by rough sidewalls," *IEEE Transactions on Electromagnetic Compatibility*, vol. 32, no. 3, pp. 177–184, 1990.

- [Pap84] A. Papoulis, *Probability, Random Variables and Stochastic Processes*, McGraw-Hill, New York, 2nd edition, 1984.
- [PB89] P.H. Pathak and R.J. Burkholder, "Modal, ray, and beam techniques for analyzing the EM scattering by open-ended wave guide cavities," *IEEE Transactions on Antennas and Propagation*, vol. 37, no. 5, pp. 635–647, 1989.
- [PBM80] P.H. Pathak, W.D. Burnside, and R.J. Marhefka, "A uniform GTD analysis of the diffraction of electromagnetic waves by a smooth convex surface," *IEEE Transactions on Antennas and Propagation*, vol. 28, no. 5, pp. 631–641, 1980.
- [Pol96] M.W. Pollack, "Communications-based signaling: Advanced capability for mainline railroads," *IEEE Aerospace and Electronics System Magazine*, vol. 11, no. 11, pp. 13–18, 1996.
- [PP94] N. Prediger and A. Plattner, "Propagation measurements at 60 GHz in railroad tunnels," in *IEEE Int. Microwave Symposium (MTT-S'94)*, San Diego, CA, May 1994, pp. 1085–1087.
- [Pro89] J.G. Proakis, *Digital Communications*, McGraw-Hill, New York, 2nd edition, 1989.
- [Pro93] K. Probst, "Wellenausbreitung in Strassentunnels von 90 MHz–1.9 GHz," Tech. Rep. VD21.1224V, Generaldirektion PTT, Switzerland, 1993, (in German).
- [PT⁺92] W.H. Press, S.A. Teukolsky, W.T. Vetterling, and B.P. Flannery, *Numerical Recipes in C*, Cambridge University Press, 2nd edition, 1992.
- [RB⁺70] G.T. Ruck, D.E. Barrick, W.D. Stuart, and C.K. Krichbaum, *Radar Cross Section Handbook*, Plenum Press, New York, London, 1970.
- [Rem93] B. Rembold, "Simulation of radio transmission in a tunnel," *Frequenz*, vol. 47, no. 11/12, pp. 270–275, 1993, (in German).
- [Riz97] K. Rizk, *Propagation in microcellular and small cell urban environment*, Ph.D. thesis, Ecole Polytechnique Fédérale de Lausanne, Switzerland, 1997.
- [Rut99] B. Ruthmann, *Meßtechnische Verifizierung des Simulationsprogramms "IHE-TUNNEL" in Modelltunneln bei 120GHz*, study thesis, IHE, Universität Karlsruhe (TH), Germany, 1999, (in German).
- [Sch95] T. Schöberl, "Combined Monte Carlo simulation and ray tracing method of indoor radio propagation channel," in *IEEE Int. Microwave Symposium (MTT-S'95)*, Apr. 1995, vol. 3, pp. 1379–1382.
- [Sch98] R. Schneider, *Modellierung der Wellenausbreitung für ein bildgebendes Kfz-Radar*, Ph.D. thesis, Universität Karlsruhe (TH), Germany, 1998, (in German).

- [Sch99] O. Schindel, *Entwicklung einer automatisierten Meßwerterfassung für einen vektoriellen Millimeterwellen-Netzwerkanalysator mit hoher Dynamik*, diploma thesis, IHE, Universität Karlsruhe (TH), Germany, 1999, and *Wissenschaftliche Berichte*, FZKA 6348, Forschungszentrum Karlsruhe, Sep. 1999, (in German).
- [SDK96] A. Schmitt, O. Deussen, and M. Kreeb, *Einführung in graphisch-geometrische Algorithmen*, B.G. Teubner, Stuttgart, 1996, (in German).
- [SDW00] R. Schneider, D. Didascalou, and W. Wiesbeck, "Impact of road surfaces on millimeter wave propagation," *IEEE Transactions on Vehicular Technology*, 2000, accepted for publication.
- [Sge91] L. Saxton (guest editor), "Special Issue on Intelligent Vehicle Highway Systems," *IEEE Transactions on Vehicular Technology*, vol. 40, no. 1, 1991.
- [SL90] W. Schäfer and E. Lutz, "Propagation characteristics of short-range radio links at 60GHz for mobile intervehicle communication," in *IEEE Intern. Telecommunications Symposium (ITS'90)*, Rio de Janeiro, Brasil, Sep. 1990, pp. 212–216.
- [SM⁺96] K. Sato, T. Manabe, J. Polivka, T. Ihara, Y. Kasashima, and K. Yamaki, "Measurement of the complex refractive index of concrete at 57.5 GHz," *IEEE Transactions on Antennas and Propagation*, vol. 44, no. 1, pp. 35–39, 1996.
- [SM97] H. Suzuki and A.S. Mohan, "Ray tube tracing method for predicting indoor channel characteristics map," *IEE Electronics Letters*, vol. 33, no. 17, pp. 1495–1496, 1997.
- [Sob91] I.M. Sobol, *Die Monte-Carlo Methode*, Deutscher Verlag der Wissenschaften, Berlin, 1991, (in German).
- [SR94] S.Y. Seidl and T.S. Rappaport, "Site-specific propagation prediction for wireless in-building personal communication system design," *IEEE Transactions on Vehicular Technology*, vol. 43, no. 4, pp. 879–891, 1994.
- [Ste92] R. Steele, Ed., *Mobile Radio Communications*, Pentech Press, London, 1992.
- [Str95] Arbeitsgruppe Straßenentwurf, "Richtlinien für die Anlage von Straßen RAS: Linienführung RAS-L," Tech. Rep., Forschungsgesellschaft für Straßen- und Verkehrswesen, Köln, 1995, (in German).
- [Str96] Arbeitsgruppe Straßenentwurf, "Dokumentation für Straßentunneln in Deutschland," Tech. Rep., Forschungsgesellschaft für Straßen- und Verkehrswesen, Köln, 1996, (in German).
- [SW98] T. Schäfer and F. Weinmann, *Funkwellenausbreitung im Tunnel*, diploma thesis, IHE, Universität Karlsruhe (TH), Germany, 1998, (in German).

- [Taf95] A. Taflove, Ed., *Computational Electrodynamics, The Finite-Difference Time-Domain Method*, Artech House, Boston, 1995.
- [Tai93] C.-T. Tai, *Dyadic Green Functions in Electromagnetic Theory*, IEEE Press, Piscataway, 2nd edition, 1993.
- [TCH97] J.H. Tarng, W.R. Chang, and B.J. Hsu, "Three-dimensional modelling of 900MHz and 2.44GHz radio propagation in corridors," *IEEE Transactions on Vehicular Technology*, vol. 46, no. 2, pp. 519–527, 1997.
- [TT95] S.Y. Tan and H.S. Tan, "Modelling and measurement of channel impulse response for an indoor wireless communication system," *IEE Proceedings—Microwaves, Antennas and Propagation*, vol. 142, no. 5, pp. 405–410, 1995.
- [TV⁺99] R.P. Torres, L. Valle, M. Domingo, S. Loredó, and M.C. Diez, "CIN-DOOR: An engineering tool for planning and design of wireless systems in enclosed spaces," *IEEE Antennas and Propagation Magazine*, vol. 41, no. 4, pp. 11–22, 1999.
- [UE98] C. Ucke and C. Engelhardt, "Kaustik in der Kaffeetasse," *Physik in unserer Zeit*, vol. 29, no. 3, pp. 120–122, 1998, (in German).
- [UMF83] F.T. Ulaby, R.K. Moore, and A.K. Fung, *Microwave Remote Sensing: Active and Passive*, vol. I–III, Addison-Wesley, London, 1981–83.
- [vD94] G.A.J. van Dooren, *A Deterministic Approach to the Modelling of Electromagnetic Wave Propagation in Urban Environments*, Ph.D. thesis, Technische Universiteit Eindhoven, The Netherlands, 1994.
- [Vet92] H. Vetsch, "Funkausbreitung in Eisenbahntunnels 150–900 MHz," *Signal+Drabt*, vol. 84, no. 10, pp. 297–303, 1992, (in German).
- [Wai67] J.R. Wait, "Electromagnetic whispering gallery modes in a dielectric rod," *Radio Science*, vol. 2, no. 9, pp. 1005–1017, 1967.
- [Wai75] J.R. Wait, "Theory of EM wave propagation through tunnels," *Radio Science*, vol. 10, no. 7, pp. 753–759, 1975.
- [Wai80] J.R. Wait, "Propagation in rectangular tunnel with imperfectly conducting walls," *IEE Electronics Letters*, vol. 16, no. 13, pp. 521–522, 1980.
- [Web96] R. Weber, *Ein polygon-orientierter Raytracer unter spezieller Berücksichtigung speichereffizienter Datenstrukturen und Verwendung laufzeit-optimierter Algorithmen*, diploma thesis, IBDS, Universität Karlsruhe (TH), Germany, 1996, (in German).
- [WSC97] R.L. Wagner, J. Song, and W.C. Chew, "Monte Carlo simulation of electromagnetic scattering from two-dimensional random rough surfaces," *IEEE Transactions on Antennas and Propagation*, vol. 45, no. 2, pp. 235–245, 1997.
- [YA⁺85] Y. Yamaguchi, T. Abe, T. Sekiguchi, and J. Chiba, "Attenuation constants of UHF radio waves in arched tunnels," *IEEE Transactions on Microwave Theory and Techniques*, vol. 33, no. 8, pp. 714–718, 1985.

- [YAS86] Y. Yamaguchi, T. Abe, and T. Sekiguchi, "Experimental study of radio propagation characteristics in an underground street and corridors," *IEEE Transactions on Electromagnetic Compatibility*, vol. 28, no. 3, pp. 148–155, 1986.
- [YAS89] Y. Yamaguchi, T. Abe, and T. Sekiguchi, "Radio wave propagation loss in the VHF to microwave region due to vehicles in tunnels," *Transactions on Electromagnetic Compatibility*, vol. 31, no. 1, pp. 87–91, 1989.
- [Yee66] K.S. Yee, "Numerical solution of initial boundary value problems involving Maxwell's equations in isotropic media," *IEEE Transactions on Antennas and Propagation*, vol. 14, no. 3, pp. 302–307, 1966.
- [YKS91] H. Yamamura, T. Kawamura, and S. Sasaki, "Millimeter-wave propagation characteristics and applications in railway radio systems," *Quarterly Report of RTRI*, vol. 32, no. 3, pp. 182–189, 1991.
- [ZH98a] Y.P. Zhang and Y. Hwang, "Characterization of UHF radio propagation channels in tunnel environments for microcellular and personal communications," *IEEE Transactions on Antennas and Propagation*, vol. 47, no. 1, pp. 283–296, 1998.
- [ZH98b] Y.P. Zhang and Y. Hwang, "Measurements and statistical modelling of 900 MHz radio propagation channels for microcellular and personal communications in tunnels," *Wireless Personal Communications*, vol. 7, no. 1, pp. 25–39, 1998.
- [ZH98c] Y.P. Zhang and Y. Hwang, "Theory of the radio-wave propagation in railway tunnels," *IEEE Transactions on Vehicular Technology*, vol. 47, no. 3, pp. 1027–1036, 1998.
- [ZHK98a] Y.P. Zhang, Y. Hwang, and R.G. Kouyoumjian, "Ray-optical prediction of radio-wave propagation characteristics in tunnel environments—part 1: Theory," *IEEE Transactions on Antennas and Propagation*, vol. 46, no. 9, pp. 1328–1336, 1998.
- [ZHK98b] Y.P. Zhang, Y. Hwang, and R.G. Kouyoumjian, "Ray-optical prediction of radio-wave propagation characteristics in tunnel environments—part 2: Analysis and measurements," *IEEE Transactions on Antennas and Propagation*, vol. 46, no. 9, pp. 1337–1345, 1998.
- [ZL⁺99] N.Y. Zhu, F.M. Landstorfer, A.V. Popov, and V.A. Vinogradov, "Numerical study of radio wave propagation in tunnels," in *European Microwave Conference (EUMC'99)*, Munich, Oct. 1999, pp. 283–286.
- [ZSW97] T. Zwick, K. Schmitt, and W. Wiesbeck, "Radio communications through car windows," *ATZ Worldwide*, vol. 99, no. 4, pp. 14–16, 1997.
- [Zwi94] T. Zwick, *Dreidimensionale, strahlenoptische Modellierung der Wellenausbreitung innerhalb komplexer Gebäudestrukturen*, diploma thesis, IHE, Universität Karlsruhe (TH), Germany, 1994, (in German).

Curriculum Vitae

Persönliche Daten:

Name: Dirk Leonidas Didascalou
Geburtsdatum: 29. Juli 1969
Geburtsort: Hamburg
Familienstand: verheiratet, ein Sohn

Schulbildung:

1989 Philipp-Matthäus-Hahn Gymnasium Leinfelden-
Echterdingen: Allgemeine Hochschulreife

Studium und Berufsweg:

1989 - 1991 Studium der Elektrotechnik an der Universität Stuttgart
Vordiplom

1991 - 1992 Aristoteles Universität Thessaloniki
Gasthörer in Elektrotechnik und Neugriechisch

1992 - 1996 Studium der Elektrotechnik an der Universität Karlsruhe (TH)
Europäisches Gemeinschaftsstudium für Elektroingenieure
Vertiefungsrichtung: Nachrichtensysteme

1994 - 1995 Ecole Supérieure d'Ingenieurs en Electrotechnique et
Electronique (ESIEE), Paris

1995 - 1996 University of Southampton
Diplomarbeit: The potential of turbo codes in trellis coding
schemes

seit 1996 Wissenschaftlicher Mitarbeiter am Institut für Höchsthre-
quenztechnik und Elektronik der Universität Karlsruhe (TH)